The Thesis Committee for Lauren Rolston Jacob
Certifies that this is the approved version of the following thesis:

Remote Sensing, Geochemistry, Geochronology, and Cathodoluminescence Imaging of the Egrigoz, Koyunoba, and Alacam Plutons, Northern Menderes Massif, Turkey

APPROVED BY
SUPERVISING COMMITTEE:

Supervisor: ______________________________
Elizabeth Catlos

____
Mark Cloos

____
Daniel Barker

Remote Sensing, Geochemistry, Geochronology, and Cathodoluminescence Imaging of the Egrigoz, Koyunoba, and Alacam Plutons, Northern Menderes Massif, Turkey

by

Lauren Rolston Jacob, B.S.

Thesis

Presented to the Faculty of the Graduate School of

The University of Texas at Austin

in Partial Fulfillment

of the Requirements

for the Degree of

Master of Science in Geological Sciences

The University of Texas at Austin

May, 2011

Acknowledgements

It is my pleasure to thank those who have made this thesis possible. First and foremost, I would like to express my sincere gratitude to my advisor, Dr. Elizabeth Catlos, for accepting me as her graduate student, giving me unbelievable research opportunities in Turkey, and providing constant guidance and advice. This thesis could not have been written without her. This project was funded by the National Science Foundation International Research Experience for Students: Research Opportunities in Extensional Dynamics for US Undergraduate and Graduate Geosciences Students in Western Turkey, Abstract #0937254. The Jackson School of Geosciences at the University of Texas at Austin also provided support for which I am grateful. Also, I would like to thank my committee members, Dr. Mark Cloos and Dr. Daniel Barker, for their advice.

Fieldwork in Turkey would not have been possible without help from Turkish colleagues, Dr. Yasar Kibici, Dr. Tolga Oyman, Mehmet Demirbilek, Okan Yildiz, Ozge Karaman, and Esra Yalcin. I would like to thank Dr. Sorena Sorensen for allowing me to spend the summer in the Cathodoluminescence Laboratory at the Smithsonian Institution National Museum of Natural History in Washington, D.C. Without her advice and guidance, I would have been lost.

Most importantly, I wish to thank my family: my parents, who have always encouraged me to follow my dreams and never give up, my dog Mo for forcing me to take a ten-minute break to go for a daily lunch walk, and my husband Josh for his constant support and understanding. Without Josh, none of this would have been possible. I dedicate this thesis to him.

Abstract

Remote Sensing, Geochemistry, Geochronology, and Cathodoluminescence Imaging of the Egrigoz, Koyunoba, and Alacam Plutons, Northern Menderes Massif, Turkey

Lauren Rolston Jacob, M.S. Geo. Sci.

The University of Texas at Austin, 2011

Supervisor: Elizabeth Catlos

The Egrigoz, Koyunoba, and Alacam plutons are located in the Northern Menderes Massif of western Turkey between the Simav normal fault to the south and the Izmir-Ankara-Erzincan suture to the north. Although much attention has focused on their geochemical and geochronological history, their relationship to each other and other major structures in the region is still debated. Some geologic maps show the Egrigoz and Koyunoba pluton bounded to the west by the low-angle Simav detachment fault. In contrast, other regional maps show no offsets between the plutons and surrounding metamorphic rocks. Yet other studies indicate thrust faults may be present near the Egrigoz pluton, between Menderes metamorphic rocks and a meta-rhyolite unit. To gain a better understanding of the history of the Egrigoz, Koyunoba, and Alacam plutons, ArcGIS digital elevation data from the region, geochronological data, geochemical

analyses, and cathodoluminescence (CL) images were acquired to search for effects of micro- to macro-scales of deformation.

Numerous ~E-W trending extension lineations that parallel the Simav graben and cut the plutons were observed in relief images. These lineations, likely due to large-scale ~N-S extension, continue across plutons inferring that extension continued after the exhumation of these rocks. The Simav graben and its associated high-angle fault are evident in the elevation data, but no other significant detachment-related basins or structures are shown, including the low-angle Simav detachment.

U-Pb zircon ages, ranging from 29.9±3.9 Ma to 14.6±2.6 Ma, suggest the plutons crystallized over a ~15 m.y. time frame. Samples from the plutons are peraluminous S-type granite to granodiorites. The plutons were emplaced in a post-collisional volcanic-arc setting and range from magnesian to ferroan with increasing silica contents. Geochemical analyses show little difference between the three plutons, consistent with the rocks arising from a similar source.

To document microstructures that might help explain these heterogeneities, CL images were obtained. CL images document a complicated tectonic history including magma mixing, multiple episodes of brittle deformation, and fluid alteration. The CL images constitute evidence of a complex multi-stage tectonic history for the region that includes water-mediated brittle deformation.

Table of Contents

List of Tables

List of Figures

Chapter 1: Introduction

1.1 Introduction to the Menderes Massif

The Menderes Massif, located in southwest Turkey, is the largest known metamorphic core complex on Earth, covering >40,000km^2 (Westaway, 2006) (Figure 1-1). A metamorphic core complex forms when lithospheric extension accommodated by detachment faults exposes medium- to high-grade metamorphic rocks. Two end-member models for the initiation of extension in metamorphic core complexes have been proposed (e.g., Corti et al., 2003): (1) active emplacement of hot mantle plume thins and weakens crust while isostatic crustal doming drives active extension and (2) passive tensional regional stress drive extension and magmatism is a consequence of extension (Figure 1-2). Detachment faults accommodating tens to hundreds of kilometers of extension are typically exposed as brittlely deformed sedimentary or low-grade metamorphic rocks of the hanging wall slide over medium-to high-grade ductily deformed rocks of the footwall (e.g. Gessner et al., 2001).

Turkey is made up of multiple terranes of different geologic background separated by suture zones (Moix et al., 2008). These continental fragments include the Rhodope-Pontide fragment, the Cimmerides, the Sakarya Continent, and the Anatolide-Tauride Platform. Prior to extension, the Aegean area experienced multiple episodes of continental collision from the middle Jurassic to the Eocene as these continental fragments sutured (Sengor and Yilmaz, 1981; Moix et al., 2008). Crust in the Menderes Massif thickened due to the closing of the Neotethyan Ocean in the Paleocene-Eocene along the Izmir-Ankara-Erzincan suture zone (e.g., Sengor and Yilmaz, 1981; Gorur et al., 1984) as evidenced by S-vergent thrusting of large-scale nappes (Gessner et al., 2001). From structurally lowest to highest: the Bayindir nappe (metapelitic assemblages with amphibolite and marble lenses; Gessner et al., 2001; Ring et al., 1999; Catlos and Cemen, 2005), the Bozdag nappe (metapelitic assemblages with amphibolite and marble lenses; Gessner et al., 2001), the Cine nappe (ortho and paragneisses; Gessner et al., 2001), and the Selimiye nappe (metasedimentary succession of intercalated marble and calcschist; Catlos and Cemen, 2005). The Cyclades Menderes Thrust placed blueschists and the Lycian nappes of high-pressure-lower temperature metamorphic assemblages structurally above the Selimiye nappe (Gessner et al., 2001).

Post-collisional extension due to slab roll-back and orogenic collapse exhumed several core complexes, including the Rhodpe, Kazadag, Menderes, Attic-Cycladic, and Crete Massifs (Figure 1-1) (e.g., Gautier et al., 2008; Ilbeyli and Kibici, 2009). The Menderes Massif is thought to have formed in three stages of extension based on field data and radiometric ages (Cemen et al., 2006). First, beginning in the late Oligocene and continuing into the Miocene, extension may have initiated by orogenic collapse of overly thickened crust (Dewey, 1988; Pinet and Coletta, 1990; Seyitoglu and Scott, 1996) or back-arc spreading of the Hellenic arc (Le Pichon and Angelier, 1979; Meulenkamp et al., 1988; Seyitoglu and Scott, 1996). Next, the north-dipping Alasehir and south-dipping Buyuk detachments formed in the Central Menderes Massif due to extension caused by the roll-back of the African slab along the Hellenic arc system (Purvis and Robertson, 2005; Cemen et al., 2006; Edwards and Grasemann, 2009). It is debated if this extension is accommodated by the Simav detachment fault located in the Northern Menderes Massif (Bingol et al. 1982; Isik and Tekeli, 2001; Akay, 2009). Some geologic maps show the Egrigoz and Koyunoba plutons bounded to the west by the low-angle Simav detachment fault (Isik and Tekeli, 2001; Ring and Collins, 2005; Thomson and Ring, 2006; Westaway, 2006) while other regional maps show no offset between the Egrigoz and Koyunoba and surrounding metamorphic rocks (Ozgenc and Ilbeyli, 2008; Akay, 2009). In contrast, other maps show thrust faults present near the western boundary of the Egrigoz and eastern boundary of the Koyunoba pluton (Akay, 2009). The final stage of extension, which began around 5 Ma, is marked by normal faults throughout the Alasehir and Buyuk Menderes grabens (Cemen et al., 2006).

1.2 GEOLOGY OF THE EGRIGOZ, KOYUNOBA, AND ALACAM GRANITOIDS

The Egrigoz, Koyunoba, and Alacam granitoids are located in the hanging wall of the Simav normal fault in the northern Menderes Massif. The existence of a low angle west-dipping detachment fault along the western border of the Egrigoz and Koyunoba plutons is debated (Bingol et al. 1982; Reischmann et al., 1991; Delaloye and Bingol, 2000; Isik et al., 2004; Ring and Collins, 2005; Hasozbek et al., 2010; Ozgenc and Ilbeyli, 2008; Akay, 2009; Dilek et al., 2009; Ilbeyli and Kibici, 2009). These plutons intruded into rocks of the Menderes Massif and Afyon zone between the Simav normal fault and the Izmir-Ankara-Erzincan suture zone (i.e. Ozgenc and Ilbeyli, 2008). Based on geochemistry analyses, they were crystallized in an extensional setting during the middle Miocene (i.e. Dilek and Altunkaynak, 2007) and are part of a wider NW-SE trending magmatic belt. Shallow crustal emplacement and rapid cooling are evidenced by a chilled margin ~50-200m wide (Akay, 2009).

Although previous studies have focused on the Egrigoz, Koyunoba, and Alacam plutons, conflicting geochemical analyses (metaluminous, I-type, Ozgenc and Ilbeyli, 2008; peraluminous, I-type, calc-alkaline, Akay, 2009; peraluminous and metaluminous, I-type, shoshonitic, Ilbeyli and Kibici, 2009), unclear relationships to structures (i.e., the Simav detachment; Isik and Tekeli, 2001; Akay, 2009), and a large range in reported ages (70±7 Ma, Burkut, 1966; 167±14 Ma—29±3 Ma, Oztunali, 1973; 29±3 Ma—20.0±0.7 Ma, Bingol et al., 1982; 21.6±1.8 Ma, Delaloye and Bingol, 2000; 22.9±0.5 Ma, Isik et al., 2004; 2972±13 Ma—19.9±3.1 Ma, Ring and Collins, 2005; 21.7±1.0 Ma—19.3±4.4 Ma, Hasozbek et al., 2010) point to a complexity that may have been previously overlooked. This thesis attempts to clarify these issues using remote sensing, fieldwork, geochemical analyses, cathodoluminescence (CL) imaging, and *in situ* ion microprobe zircon geochronology.

1.3 Research Questions

Some key questions outlined by the previous work in the Northern Menderes Massif include:

1. When did the Egrigoz, Koyunoba, and Alacam plutons crystallize and what are their probable source rocks and source regions?
2. How are the Egrigoz, Koyunoba, and Alacam plutons related to one another structurally, geochemically, and tectonically?
3. How and when did the Egrigoz, Koyunoba, and Alacam plutons exhume?

The overall goal of this research is to obtain a better understanding of extensional history associated with subduction slab roll-back in western Turkey. Roll-back may occur systematically as the continental crust extends southward. Alternatively, the Aegean may experience more episodic movements that could give us a better understanding of the history of the subduction and provide insight into the consequences of the subducting plate, including roll-back and delamination.

1.4 Methods

To better understand the tectonic history of the Egrigoz, Koyunoba, and Alacam plutons, remote sensing, fieldwork, geochemical analyses, CL imaging, and geochronological studies were employed. Remote sensing was used to analyze spatial features in the Simav area and has not been previously used to examine proposed field relationships of the Egrigoz, Koyunoba, and Alacam plutons. Fieldwork focused on sample collection and the visits to proposed contacts (e.g. Isik and Tekeli, 2001; Akay, 2009). Major, minor and trace element data from collected samples was used to identify the geochemical relationship of the granites to each other and ascertain their potential source(s) (e.g., Rollinson, 2003). CL images document mineral zoning, fluid alteration, deformation, and textural relationships of zircons within the samples (e.g., Ramseyer et al., 1992; Sorensen et al., 2006; Catlos et al., 2008; 2010; 2011). Three samples from each pluton were picked for geochronological studies. Zircon was dated in thin section (*in situ*) using an ion microprobe to constrain timing of crystallization (e.g. Burkut, 1966; Bingol et al., 1982; Ring and Collins, 2005; Hasozbek et al., 2010). This is the first time zircons have been dated *in situ* for these rocks. The ion microprobe is nondestructive (e.g., Harrison et al., 1995**)** and *in situ* analyses preserve textural relationships needed to understand the ages obtained from rocks that experienced a complicated tectonic history (e.g., Catlos et al., 2002).

1.5 ORGANIZATION OF THESIS

This thesis is organized into eight chapters. Chapter 2 describes the geologic background of the Aegean region and details previous geochemical and geochronological studies of the Egrigoz, Koyunoba, and Alacam plutons. Chapter 3 describes the research methods used (remote sensing, fieldwork, geochemistry, CL image acquisition, and *in situ* ion microprobe U-Pb zircon analysis). The results of these methods are presented in chapters 4-7. Chapter 8 provides a summary of the conclusions and contributions of this thesis and proposed answers to research questions.

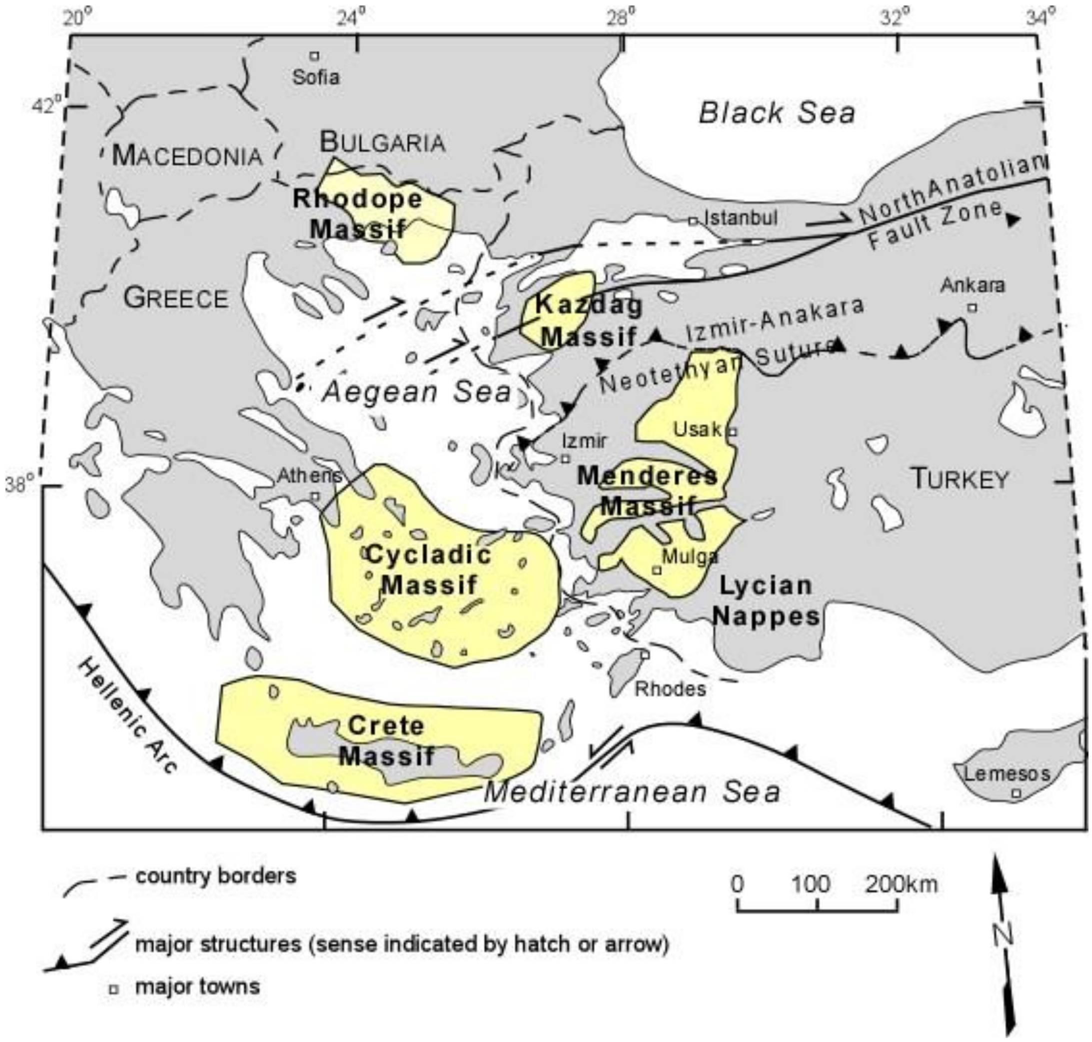

Figure 1-1: Generalized map of Aegean showing location of core complexes and other major structural elements. Black box outlines the Menderes massif. Catlos and Cemen (2005).

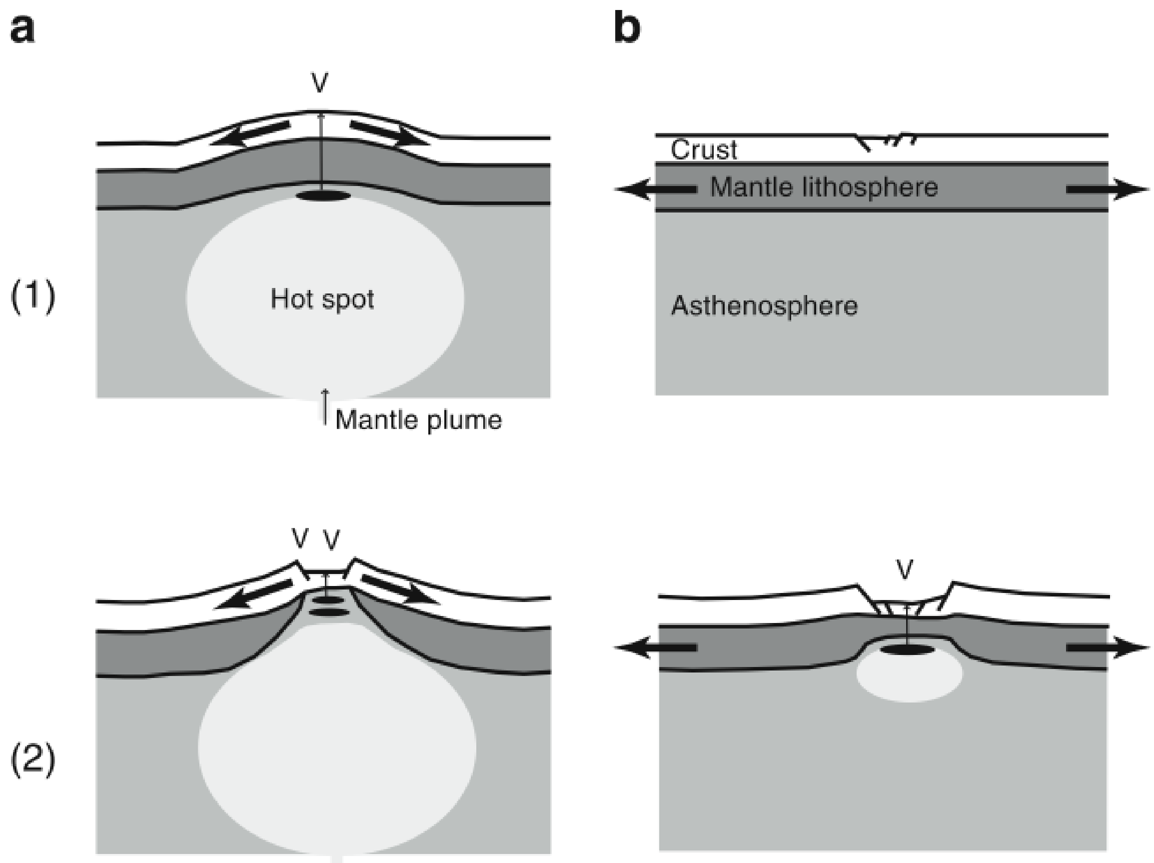

Figure 1-2: Schematic diagram of metamorphic core complex formation. (a) Active—emplacement of hot mantle plume thins and weakens crust. Isostatic crustal doming drives active extension. (b) Passive—tensional regional stresses (e.g. slab roll-back) drive extension and magmatism is a consequence of thinning. Corti et al., (2003).

Chapter 2: Geologic Background

2.1 Context of the Menderes Massif in Western Turkey

The Aegean region experienced multiple episodes of continental collision and crustal thickening during the Late Cretaceous to Eocene (Sengor and Yilmaz, 1981; Tankut et al., 1988; Cemen et al., 2006; Dilek and Altunkaynak, 2007; Moix et al., 2008; Ilbeyli and Kibici, 2009). Post-collisional extension due to slab roll-back and orogenic collapse exhumed several core complexes throughout the region (e.g. Gautier et al., 2008; Ilbeyli and Kibici, 2009) including the Menderes (Bozkurt and Park, 1994; Hetzel and Dora, 1994; Isik and Tekeli, 2001), Rhodope (Dinter and Royden, 1993), Kazdag (Okay and Satir, 2000), Cyclades (Buick, 1991; Gautier and Brun, 1994; Vandenberg and Lister, 1996), and Crete massifs (Jolivet et al., 1994; Kilias et al., 1994) (Figure 2-1). Recognizing similarities between these core complexes is important in understanding the nature and temporal evolution between shortening and extension in the Aegean area. New information will also enhance our knowledge of the history of the Northern Menderes Massif.

During the Paleocene-Eocene, the crust in the Aegean region thickened due to the closure of the Neotethys Ocean (e.g. Dilek and Altunkaynak, 2007). Ophiolites from the obduction/subduction of the Neotethys are located in the Izmir-Ankara-Erzincan suture zone (e.g., Sengor and Yilmaz, 1981; Gorur et al., 1984). Thickening is evidenced by north-vergent thrusting of nappes that comprise the Menderes Massif (e.g., Gessner et al., 2001), which is considered by Wesaway (2006) as the Earth's largest known metamorphic core complex (>40,000km^2) (Figures 2-1 to 2-4). These nappes (Bayindir, Bozdag, Cine, and Selimiye) are the rock units of the Menderes Massif and are affected by large-scale (~300km) extension that likely initiated during the Oligocene-Miocene (Gessner et al., 2001; Ring et al., 2001; Catlos and Cemen, 2005).

The Bayindir nappe is structurally lowest (Figure 2-2) and is comprised of metapelitic assemblages with amphibolite and marble lenses (Gessner et al., 2001; Ring et al., 1999; Catlos and Cemen, 2005). The sediments within the Bayindir nappe were likely deposited in the early Tertiary and metamorphosed to greenschist facies in the Eocene ($^{40}Ar/^{39}Ar$: ~37 Ma) (Lips, 2001). The Bozdag nappe overlies the Bayindir nappe and also contains metapelitic assemblages with amphibolite and marble lenses (Gessner et al. 2001). Protoliths include Precambrian metasediments and metabasites metamorphosed to amphibolite-facies in the Late Proterozoic (Ring et al., 2001). The Cine nappe overlies the Bozdag nappe, and is comprised of ortho and paragneisses (Gessner et al., 2001). The protolith, orthogneiss and metagranite, is thought to be Cambro-Ordovician (U-Pb zircon age of 551±1.4 Ma, Hetzel et al., 1998) and was metamorphosed to amphibolite-facies in the Eocene ($^{39}Ar/^{40}Ar$ muscovite ages of 43 to 37 Ma, Hetzel et al., 1998). The Selimiye nappe overlies the Cine nappe, and is comprised of a metasedimentary succession of intercalated marble and calcschist (Catlos and Cemen, 2005). The Selimiye nappe shows evidence for lower amphibolite-facies metamorphism that likely took place in the Late Proterozoic based on 549 Ma $^{206}Pb/^{207}Pb$ zircon ages of intruding metagranites (Ring et al., 2001). The Cyclades Menderes Thrust places blueschists and Lycian nappes structurally above the Selimiye nappe (Gessner et al., 2001). The Selimiye nappe, blueschists, and Lycian nappes contain evidence of high-pressure, low-temperature (High P/T) metamorphism (Fe-Mg carpholite) appropriate of a subduction zone setting (Oberhaensli et al., 2001; Rimmele et al., 2003) (Figure 2-2).

The Menderes Massif is bounded by the Izmir-Ankara-Erzincan suture to north, the Lycian nappes to the south, and the Afyon zone to the east (Moix et al., 2008). The Afyon zone is a High P/T belt that tectonically overlies the Menderes Massif (Akay, 2009). The Menderes Massif is thought to have formed in three stages (e.g. Cemen et al., 2006). Beginning in the late Oligocene and continuing into the Miocene, extension may have initiated along the north-dipping Southwest Anatolian Shear Zone by orogenic collapse of overly thickened crust (Dewey, 1988; Pinet and Coletta, 1990; Seyitoglu and Scott 1996) or back-arc spreading of the Hellenic arc (Le Pichon and Angelier, 1979; Meulenkamp et al., 1988; Seyitoglu and Scott, 1996).

The second stage of extension, which likely initiated from subduction slab roll-back (Purvis and Robertson, 2005; Edwards and Grasemann, 2009), began in the early Miocene and is evidenced by two east-west trending structures, the north-dipping Alasehir (Kuzey) and the south-dipping Buyuk (Guney) detachments (Figure 2-1 to 2-2). The Alasehir detachment extends ~180 km with a north-northwest dip of 10-20° (Isik et al., 2004). The Buyuk detachment extends roughly the same distance with a south-southwest dip of 40-60° (Hetzel et al., 1994; Gessner et al., 2001; Gurer et al., 2009). The Alasehir detachment may have initiated at a higher angle and rolled back to its present angle throughout the process of extension (Hetzel et al., 1994).

These detachments create two distinctive east-west trending grabens in the Menders Massif termed the Alasehir (Gediz) and the Buyuk Menderes grabens (Figure 2-1) (Purvis and Robertson, 2005). These accommodate extension in the region and divide the Menderes Massif into the Northern (Gordes submassif), Central, and Southern (Cine submassif) sections. The Alasehir graben contains four different sedimentary units (lacustrine, muddy-to-sandy alluvial fan, axial-fluvial, and coarse alluvial fan facies) with a total thickness of >300 m (Purvis and Robertson, 2005). Structures within the Alasehir graben (i.e. unconformities and cross-cutting high angle faults) show evidence for episodes of pulsed extension (Emre, 1988; Paton, 1992; Purvis and Robertson, 2005). The third stage of extension began in the Pliocene and is marked by faults that crosscut the Alasehir and Buyuk Menderes grabens (Purvis and Robertson, 2005). The Pliocene age was also recorded by monazite crystallization in metamorphic rocks along the Alasehir detachment surface (Catlos and Cemen, 2005).

2.2 Structural relationships of the Egrigoz, Koyunoba, and Alacam plutons

Here we focus on the Egrigoz, Koyunoba, and Alacam plutons in the Northern Menderes Massif (Figures 2-3 and 2-4) because they are the largest exhumed granitoids in the northern Menderes Massif. They lie between the Simav normal fault and Izmir-Ankara-Erzincan suture (e.g. Ozgenc and Ilbeyli, 2008). Three distinct pulses of magmatism occurred in western Anatolia following the early Eocene collision of the Anatolide-Tauride platform with the Eurasian plate (Genc, 1998; Dilek and Altunkaynak, 2007). First, Eocene to Oligo-Miocene subalkaline medium- to high-K and calc-alkaline granitoids formed in a collisional regime during closure of the NeoTethys due to increased asthenospheric heat from lithospheric slab break-off (Dilek and Altunkaynak, 2007). These rocks display a wide array of chemistries possibly due to large amounts of crustal contamination (Dilek and Altunkaynak, 2007). Middle Miocene granitoids then formed in an extensional setting that also produced extrusive mildly alkaline rocks with OIB-like geochemical analyses due to high asthenospheric mantle-derived melt contribution with little crustal contamination (Dilek and Altunkaynak, 2007). Lastly, beginning ~12 Ma and continuing into the late Quaternary, alkaline mafic magmas with progressively increasing potassic and sodic compositions were produced by decompression melting of asthenospheric mantle beneath substantially thinned continental crust (Yilmaz, 1998; Dilek and Altunkaynak, 2007). The Egrigoz, Koyunoba, and Alacam plutons are thought to be a result of the second pulse of magmatism (Akay, 2009). They are located at the eastern part of the NW-SE trending magmatic belt (Figure 2-3).

The Egrigoz, Koyunoba, and Alacam plutons are located in the hanging wall of the Simav normal fault, a high-angle (~45-60°, Seyitoglu, 1997) north-dipping listric fault extending ~150 km (Seyitoglu, 1997; Ersoy et al., 2010) (Figure 2-2 and 2-4). Some researchers (i.e. Isik and Tekeli, 2001) argue that the plutons are located in the footwall of the Simav Detachment fault but others (i.e. Akay, 2009) contend that the detachment does not exist. The Egrigoz is the largest exposed pluton, covering ~400 km^2 while the Koyunoba and Alacam granitoids are ~170 km^2 and ~60 km^2 respectively (Figure 2-4) (Isik et al, 2004; Hasozbek et al., 2010). The country rocks intruded by the plutons include Simav metamorphics and the Balikbasi, Saricasu, and Arikaya formations (Oyman et al., 2011). The Simav metamorphics are the oldest country rocks and are comprised of migmatitic-banded and biotite gneiss, high-grade schist, marble and amphibolite (Isik et al., 2003). The Balikbasi formation, consisting of laminated limestone, overlies the Simav metamorphics (Oyman et al., 2011). Unconformably above the Balikbasi, the Saricasu formation is made of Upper Paleozoic-Lower Triassic schists (Akdeniz and Konak, 1979**)**. The Arikaya overlies the Saricasu formation and contains meta-carbonate rocks and pelitic schists enclosing limestone lenses (Akdeniz and Konak, 1979).

The Egrigoz, Koyunoba, and Alacam plutons intruded into rocks of the Menderes Massif and Afyon zone after regional metamorphism was complete (Akay, 2009). Chilled margins ~50-200 m wide are evidence of rapid cooling and indicate shallow crustal emplacement (Akay, 2009). Explanations of exhumation mechanisms vary depending on the existence of the Simav detachment fault (Figure 2-3 and 2-4) (i.e. Isik and Tekeli, 2001; Akay, 2009). Based on field observations of lower-grade metamorphic rocks tectonically above higher-grade ones in the Simav area (Ring et al., 2003; Akay, 2009), some geologic maps show the Egrigoz and Koyunoba plutons bounded to the west by the low-angle Simav detachment fault (Isik and Tekeli, 2001; Ring and Collins, 2005; Thomson and Ring, 2006; Westaway, 2006). In contrast, other regional maps show no offset between the Egrigoz and Koyunoba and surrounding metamorphic rocks (Ozgenc and Ilbeyli, 2008; Akay, 2009). Thrust faults, roof pendants from the Afyon Zone, may be present near the western boundary of the Egrigoz and eastern boundary of the Koyunoba, between Menderes metamorphic rocks and a meta-rhyolite unit (Akay, 2009).

2.3 Previous Geochemical Results

Geochemical analyses of the Egrigoz, Koyunoba, and Alacam plutons range from granite to diorite (Figure 2-5 to 2-6) (Ozgenc and Ilbeyli, 2008, n=12; Akay, 2009, n=20; Erkul et al., 2010, n=11; this thesis, n=31). The granitics have been reported to range from calc-alkaline to shoshonitic, and interpretations of the tectonic setting vary. The Egrigoz pluton has been most analyzed and samples plot within the Volcanic Arc Granite (VAG) field (Ozgenc and Ilbeyli, 2008; Ilbeyli and Kibici, 2009) or between VAG and syn-collisional granites (syn-COLG) (Akay, 2009) on the Rb-(Y+Ta) discrimination diagram (Figure 2-6A). On the Nb-Y discrimination diagram (Figure 2-6B), samples plot within the VAG and syn-COLG fields (Akay, 2009) or between within plate granite (WPG) and VAG + syn-COLG granite fields (Ozgenc and ilbeyli, 2008; Ilbeyli and Kibici, 2009). Post-collisional granites cannot be distinguished between VAG and syn-COLG (Pearce et al., 1984; Rollinson, 1993)

Samples from Egrigoz pluton are metaluminous or peraluminous depending on sampling locality (Ozgenc and Ilbeyli, 2008; Ilbeyli and Kibici, 2009; Akay, 2009; Dilek et al., 2009). Both I-type and S-type granitics have been reported from the pluton

(Ozgenc and Ilbeyli, 2008; Dilek et al., 2009; Ilbeyli and Kibici, 2009). Heterogeneities within the plutons may be caused by magma mixing, partial melting, crustal contamination, and post-emplacement fluid interactions as evidenced by cathodoluminescence images (e.g. Hibbard, 1981; Purvis and Robertson, 2005; Catlos et al., 2010).

2.4 Previous Geochronological Results

The Egrigoz, Koyunoba, and Alacam plutons may have been emplaced syn-extensionally into Oligocene metamorphic rocks during the early Miocene (e.g. Seyitoglu and Scott, 1996; Hetzel et al., 1995; Ring et al., 1999; Okay and Satir, 2000; Isik and Tekeli, 2001; Isik et al, 2004; Thomson and Ring, 2006). However, reported ages from the plutons range from the Late Archean to early Miocene with other dates between these extremes (Table 2-1). The oldest age is Archean (2973±13 Ma, U-Pb, Ring and Collins, 2005), which was reported from the core of a single zircon within the Egrigoz pluton. Cambrian ages likely time events related to the Pan-African orogeny. No explanation has been provided for documented Cretaceous ages (70±7 Ma, U-Pb zircon, Burkut, 1966; 93±1 Ma, $^{206}Pb/^{238}U$ zircon, Ring and Collins, 2005), but they could be related to the closure of the Paleotethys at this time. Late Oligocene to early Miocene ages are cited as timing pluton crystallization (e.g. Ring and Collins, 2005).

2.5 Summary

Although the Egrigoz, Koyunoba, and Alacam plutons have been the subject of previous studies (e.g. Dilek et al., 2009), conflicting geochemical data, unclear structural relationships, and a range of reported ages from 2973±13 Ma (inherited zircon, U-Pb, Ring and Collins, 2005) to 19.3±4.4 Ma (U-Pb zircon, Hasozbek et al., 2010) indicates a complexity that may provide insight into the timing of granitic formation in the Aegean region. To clarify these issues, remote sensing, fieldwork, geochemical analyses, cathodoluminescence imaging, and *in situ* ion microprobe zircon geochronology were employed. These methods are described in detail in Chapter 3.

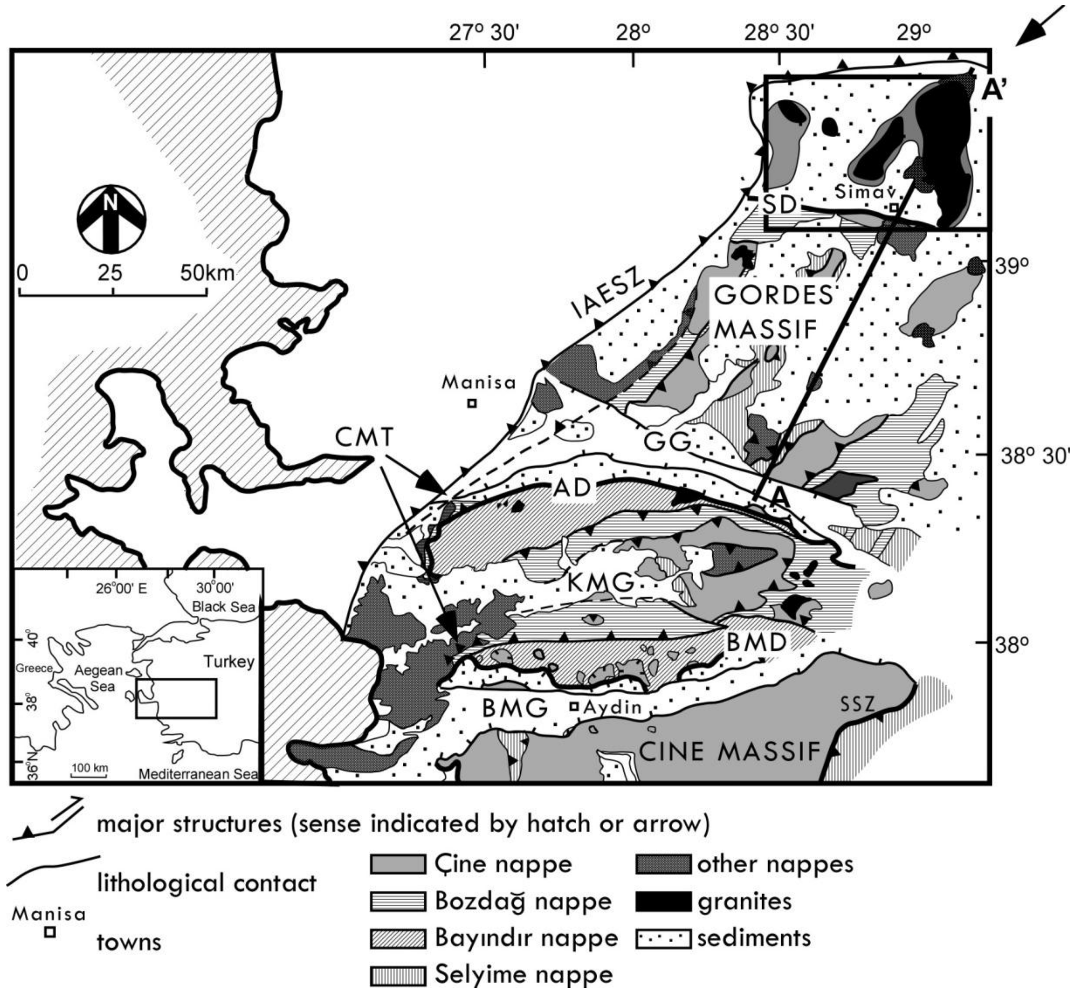

Figure 2-1: Map of the Menderes Massif after Sozbilir (2001) and Gessner et al. (2001). Inset shows the location of the massif in relation to western Turkey. Figure 2-2 shows a cross section along A-A', and 2-4 shows a geologic and sample location map of the boxed area. Abbreviations: SD= Simav Detachment; IAESZ= Izmir-Ankara-Erzincan suture zone; CMT= Cyclades Menderes Thrust, GG= Gediz Graben; AD= Alasehir Detachment; KMG= Kucuk Menderes Graben; BMD= Buyuk Menderes Detachment; BMG= Buyuk Menderes Graben.

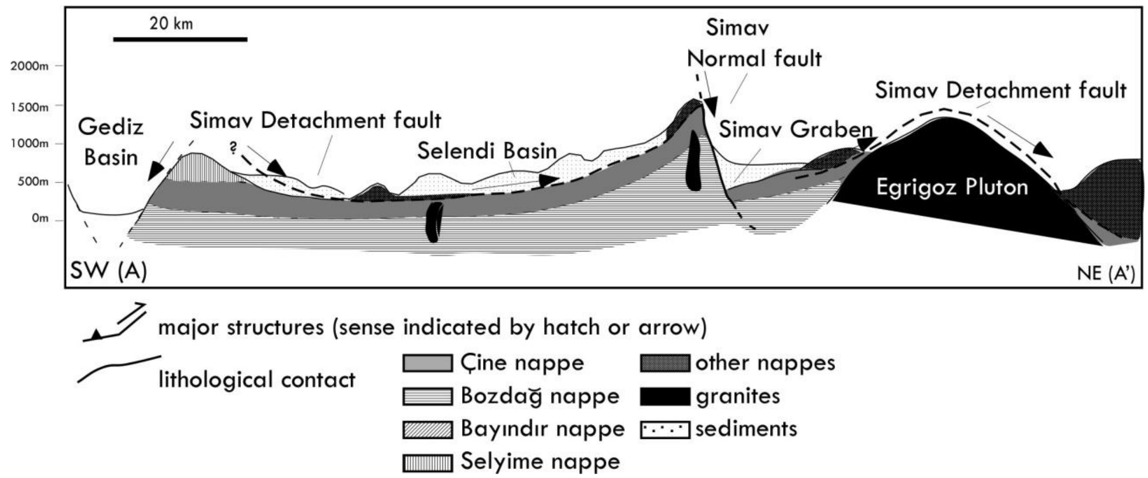

Figure 2-2: Schematic cross section of northern Menderes Massif modified after Thomson and Ring (2006). See Figure 2-1 for approximate line of section. The Simav Detachment and Bozdag, Cine, and Selimiye nappes are offset by the younger Simav normal fault. The Egrigoz Pluton shows post-kinematic doming. The Koyunoba and Alacam plutons are west of this line of section.

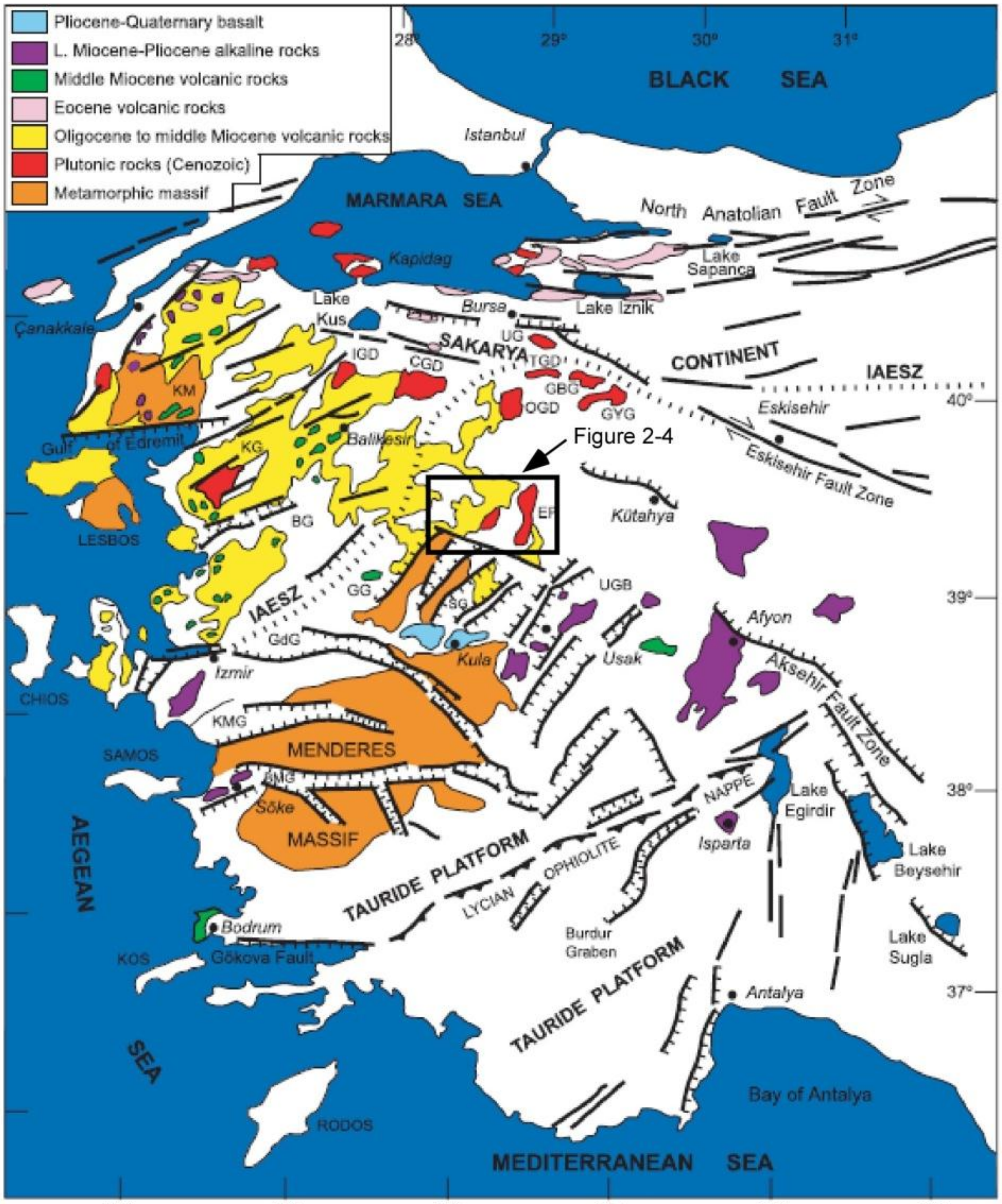

Figure 2-3: Simplified geological map of western Turkey after Altunkaynak and Dilek (2007) showing the distribution of igneous assemblages and key metamorphic massifs. Box shows location of the detailed geological map in Figure 2-4. Abbreviations: BG, Bakircay graben; BMG, Buyuk Menderes graben; CGD, Cataldag granodiorite; EP, Egrigoz pluton; GBG, Goynukbelen granite; GdG, Gediz graben; GG, Gordes graben; IAESZ, Izmir-Ankara-Erzincan suture zone; IGD, Ilica granodiorite; KG, Kozak granodiorite; KM, Kazdag massif; KMG, Kucuk Menderes graben; OGD, Orhaneli granodiorite; SG, Selendi graben; SaG, Salihli granite; TG, Turgutlu granite; TGD, Topuk granodiorite; UGB, Usak-Gure basin.

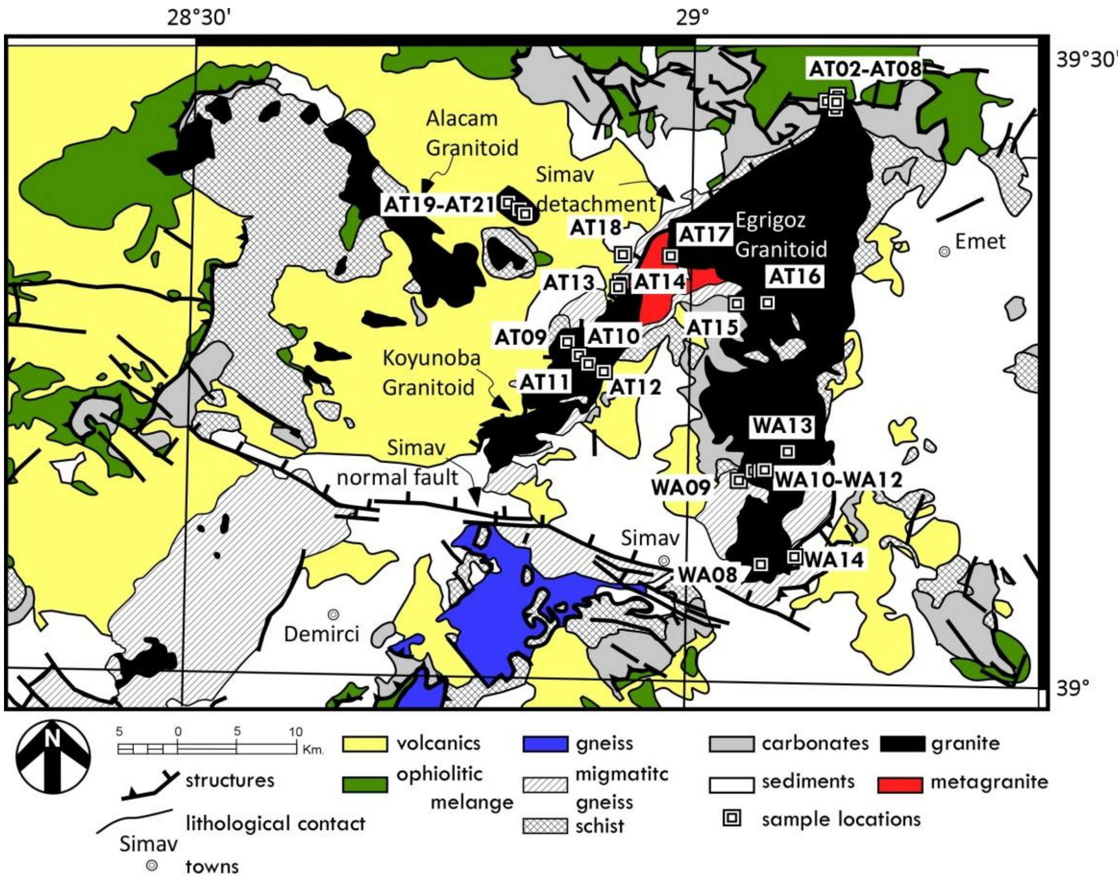

Figure 2-4: Geologic map of field area after Konak (2002) and Ring and Collins (2005). The granitoid plutons are and sample locations are indicated.

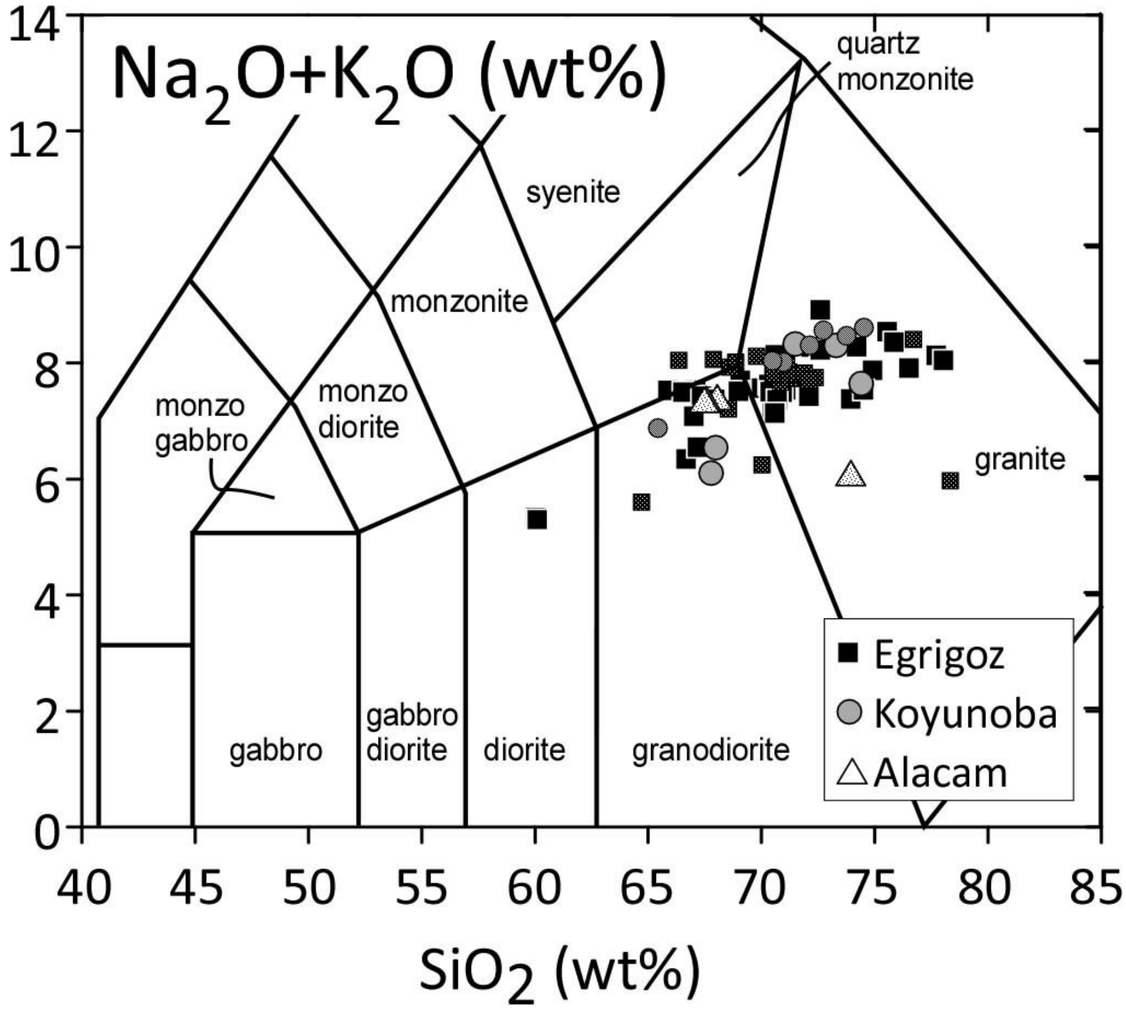

Figure 2-5: Geochemical results for the Egrigoz, Koyunoba, and Alacam plutons on the Na_2O+K_2O versus SiO_2 diagram (Middlemost, 1994). The analysis range from diorite, granodiorite, quartz monzonite, and granite fields. Data from: Ozgenc and Ilbeyli, 2008, n=12; Akay, 2009, n=20; Erkul et al., 2010, n=11; this thesis, n=31 (indicated with hatch marks).

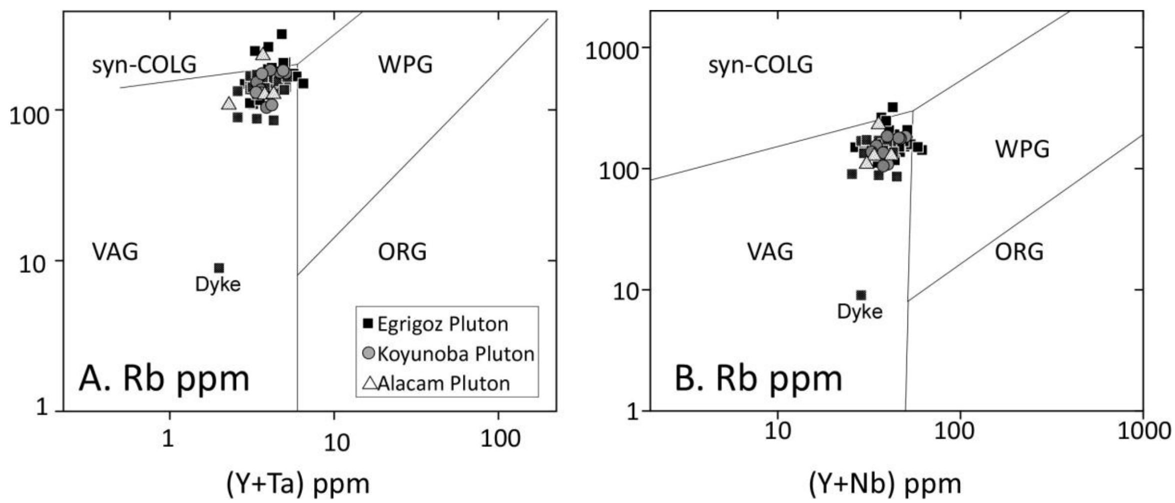

Figure 2-6: Geochemical results for the Egrigoz, Koyunoba, and Alacam plutons on (A) Rb versus (Y+Nb) and (B) Rb versus (Y+Ta) discrimination diagrams (Pearce et al., 1984). Data is the same as in Figure 2-5. Abbreviations: VAG: volcanic arc granites, WPG: within plate granites, syn-COLG: syn-collision granites, ORG: ocean-ridge granites.

Table 2-1: Previously reported ages of the Egrigoz, Koyunoba, and Alacam plutons in the Northern Menderes Massif.

Age (Ma)	Method	Interpretation	Ref.
		Egrigoz Pluton	
2972±13	$^{207}Pb/^{206}Pb$ zircon	Inherited	(1)
653±6	U-Pb zircon	Xenocryst of Pan-African orogeny	(1)
578±21	U-Pb zircon	Xenocryst of Pan-African orogeny	(1)
167±14	Rb-Sr whole rock	Unknown	(3)
70±7	U-Pb zircon	Xenocryst of unknown origin	(4)
31±5	Rb-Sr orthoclase	Unknown	(3)
29±3	Rb-Sr biotite	Unknown	(3)
24.6±1.4	K-Ar orthoclase	Pluton crystallization	(2)
22.9±0.5	$^{40}Ar/^{39}Ar$ biotite	Pluton crystallization	(5)
21.6±1.8	K-Ar orthoclase	Pluton crystallization	(6)
20.7±0.6	U-Pb zircon	Pluton crystallization	(1)
20.4±0.6	K-Ar biotite	Pluton crystallization	(5)
20.2±0.3	$^{40}Ar/^{39}Ar$ biotite	Pluton crystallization	(5)
20.0±0.7	K-Ar biotite	Pluton crystallization	(2)
19.3±4.4	U-Pb zircon	Pluton crystallization	(7)
		Koyunoba Pluton	
540±96	U-Pb zircon	Xenocryst of Pan-African orogeny	(1)
500±5	$^{206}Pb/^{238}U$ zircon	Xenocryst of Pan-African orogeny	(1)
93±1	$^{206}Pb/^{238}U$ zircon	Xenocryst of unknown origin	(1)
21.7±1.0	U-Pb zircon	Pluton crystallization	(7)
21.0±0.2	U-Pb zircon	Pluton crystallization	(1)
19.9±3.1	U-Pb zircon	Pluton crystallization	(1)
		Alacam Pluton	
38.5±1.8	K-Ar orthoclase	Pluton crystallization	(2)
27.1±1.0	K-Ar orthoclase	Pluton crystallization	(2)
20.2±0.2	Rb-Sr biotite	Pluton crystallization	(7)
20.0±0.2	Rb-Sr biotite	Pluton crystallization	(7)
20.0±3.7	U-Pb zircon	Pluton crystallization	(2)
20.2±1.4	U-Pb zircon	Pluton crystallization	(7)

References: (1) Ring and Collins (2005) (2) Bingol et al. (1982) (3) Oztunali (1973) (4) Burkut (1966); (5) Isik et al. (2004) (6) Delaloye and Bingol (2000), and (7) Hasozbek et al. (2010).

Chapter 3: Methods

3.1 Overview

This thesis reports (1) interpretations of remotely sensed images, (2) major and trace geochemical information, (3) cathodoluminescence (CL) images, and (4) U-Pb ion microprobe zircon ($ZrSiO_4$) ages from the Egrigoz, Koyunoba, and Alacam plutons. These plutons represent only a few of the granitics within the Aegean region (Figure 2-3) (Akay, 2009; Dilek et al., 2009; Hasozbek, 2010). Information regarding their structural history and chemical and geochronological relationship to other granitics in the region is important to overall understanding of extension dynamics in western Turkey (e.g., Isik et al., 2003; Ring and Collins, 2005). Remote sensing allows us to analyze spatial features and has not been used previously to examine proposed field relationships of the Egrigoz, Koyunoba, and Alacam plutons. Geochemical data is regularly used to analyze and understand geologic processes (e.g., Rollinson, 2003). Zircon is a common accessory mineral dated to constrain timing of intrusion (Ring and Collins, 2005) and CL has been stated to be "necessary to gather valid information about the tectonic evolution of granites" (Ramseyer et al., 1992). CL images document mineral zoning, fluid alteration, deformation, and textural relationships of radiogenic minerals within granitics (e.g., Ramseyer et al., 1992; Sorensen et al., 2006; Catlos et al., 2008; 2010; 2011) and help with interpretation of the zircon ages.

3.2 Remote Sensing and Fieldwork

3.2.1 Remote Sensing

The Simav normal fault is a high-angle normal fault in the northern Menderes Massif (Figures 2-1, 2-2, and 2-4; Figure 3-1). It has >200m of offset between the top of the hanging-wall and footwall (Tekeli et al., 2001; Isik et al., 2003). This fault dips steeply to the north, roughly perpendicular to extension (Strike ~270°, Dip ~60°). A second extensional structure, the Simav detachment, has also been mapped trending NE-SW along the western border of the Egrigoz and Koyunoba plutons (Figure 2-4; Figure 3-1) (Isik and Tekeli, 2001; Isik et al. 2004; Seyitoglu et al., 2004; Ring and Collins, 2005; Thomson and Ring, 2006). The main evidence for the Simav detachment are metagranites interpreted as synkinematically deformed upper portions of the Egrigoz and Koyunoba plutons (Isik and Tekeli, 2001; Isik et al., 2004; Seyitoglu et al., 2004; Thomson and Ring, 2006). The presence of this structure is debated since not all researchers believe that the Simav Detachment exists (i.e. Akay, 2009). To address this issue, geographic information system (GIS) software with detailed elevation data and a geologic map of the area where the Simav detachment is reported to be located was used to look for evidence that would denote the presence of a detachment. The Simav normal fault shows an elevation difference of ~200 m between the footwall and the hanging wall (i.e. Isik and Tekeli, 2001). If the Simav detachment exists, it should also be visible by topography. Detachments are evidenced in topography by grooved surfaces on the footwall parallel to the direction of extension (Tucolke et al., 1999; Smith et al., 2006; Spencer, 2010).

Shuttle Radar Topography Mission (SRTM) data is available with 90 m resolution. SRTM data from the United States Geological Survey (USGS) website http://dds.cr.usgs.gov/srtm/version1/Eurasia/ was downloaded and the two height (HGT) files covering the Simav field area (N39E28 and N39E29) were converted to Band Interleaved by Line (.bil) files to open in the software ArcCatalog. From ArcCatalog, the rasters were exported to a format that could be opened in the software ArcMap.

A geologic map of the field area was scanned (Konak, 2002). The image was georeferenced using six control points. Next, the image was rectified and opened as a new raster with geographic coordinates in ArcMap. This allowed SRTM data and the geologic map to be projected together. To better understand where the faults are in relationship to the granitics that they have deformed, a new polygon feature class called “granites” was created in the geodatabase within ArcCatalog. After uploading this new feature class into ArcMap, the editor was used to outline all of the granitic plutons as a separate shapefile (Figure 3-1).

Using the SRTM data and the location of the plutons in ArcGIS, a hillshade map, aspect map, and contour map were created with the Spatial Analyst tool (see Chapter 4). These maps will be used to analyze the topography of the area. A detailed road map was created by combining the location of the plutons with the location of all roads and towns on Google Maps. The road map was used during fieldwork.

3.2.2 Fieldwork Methods

Throughout the course of three days, 31 samples from 21 locations were collected (Figure 2-4). Five contacts were crossed, two of which were exposed. We focused on these specific transects: (1) from the town of Kureci to Orencik, (2) from Yesildere to Ortaca, (3) and from Camlik to Canakci (Figure 3-2). These rocks have the abbreviation of AT##. Previous samples from the Egrigoz pluton near the town of Simav were collected during a prior field season (sample numbers WA##). Fresh, unweathered samples were collected using a sledge and their GPS positions were documented. Table 3-1 reports the samples and their GPS locations.

3.3 MAJOR AND TRACE ELEMENT GEOCHEMISTRY

Geochemistry analyses are important tools to analyze the relationships between the plutons and the regional tectonic setting in which they formed (Pearce and Cann, 1971). Major and trace element geochemical analyses of the Egrigoz (21 analyses), Koyunoba (6), and Alacam (4) plutons (see Table 5-1) were performed at Activation Laboratories in Ontario, Canada. Sc, Be, V, Ba, Sr, Y, and Zr were obtained using whole rock fusion ICP methods; all other elements were obtained using whole rock fusion ICP mass spectrometry. Measured but not detected: Zn < 30 ppm, Ni and Cr <20 ppm, Cu < 10 ppm, As < 5 ppm, Mo < 2 ppm, Co and W< 1 ppm, Ag and Sb < 0.5 ppm, Bi < 0.4 ppm, and In < 0.2ppm. See Figure 2-4 for sample locations.

3.4 CL Imagery

Thin sections were examined using an optical microscope to determine the mineral assemblages. Table 3-2 reports the mineral assemblages for each collected sample. Thin sections were imaged using CL with a Premier American Technologies Luminoscope model ELM-3R in the Smithsonian Institution's Department of Mineral Sciences at the National Museum of Natural History using the same methods as outlined by Sorensen et al. (2006) (Figure 3-3). A microscope is attached to the luminoscope with an Olympus Opelco MagnaFire Model S9989 camera. An electron beam was run with operating conditions of 20kV and 0.5mA. Using a rotating red-blue-green (R-G-B) color filter wheel, three images are captured with a 1300 x 30 pixel monochrome charged-coupled device (CCD). MagnaFire software combines the three R-G-B images to produce the final image. Exposure time varies between 30 seconds to 3 minutes depending on the sample. The "brightness" and "levels" of the digital pictures were then edited in Adobe Photoshop.

CL images show textural structures that are not visible using other methods and will help us better understand the plutons' complex histories. The location of datable zircons within the CL images (e.g. in the core of a grain, in the rim of a grain, or near a vein of hydrothermal alteration) also assists in understanding the significance of the ion microprobe ages.

3.5 Geochronology

3.5.1 Scanning Electron Microscope Analysis

Three samples from the Egrigoz and two from the Koyunoba and Alacam plutons were selected for geochronological analyses. Zircons, initially detected with an optical microscope, were verified with backscattered electrons (BSE) and energy-dispersive spectrometry (EDS) using the JEOL JSM-6490 scanning electron microscope (SEM) at the University of Texas at Austin. Zircons appear bright using BSE light due to the presence of zirconium and uranium, which has the highest atomic number of all naturally occurring elements (e.g., Whitehouse et al., 1997). Standard operating conditions for the SEM were: an accelerating voltage of 15 kv, a spot size of 30 μm, and working distance of 11 mm.

After verifying zircons using the SEM, samples were prepared for the ion microprobe. Identified zircons were relocated using an optical microscope and the thin sections were cut into small pieces containing each zircon. The chips were cleaned and mounted with a pre-polished block of zircon age standards (AS3, 1099±1 Ma; Schenider et al., 1999) on dual-sided tape. A teflon ring was placed around the thin section chips and age standards. Buehler Epoxicure Resin (20-8130-032) and Hardener (20-8132-008) was then mixed and poured into the ring with a depth of 0.5 cm. After the epoxy hardened, the rings were removed from the tape and the epoxy mounts were removed of the rings. Employing an optical microscope with an automated stage and attached digital camera, a reflected light image was then acquired to assist in finding the minerals to be dated while using the ion microprobe. The mount was then cleaned and coated with gold.

3.5.2 Ion Microprobe Analysis

In situ zircon absolute age dates were obtained using the high-sensitivity/high-resolution Cameca IMS 1270 Ion Microprobe at UCLA (Figure 3-4). The ion microprobe is nondestructive (Harrison et al., 1995) and *in situ* analyses preserves textural relationships needed to understand the ages obtained from rocks that experienced a complicated tectonic history (Catlos et al., 2002).

The gold-coated epoxy mounts were loaded into the ion microprobe. Oxygen gas was leaked into the sample chamber during zircon analyses to enhance Pb isotope intensity. Energy offsets of Pb^+, U^+, and UO^+ were first determined using the standard zircons to establish the offset voltages applied during analyses. The primary beam was focused on the sample surface for an extended period of time (~3 min) to stabilize the secondary ion signal and remove surface contamination. Following presputtering, intensities were measured in 15 magnet cycles before isotopic ratios could be calculated. Age uncertainties depend on fractionation between U, Th, and Pb during ion microprobe analyses that are monitored using standards of known isotopic composition. Values plotted as $^{206}Pb^+/U^+$ RSF (relative sensitivity factor) against UO^+/U^+ are then regressed as a linear function. This allows calibrating the U-Pb sensitivity as a function of UO^+/U^+. The age of an unknown zircon is determined by applying the RSF to a measured $^{206}Pb^+/U^+$ RSF versus UO^+/U^+ zircon standard (see the UCLA National Website: http://sims.ess.ucla.edu/).

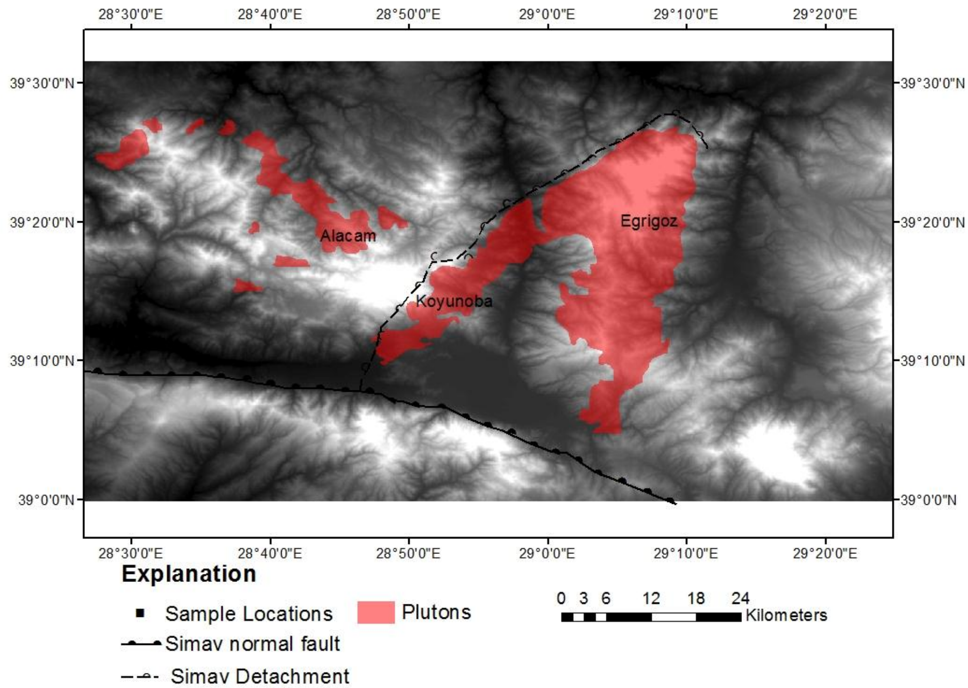

Figure 3-1: ArcGIS map of field area. The Egrigoz, Koyunoba, and Alacam plutons are shown as red polygons and projected on top of SRTM data to see elevation differences with respect to the faults.

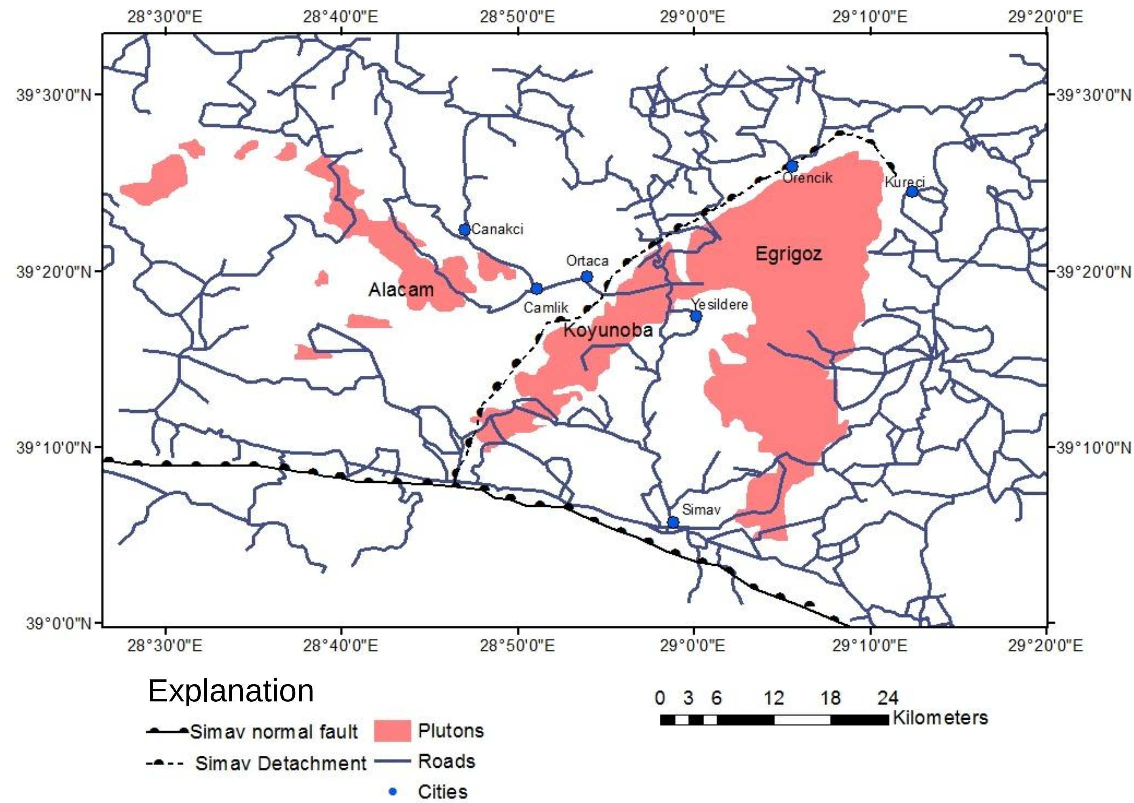

Figure 3-2: ArcMap showing the Egrigoz, Koyunoba, and Alacam plutons and their relationship to roads in the Simav area.

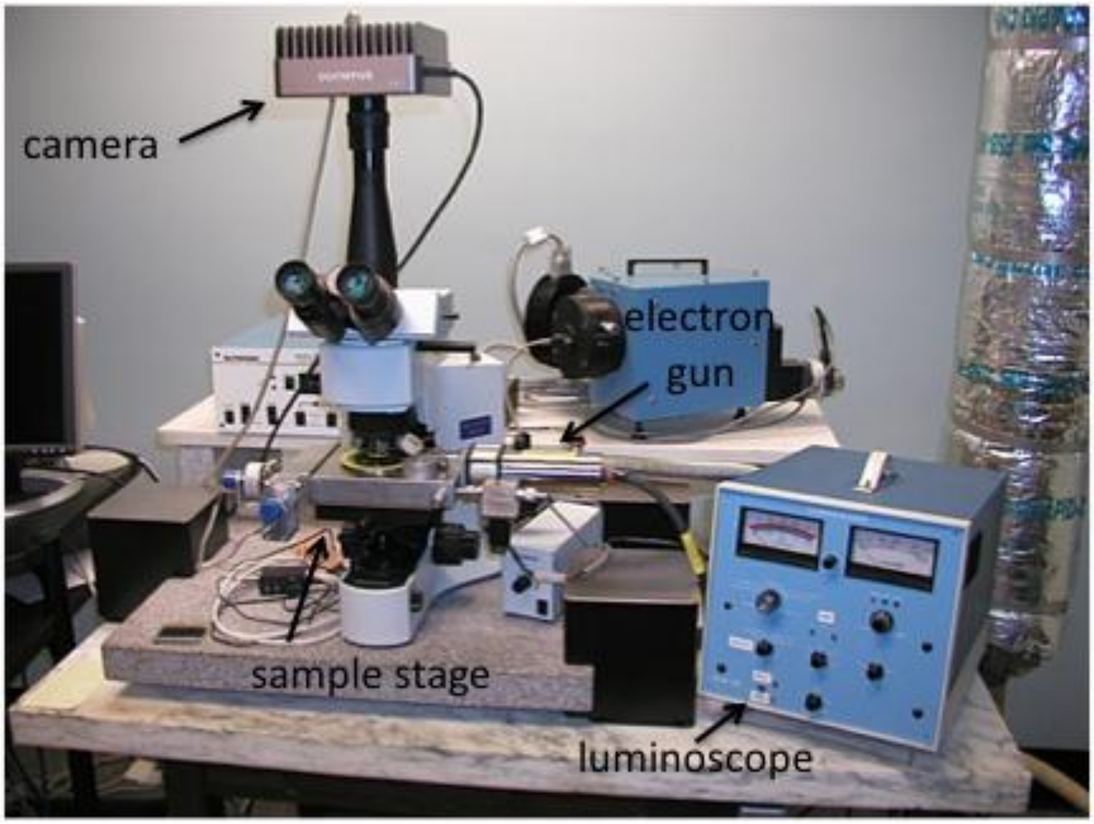

Figure 3-3: Cathodoluminescence equipment at the Smithsonian Institution National Museum of Natural History, Washington D.C.

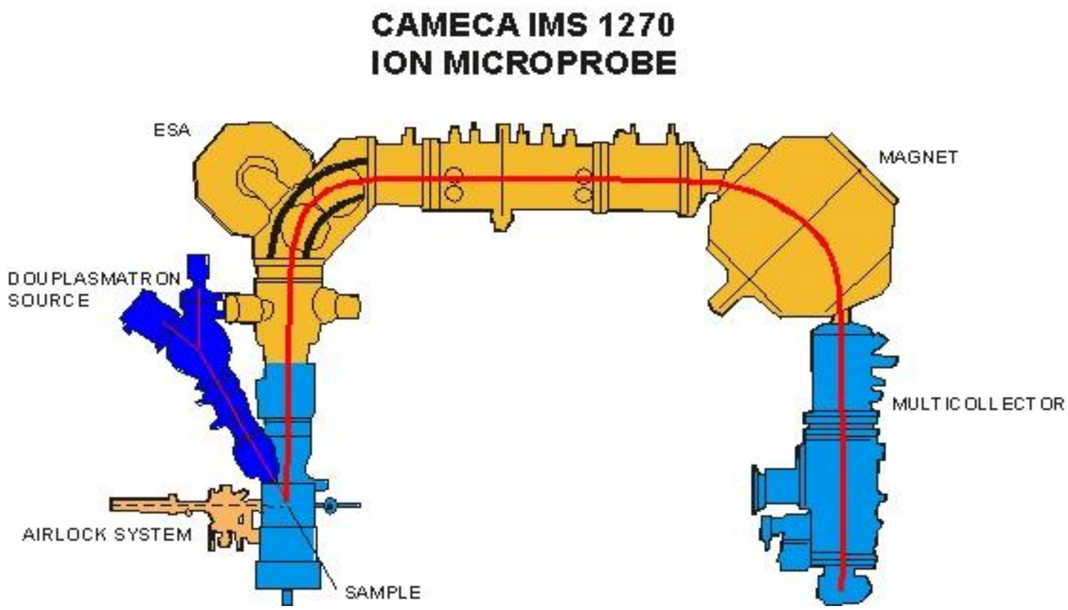

Figure 3-4: Schematic drawing of the high-sensitivity/high-resolution Cameca IMS 1270 Ion Microprobe at UCLA. The airlock system allows samples to be interchanged. The duoplasmatron is the source of primary oxygen ions. Secondary ions from the sample are moved from the sample surface through the ESA (electrostatic analyzer) a magnet, and are then detected at the multicollector.

Table 3-1: Samples and locations.

Sample Number	Location	
	Egrigoz Pluton	
WA08	39° 04' 14.20" N	29° 03' 22.60" E
WA09	39° 08' 08.60" N	29° 02' 00.20" E
WA10	39° 08' 35.10" N	29° 02' 42.90" E
WA11	39° 08' 36.10" N	29° 03' 10.40" E
*WA12	39° 08' 34.90" N	29° 03' 24.70" E
WA13	39° 09' 32.20" N	29° 04' 46.40" E
WA14	39° 04' 38.00" N	29° 05' 16.70" E
AT02	39° 26' 02.60" N	29° 07' 00.50" E
AT03	39° 25' 37.90" N	29° 07' 22.40" E
AT04	39° 25' 42.10" N	29° 07' 18.20" E
*AT05	39° 25' 43.40" N	29° 07’ 18.20" E
AT06	39° 25' 49.30" N	29° 07' 15.50" E
AT07	39° 26' 08.60" N	29° 07' 21.80" E
AT08	39° 26' 02.60" N	29° 07' 00.50" E
AT15	39° 16' 22.00" N	29° 01' 36.40" E
*AT16	39° 16' 30.10" N	29° 03' 25.50" E
	Koyunoba Pluton	
AT09	39° 14' 21.50" N	28° 51' 36.50" E
AT10	39° 13' 48.50" N	28° 52' 20.30" E
AT11	39° 13' 23.20" N	28° 53' 00.40" E
*AT12	39° 13' 07.10" N	28° 53' 43.60" E
AT13	39° 17' 08.70" N	28° 54' 39.40" E
*AT14	39° 16’ 59.06” N	28° 54’ 30.70” E
AT17	39° 18' 35.40" N	28° 57' 35.10" E
	Alacam Pluton	
*AT19	39° 20' 22.30" N	28° 49' 01.20" E
*AT20	39° 20' 34.60" N	28° 68' 31.80" E
AT21	39° 20' 49.00" N	28° 47' 59.50" E

*dated samples

Table 3-2: Mineral assemblages of the Egrigoz, Koyunoba, and Alacam pluton samples. Abbreviations after Kretz (1983).

Sample	Mineral Assemblages
	Egrigoz Pluton
WA08	Qtz+Pl+Bt+Kfs+Ap+Zrn+Xt+FeO+FeSi
WA09	Qtz+Bt+Pl+Kfs+Ms+Zrn+Mnz
WA10	Qtz+Kfs+Pl+Bt+Ep+Zrn
WA11	Qtz+Pl+Kfs+Bt+Ms+Cal+Spn+Rt+Zrn+Mnz
WA12	Qtz+Bt+Ms+Pl+Kfs+Ap+FeO+Zrn
WA13	Qtz+Pl+Kfs+Bt+Ms+Ilm+Ap+Aln+Brt+FeO
WA14	Qtz+Pl+Ms+Kfs+Bt+Ap+Zr+Rt+Zrn+FeO
AT02	Qtz+Pl+Bt+Kfs+Ms+Alu+Ap+Chl+Px+Zrn+Mnz+Hem+Cal
AT03	Qtz+Pl+Kfs+Bt+Ms+Hbl+Ep+Chl+Cal+Zrn
AT04	Qtz+Pl+Kfs+Bt+Px+Ap+Hbl+Cal+Chl+Zrn
AT05	Qtz+Kfs+Bt+Pl+Chl+Ap+Zrn+Rt+Cal+FeO
AT06	Qtz+Kfs+Pl+Bt+Chl+FeO+Ap+Zrn+Spn
AT07	Qtz+Pl+Kfs+Bt+Ms+Py+Hbl+FeO
AT08	Qtz+Pl+Hbl+Kfs+Bt+Chl+Zrn
AT15	Qtz+Pl+Kfs+Bt+Ms+Zrn+Chl+Ilm+Hbl+Mag
AT16	Qtz+Bt+Pl+Kfs+Ap+Chl+Ms+Zrn
	Koyunoba Pluton
AT09	Qtz+Kfs+Pl+Bt+Ms+Hbl
AT10	Qtz+Bt+Pl+Kfs+Ap+Hbl+Zrn+Mnz
AT11	Qtz+Pl+Kfs+Bt+Cal+FeO
AT12	Qtz+Bt+Kfs+Pl+Zrn+Ap+FeO
AT13	Qtz+Pl+Kfs+Bt+Ms+Ap+FeO+Zrn
AT14	Qtz+Pl+Kfs+Bt+Ms+FeO+Ap+Ilm+Rt+Zrn+Mnz
AT17	Qtz+Pl+Kfs+Bt+Zrn
	Alacam Pluton
AT19	Qtz+Pl+Kfs+Bt+Ap+Zrn+Rt+Cal+FeO
AT20	Qtz+Kfs+Pl+Bt+Ilm+Ms+Rt+Ap+Cal+Zrn

Chapter 4: Remote Sensing Results and Discussion

4.1 INTRODUCTION

There are two proposed major structures in the field area: the Simav normal fault and the Simav detachment (Figure 2-4). The well-documented E-W trending Simav normal fault (e.g. Konak, 1979) extends approximately 150 km between the towns of Banaz in the east and Sindirgi in the west and shows significant elevation contrasts between the footwall and the hanging wall (Seyitoglu, 1997; Ersoy et al., 2010) (>200m; Figure 4-1). The fault has an average dip of 45-50º (Seyitoglu, 1997) and is thought to have formed during Pliocene to recent extension (Seyitoglu, 1997; Ring and Collins, 2005). The Simav detachment, thought to be active between 24-19 Ma, may be located along the western border of the Koyunoba and Egrigoz pluton (Ring and Collins, 2005) and accommodated ~50 km of NE-SW extension (Tekeli et al., 2001; Isik et al., 2003). The existence of the Simav detachment along the western border of the Egrigoz and Koyunoba plutons is debated (Figure 4-2) (Bingol et al. 1982; Reischmann et al., 1991; Delaloye and Bingol, 2000; Isik et al., 2004; Ring and Collins, 2005; Hasozbek et al., 2010; Ozgenc and Ilbeyli, 2008; Akay, 2009; Dilek et al., 2009; Ilbeyli and Kibici, 2009). To address this, Shuttle Radar Topography Mission (SRTM) data was analyzed using ArcGIS to determine if the topography changes exist that suggest the occurrence of the NE-SW trending detachment on the western border of the plutons. Detachments are evidenced in topography by grooved surfaces on the footwall parallel to the direction of extension (Tucolke et al., 1999; Smith et al., 2006; Spencer, 2010).

The final product has two components: elevation maps that focus on the topography of the granitic outcrops and their relationship to faults (Figures 4-1, 4-3 - 4-6) and a map that shows the location of the granitics (Figure 4-7). The elevation maps are used to determine if topography is consistent with the presence of a detachment fault along the western border of the Egrigoz and Koyunoba plutons. The road map was used in the field to locate the sampled granitics (Figure 2-4). The contour map (Figure 4-1) and elevation map (Figure 4-3) show the topography of the area. The slope raster (Figure 4-4) was used to distinguish dip inclination. Areas of steep deep are shown in red and flat areas are shown in green. The hillshade raster (Figure 4-5) highlights dip direction and topography and the aspect raster (Figure 4-6) simply differentiates areas of different dip direction.

Remote sensing is often used to obtain structural geological information without intense fieldwork (i.e., Fernandes et al., 2005). Observable features include rock foliation and tectonic structures (Price and Cosgrove, 1990; Hancock, 1991; Angelier, 1994; Dunne and Hancock, 1994; Burbank and Anderson, 2001). Areas of extension exhibit high-angle normal faults and open tensile fractures trending perpendicular to extension (Fernandes et al., 2005). Detachment faults may be indicated by grooved surfaces on the footwall parallel to the direction of extension (Tucholke et al., 1999; Smith et al., 2006; Spencer, 2010). Although remote sensing has been applied to Turkey (i.e. Dohnt, 2006; Ozeren and Holt, 2010), no studies have focused on the Simav region.

4.2 The Simav detachment debate

Exhumation of the Menderes Massif has been attributed to several detachments (e.g. the Alasehir and Buyuk detachments) with both top-to-the-north and top-to-the-south sense of shear (Hetzel et al., 1995; Ring et al., 1999; Bozkurt and Sozbilir, 2004; Isik et al., 2004; van Hinsbergen and Boekhout, 2009). Detachments are most evident where they juxtapose high-grade metamorphic rocks of the footwall against upper-crustal rocks of the hanging wall (van Hinsbergen and Boekhout, 2009). Metagranites near the Egrigoz, Koyunoba, and Alacam plutons interpreted as synkinematically deformed upper portions of the plutons are the main evidence supporting the Simav detachment (Isik and Tekeli, 2001; Isik et al., 2004; Seyitoglu et al., 2004; Thomson and Ring, 2006). However, new field evidence from Akay (2009), including crosscutting relationships between the plutons and foliation planes of metagranites and an abrupt change in metamorphism between the undeformed plutons and surrounding metamorphosed country rock, shows that the plutons intruded into rocks of the Menderes Massif and Afyon zone after tectonic assemblage and metamorphism were complete. In addition, the metagranites of the Menderes Massif and Afyon zone are not genetically related to the plutons because, based on U-Pb zircon ages, the granitics' emplacement postdates the assemblage of the Menderes Massif and Afyon zone (Akay, 2009) and therefore the presence of a detachment fault is not needed to explain the juxtaposition of different metamorphic grades. This thesis addresses the question of the presence of the Simav detachment using remotely sensed data.

4.3 Data

The E-W trending Simav normal fault can be clearly seen by the contour map (Figure 4-1). The fault has an average elevation difference of >200m between the hanging wall and the top of the footwall. However, the Simav detachment on the western boundary of the Egrigoz and Koyunoba plutons is not evident by elevation data alone. A map with 100m contours highlighting the Simav normal fault and proposed detachment fault is shown in Figure 4-1. The Simav normal fault can be easily mapped by following the contours but the Simav detachment cuts across lines of different elevation.

The SRTM data shows a defined elevation difference between the footwall and hanging wall of the E-W trending Simav normal fault (Figure 4-3). However, as with the contour map, the inferred NE-SW Simav detachment fault does not follow any obvious elevation trends. Analyzing the slope raster (Figure 4-4), a steep slope marks the boundary between the hanging wall and the footwall of the E-W trending Simav normal fault but the NE-SW trending Simav detachment cuts across changes in slope steepness. The hillshade raster shows ~E-W lineations (Figure 4-5) likely due to large-scale ~N-S extension (ten Veen et al., 2009) that are more defined in the hanging wall of the main Simav normal fault. These lineations parallel the Simav normal fault but cross the inferred Simav detachment with no offset. If this detachment exists, a difference in lineations between the eastern footwall and the western hanging wall would be expected. However, the hillshade data shows no offset between the inferred hanging wall and footwall, implying that no detachment fault is present at that location. No grooves parallel to extension are seen in the proposed footwall to indicate the presence of a detachment.

The aspect raster map (Figure 4-6) shows the Simav normal fault dipping steeply towards the north. However, the NE-SW trending inferred detachment fault cuts across changing dip directions throughout the extent of the fault.

As we did not see the inferred structure in the remotely sensed images, we targeted five specific contacts to ascertain the presence of the Simav detachment. Only two of the five contacts were exposed. The northern Egrigoz pluton (Figure 2-4, near sample AT02) is bordered by skarn 10-100 meters thick (Oyman et al., 2011). Skarn is metasomatised zones of wall rock adjacent to granitics (e.g., Einaudi and Burt, 1982). No fault exists between the Egrigoz pluton and the country rock it intruded at this location (Figure 4-8). The western border of the Koyunoba was covered by Neogene (Isik et al., 2003) volcanic tuff (Figure 2-4; near sample AT18) therefore the existence of a detachment fault could not be determined. A high angle normal fault, as evidenced by slickenlines and steps, (strike 336°, dip 67° NE) was found along the border of the Egrigoz pluton and the Simav graben (Figure 4-9; Figure 2-4, Sample AT15). This fault may be related to the lineations seen in the hillshade image (Figure 4-5). Note that the Simav detachment has an expected low dip angle (Isik and Tekeli, 2001).

4.4 Discussion

Digital elevation data of the Simav area shows strong evidence of NNE-SSW extension. However, based on elevation data, no evidence supports that the low angle Simav detachment exists along the western border of the Egrigoz and Koyunoba plutons. The inferred detachment follows no elevation trends and cuts across changes in dip direction. There is no offset of extension lineations between the inferred footwall and hanging wall and no grooves paralleling extension were found on the footwall. Extension lineations continue across plutons inferring that extension continued after the exhumation of the plutons. This is consistent with sedimentary records found in the Alasehir graben that suggest pulsed extension continued into the Quaternary (e.g., Purvis and Robertson, 2005). Fieldwork in the Simav area also found no evidence of a detachment fault.

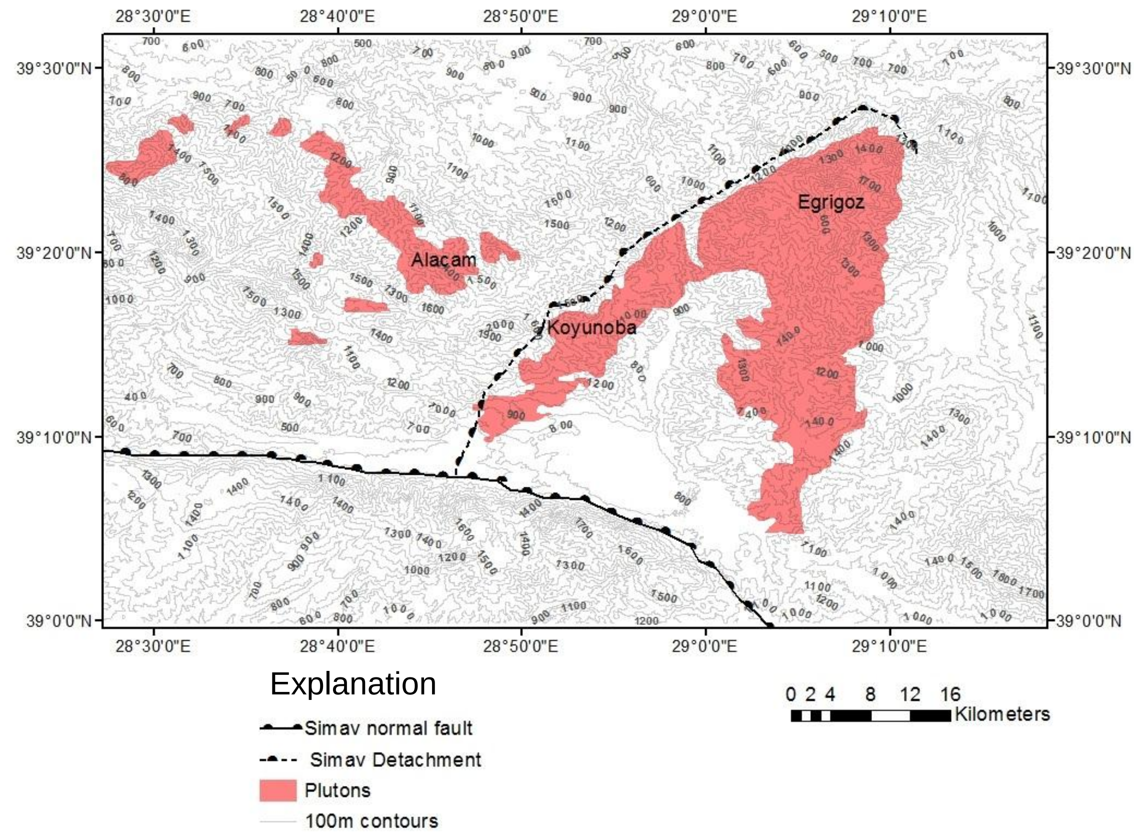

Figure 4-1: ArcMap showing the Egrigoz, Koyunoba, and Alacam plutons, 100m contours obtained from the SRTM data, and the location of the Simav normal fault and Simav detachment (after Konak, 2002). The E-W trending detachment is marked by an elevation difference of >200m and the NE-SW trending inferred detachment cuts across contour lines.

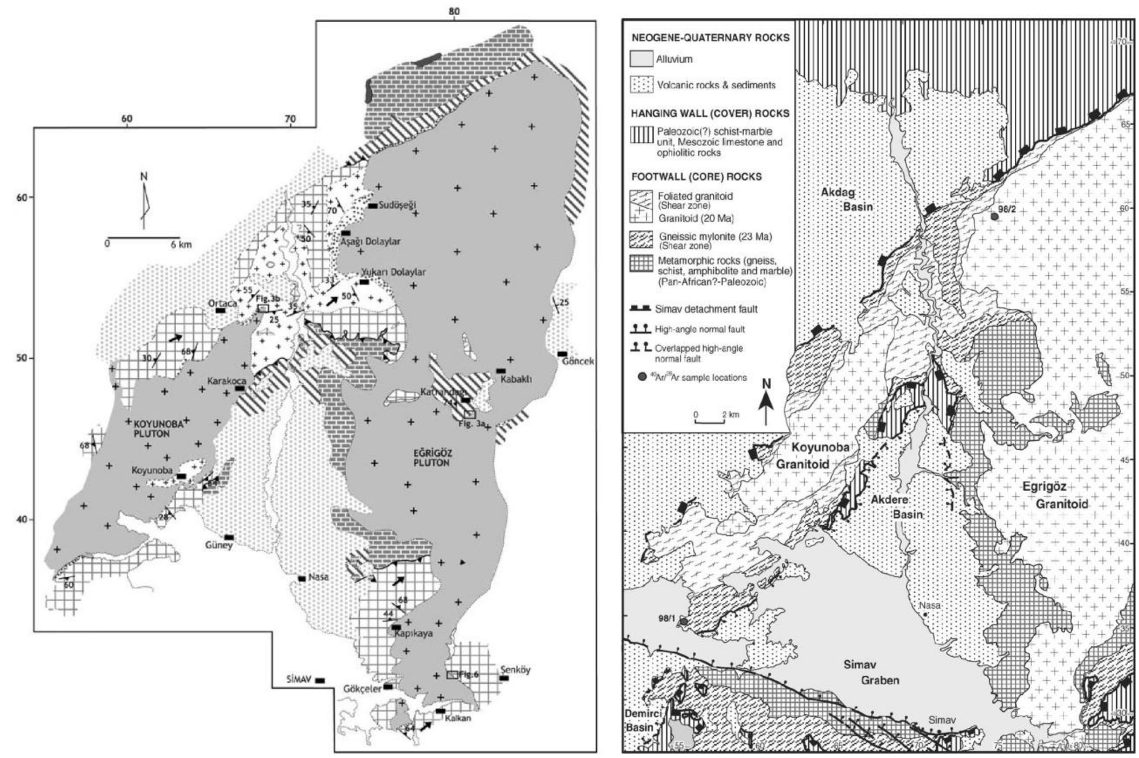

Figure 4-2: Two geologic maps of the Egrigoz and Koyunoba plutons. (A) Geologic map shows no detachment fault along the western border of the plutons (Akay, 2009). (B) Geologic map shows the Simav detachment along the western border of the plutons (Isik et al., 2004).

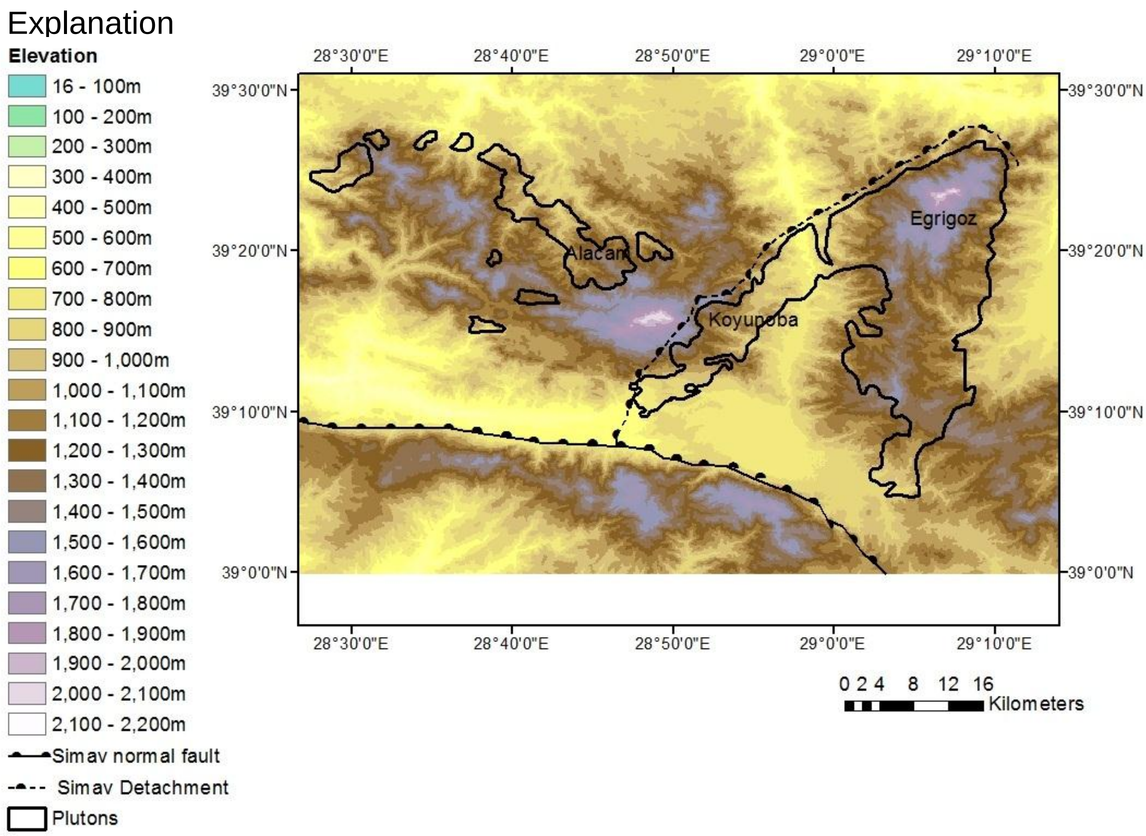

Figure 4-3: ArcMap showing the granitics and the Simav normal fault and Simav detachment fault with respect to SRTM elevation data. The E-W trending Simav normal fault follows the valley highlighted by the SRTM data. The NE-SW trending Simav detachment does not follow any elevation trends.

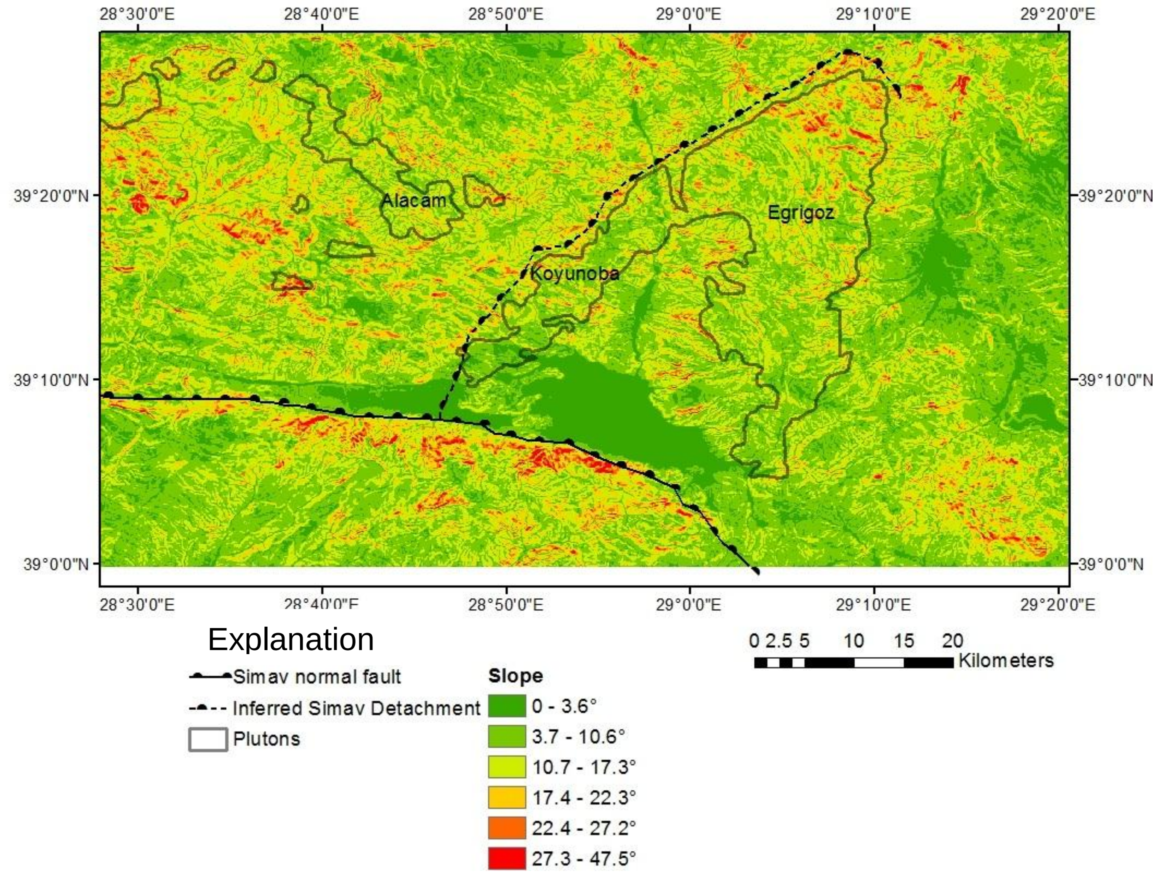

Figure 4-4: ArcMap of the classified slope raster. Colors are classified by degree of slope with green representing shallow slope and red steeper slopes. The E-W trending Simav normal fault follows a steep slope that marks the boundary between an area of high elevation and a valley. The NE-SW trending Simav detachment does not follow any obvious slope trends.

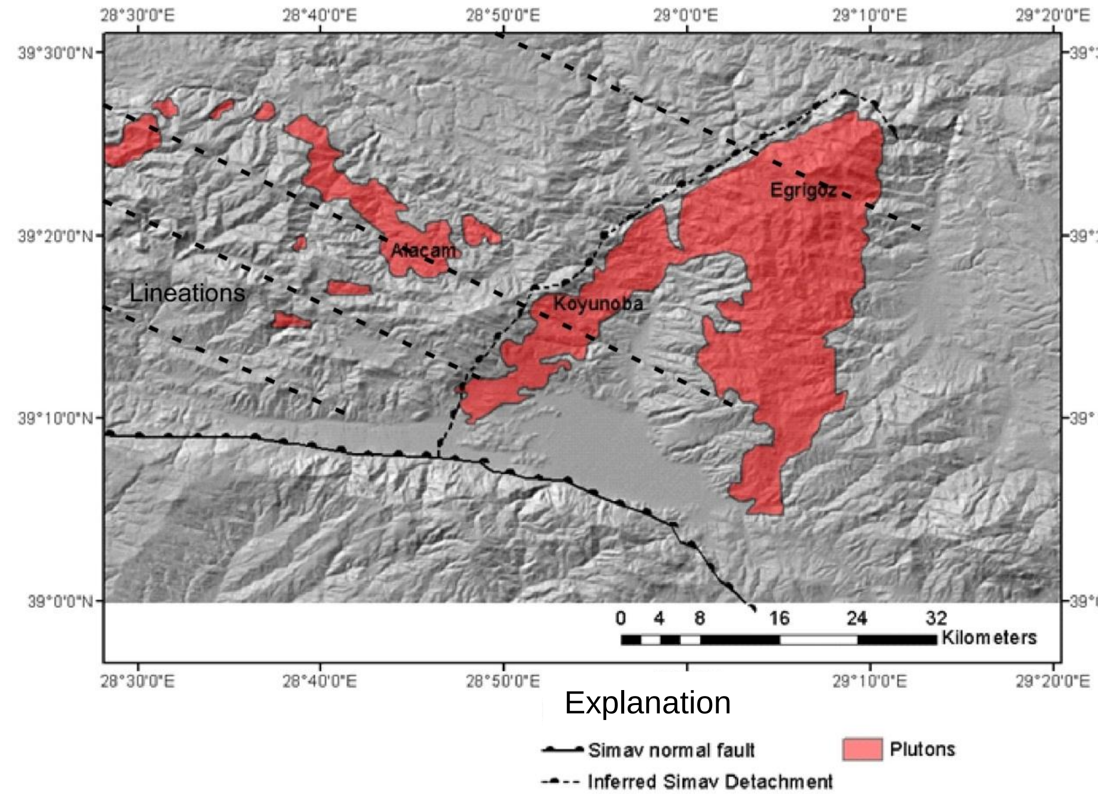

Figure 4-5: ArcMap Hillshade raster. The hillshade raster shades direction of slope dip. Notice the E-W trending lineations perpendicular to N30°E extension. Lineations can be seen cutting across proposed Simav detachment with no obvious offset.

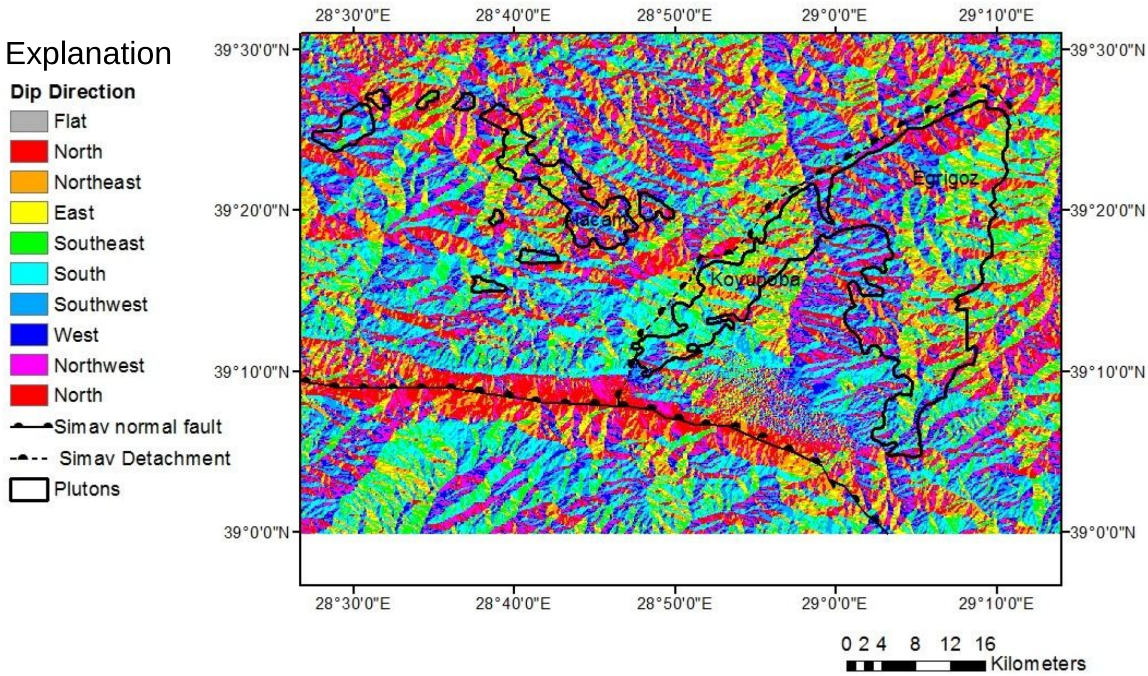

Figure 4-6: ArcMap Aspect raster with location of granitics outlined in black. Slopes are colored based on dip direction. E-W trending lineations likely caused by N-S extension (ten Veen et al., 2009) are visible. The E-W trending Simav normal fault follows a NNE dip direction and the NE-SW Simav detachment cuts across slopes dipping in different directions.

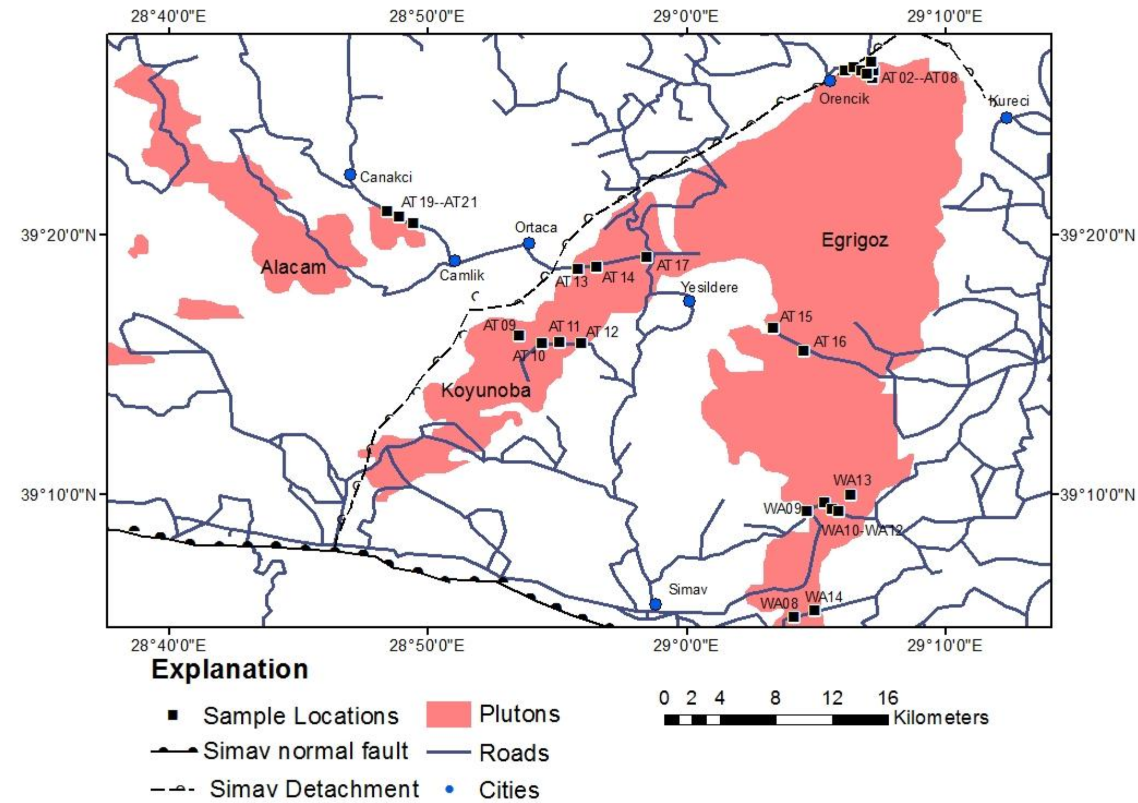

Figure 4-7: ArcMap showing the Egrigoz, Koyunoba, and Alacam plutons and their relationship to roads in the Simav area.

Figure 4-8: Skarn bordering northern Egrigoz pluton (near 39° 26' 02.60" N and 29° 07' 00.50" E).

Figure 4-9: Fault located on the western side of the Egrigoz pluton (39° 16' 22.00" N 29° 01' 36.40" E). Slickenlines and steps indicate normal sense of shear.

Chapter 5: Geochemical Results and Discussion

5.1 Introduction

Major and trace geochemical analyses from the Egrigoz, Koyunoba, and Alacam plutons are listed in Tables 5-1—5-6. Mineral assemblages are listed in Table 3-2. The data was plotted in a series of diagrams to attempt to distinguish the nature of the magma and their tectonic environment. Geochemical results from previous studies are also included in the diagrams (Ozgenc and Ilbeyli, 2008; Akay, 2009; Erkul, 2010). As described in Chapter 2, these granitics are reported to be metaluminous or peraluminous (Ozgenc and Ilbeyli, 2008; Dilek et al., 2009; Ilbeyli and Kibici, 2009; Akay, 2009), I-type or S-type (Ozgenc and Ilbeyli, 2008; Dilek et al., 2009; Ilbeyli and Kibici, 2009), and calc-alkaline to shoshonitic. Heterogeneities within the plutons may be caused by magma mixing, partial melting, crustal contamination, and post-emplacement fluid interactions (Hibbard, 1981; Rollinson, 1993; Andersson and Eklund, 1994; Janousek et al., 2004; Purvis and Robertson, 2005; Pietranik and Waight, 2008; Catlos et al., 2010).

5.2 Data

5.2.1 Major Elements

The Egrigoz, Koyunoba, and Alacam plutons range from granite to granodiorite on the total alkali ($Na_2O + K_2O$ wt. %) vs. silica (SiO_2) classification diagram (after Le Maitre, 1989; Wilson, 1989) with the exception of one Egrigoz sample that plots as a quartz monzonite and one Egrigoz sample that plots as a diorite (sample AT02A from the skarn zone) (Figure 5-1). Silica content from these samples ranges from ~60-78% (Tables 5-1—5-3).

Peraluminous rocks have another aluminous phase other than feldspar. These rocks have an aluminum-saturation index (ASI, Al/(Ca-1.67P+Na+K) > 1 in cation proportions whereas metaluminous rocks have no leftover aluminum after the crystallization of feldspars and an ASI < 1 (Frost et al., 2001). All samples from the plutons described in this thesis are peraluminous using the ASI vs. SiO_2 (wt%) (Frost et al., 2001). Most samples are peraluminous also using the Al_2O_3/(CaO+Na_2O+K_2O) vs. Al_2O_3/Na_2O+K_2O) discrimination diagram (Figure 5-2, Figure 5-3). The primary difference between the figures is that the ASI calculates aluminum-saturation based on weight percent whereas the Al_2O_3/(CaO+Na_2O+K_2O) vs. Al_2O_3/Na_2O+K_2O) diagram uses cations. Peraluminous magmas are may be formed from water-excess melting of mafic rocks (Ellis and Thompson, 1986) or melting pelitic or semi-pelitic rocks (Holtz and Johannes, 1991).

The Egrigoz, Koyunoba, and Alacam plutons are classified as S-type granitics using the Al_2O_3/(CaO+Na_2O+K_2O) vs. wt. % Fe_2O_3 discrimination diagram (Figure 5-4). S-type granitics are thought to form from melted metasedimentary rocks and are commonly strongly peraluminous with high silica contents (Chappell and White, 1974; Frost et al., 2001). I-type granitics are typically metaluminous and have high sodium contents and a wide range of silica contents (Frost et al., 2001). All samples collected from the Egrigoz, Koyunoba, and Alacam plutons plot within the S-type range on the Al_2O_3/(CaO+Na_2O+K_2O) vs. Fe_2O_3 diagram (Figure 5-4). Some researchers believe that this classification is unreliable because S-type granitics can also be produced from partial melting of a variety of sources (e.g., Miller, 1985)

Using the Modified Alkali-Lime index (MALI, Na_2O + K_2O - CaO, Frost et al., 2001) the majority of samples plot as calcic-alkalic (Figure 5-5). One Egrigoz and one Koyunoba sample plot within the calcic range, and six Egrigoz and five Koyunoba samples plot within the alkalic-calcic range. Variations are due to the magmatic source or differentiation history (Frost et al., 2001). The composition and abundances of feldspars and quartz control the MALI index. Higher MALI numbers result from increasing ratios of potassium feldspars relative to plagioclase (Frost et al., 2001). Calcic-alkalic rocks are typical of volcanic arc granites and show evidence for fractional crystallization and magmas have evidence of assimilation of host rock (Rollinson, 1993). MALI numbers tend to become more alkalic as volcanic arc plutons move farther from a subduction zone due to a decreasing continental crust contribution (Frost et al., 2001). Plutons containing both calcic-alkalic and alkalic-calcic samples, as seen in the Egrigoz and Koyunoba plutons, suggest magma mixing because fractional crystallization of the melt should trend parallel to MALI (Frost and Frost, 2008).

The $FeO^{tot}/(FeO^{tot}+MgO)$ vs. SiO_2 diagram (Frost et al., 2001) is used to understand the differentiation history of the magmatic source. Magmas enriched in iron during differentiation are classified as ferroan whereas magmas enriched in magnesium during differentiation are classified as magnesian. Magnesian granitoids are typical of subduction zones because they are relatively oxidized during differentiation (Frost and Lindsley, 1991; Frost et al., 2001) and ferroan granitoids source from anhydrous reduced magmas typical of extensional environments (Frost et al., 2001). The Egrigoz, Koyunoba, and Alacam plutons range from magnesian to ferroan, and become more ferroan with increasing SiO_2 (Figure 5-6).

In general, potassium increases with increasing SiO_2 whereas aluminum, iron, calcium, magnesium, phosphorus, manganese, and titanium decrease. Sodium remains constant with increasing SiO_2. The trends are consistent with fractional crystallization of plagioclase, alkali feldspar, amphiboles (hornblende), biotite, muscovite, quartz, magnetite, and titanite minerals. Figures 5-7 and 5-8 show patterns consistent with fractional crystallization common in granites.

5.2.2 Trace Elements

Trace elements are often assumed to be unaffected by deformation occurring after granitic crystallization (e.g. Pearce et al., 1984) and are, therefore, important in understanding the original tectonic setting of the pluton. However, Rb can be mobilized during hydrothermal fluid alteration events (Mukasa and Henry, 1990) and may give invalid results. Using the Rb vs. (Y+Nb) discrimination diagram, most samples of the plutons analyzed in this study formed in a volcanic arc typical of granitics in the overriding plate of a subduction zone with the exception of one Egrigoz sample (Sample #1401, Akay, 2009) that plots closer to the syn-collisional granite field and one Egrigoz sample (WA11B) that plots in the within-plate granite field (Figure 5-9). These discrepancies could be due to a complex tectonic history including hydrothermal fluid alteration, melting of host rocks during crystallization, magma mixing, depth of emplacement, and crystal settling.

The Egrigoz, Koyunoba, and Alacam plutons have similar chondrite-normalized rare earth element (REE) and trace element spider diagrams (Figures 5-10 and 5-11). All granitics have high rubidium, thorium, and potassium and low europium, barium, niobium, strontium, phosphorus, zirconium and titanium. The granitic samples have high light REE and negative europium anomalies due to the fractional crystallization of plagioclase under reducing conditions (e.g., Rollinson, 1993). The Egrigoz and Koyunoba plutons have flat REE patterns relative to the Alacam pluton [$(La/Lu)_N$= 11.2±3.9, 11.2±2.3 compared to 15.8±8.1]. Flatter REE patterns may be caused by higher degrees of metamorphism (e.g. Bea and Montero, 1999). Because zircon concentrates into heavy REE over light REE, zircon fractionation can enrich light REE and deplete zirconium. Low strontium indicates plagioclase fractionation and low barium is consistent with the crystallization of alkali feldspar. Phosphorus is depleted due to the crystallization of apatite and the crystallization of titanite is responsible for the depletion of titanium.

5.3 Discussion

Geochemical analyses have been used to interpret the origin the Egrigoz, Koyunoba, and Alacam plutons. In general, these plutons are peraluminous S-type granite to granodiorites (Figure 5-1) and show evidence of fractional crystallization. The rocks are calcic-alkalic to alkali-calcic, which may be due to magma mixing (Frost et al., 2001), and range from magnesian to ferroan with increasing SiO_2 (Figure 5-6). Magnesian granites are typical of subduction zones whereas ferroan granites are typical of extensional environments (Frost and Lindsley, 1991; Frost et al., 2001). Trace element data show the plutons emplaced in a volcanic arc setting, consistent with the north-dipping subduction of the African plate beneath the Eurasian plate.

A key question is if the three plutons in the field area share the same source and tectonic history. Previous researchers have noted the existence of a detachment separating the Alacam pluton from the Koyunoba and Egrigoz plutons (see Chapter 4, Isik and Tekeli, 2001; Isik et al., 2004; Seyitoglu et al., 2004; Thomson and Ring, 2006). If this detachment exists, a difference in geochemical analyses between the plutons would be expected. Major and trace element analyses show little difference between the three plutons (e.g., Figures 5-10 5-11), suggesting the plutons share a similar source and are not separated by a major structure (i.e. the Simav detachment).

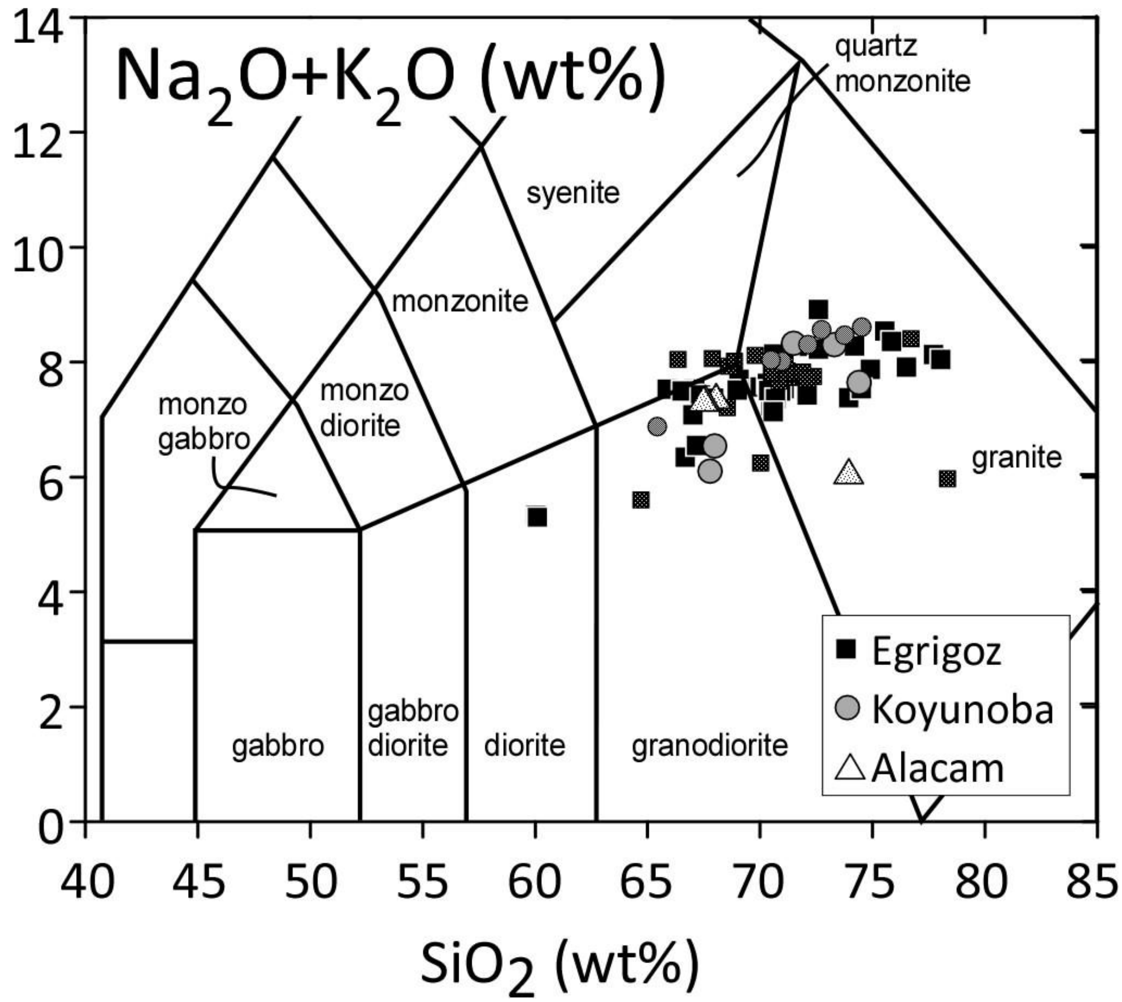

Figure 5-1: Na_2O+K_2O versus SiO_2 diagram for the Egrigoz, Koyunoba, and Alacam plutons (Middlemost, 1994). The plutons range from diorite, granodiorite and, quartz monzonite, to granite. Data from: Ozgenc and Ilbeyli, 2008, n=12; Akay, 2009, n=20; Erkul et al., 2010, n=11; this thesis, n=31 (indicated with hatch marks)

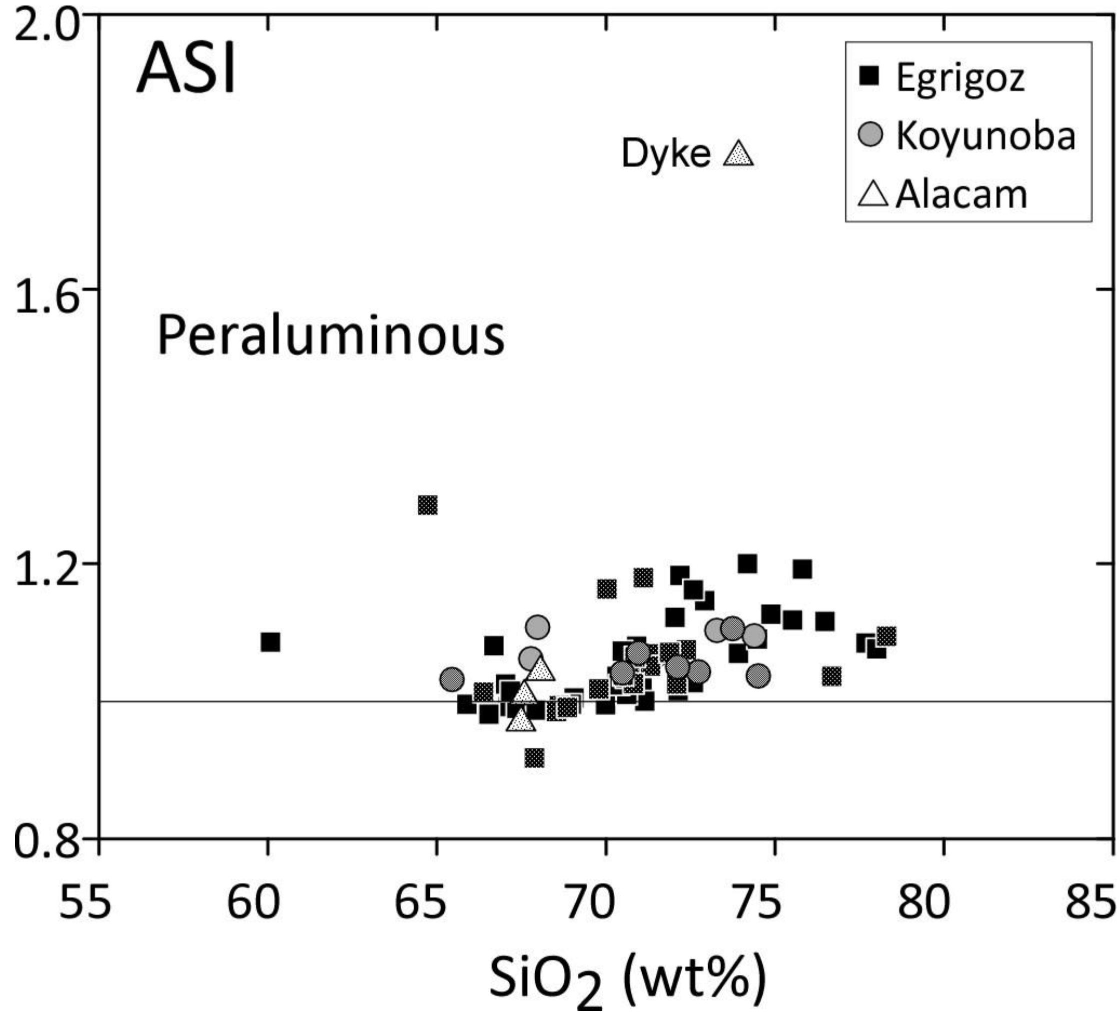

Figure 5-2: Aluminum-saturation index (ASI; Al/Ca-1.67P+Na+K) (molar) vs. SiO_2 wt. % diagram (after Frost et al., 2001). Data points are the same as in Figure 5-1. Most samples are peraluminous.

.

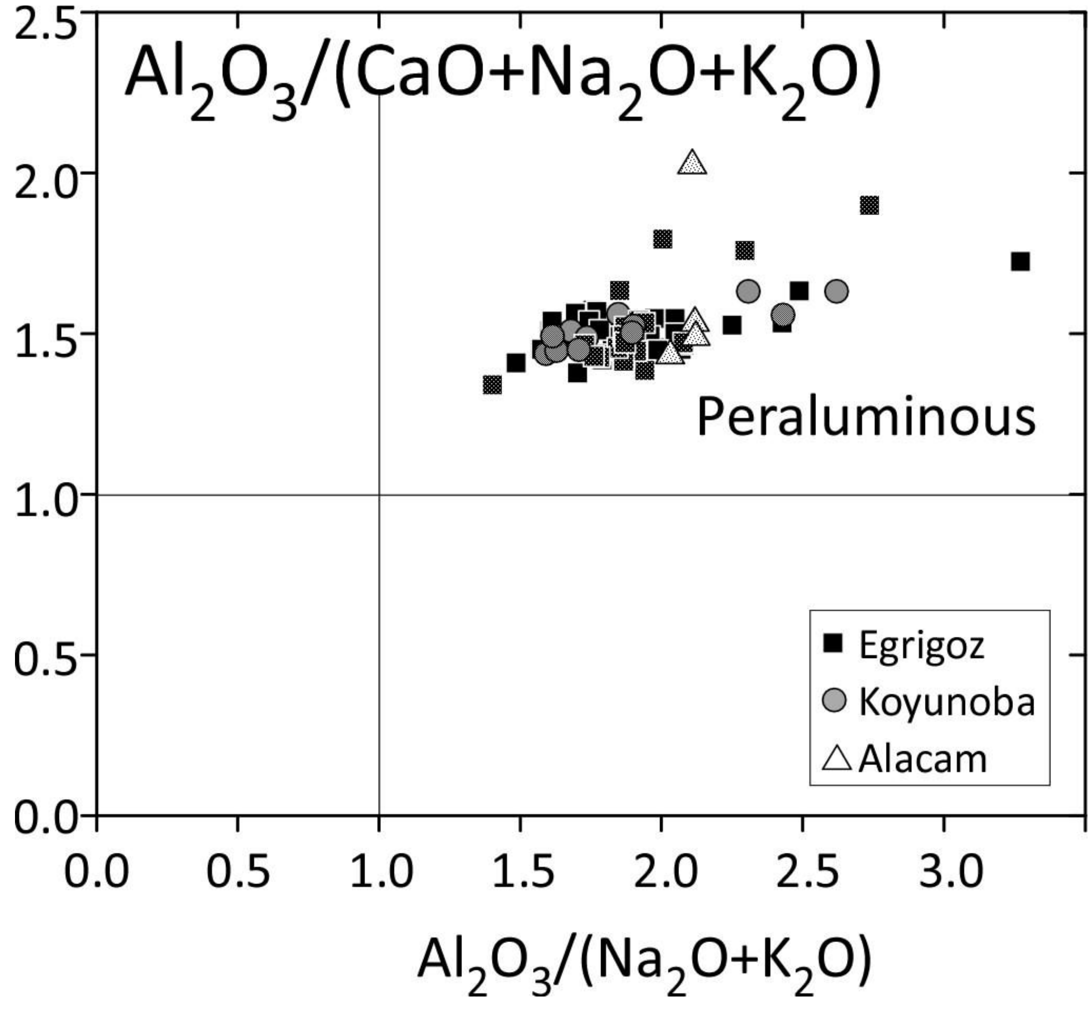

Figure 5-3: Shand's index for granitic protolith (after Maniar and Piccoli, 1989). Data points are the same as in Figure 5-1. Samples plot within the peraluminous field.

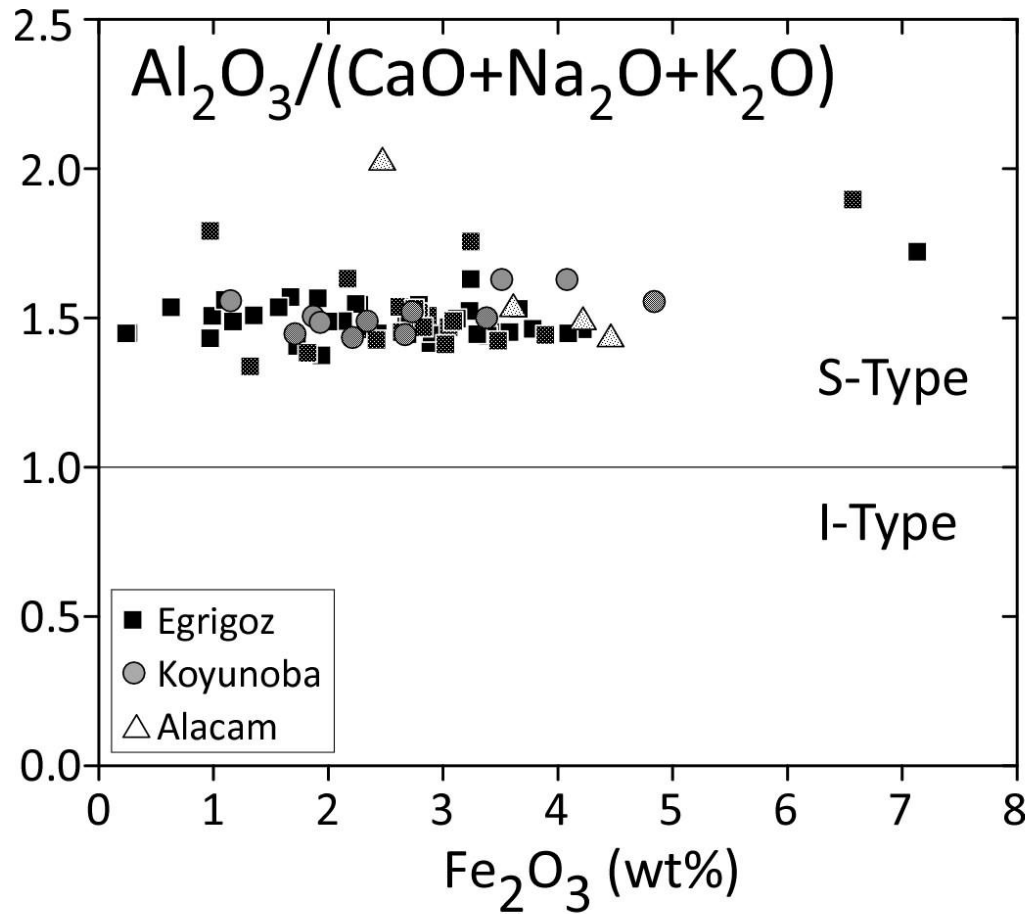

Figure 5-4: $Al_2O_3/(CaO+Na_2O+K_2O)$ vs. wt. Fe_2O_3 wt %. All granitics plot within the S-type field. Data points are the same as in Figure 5-1.

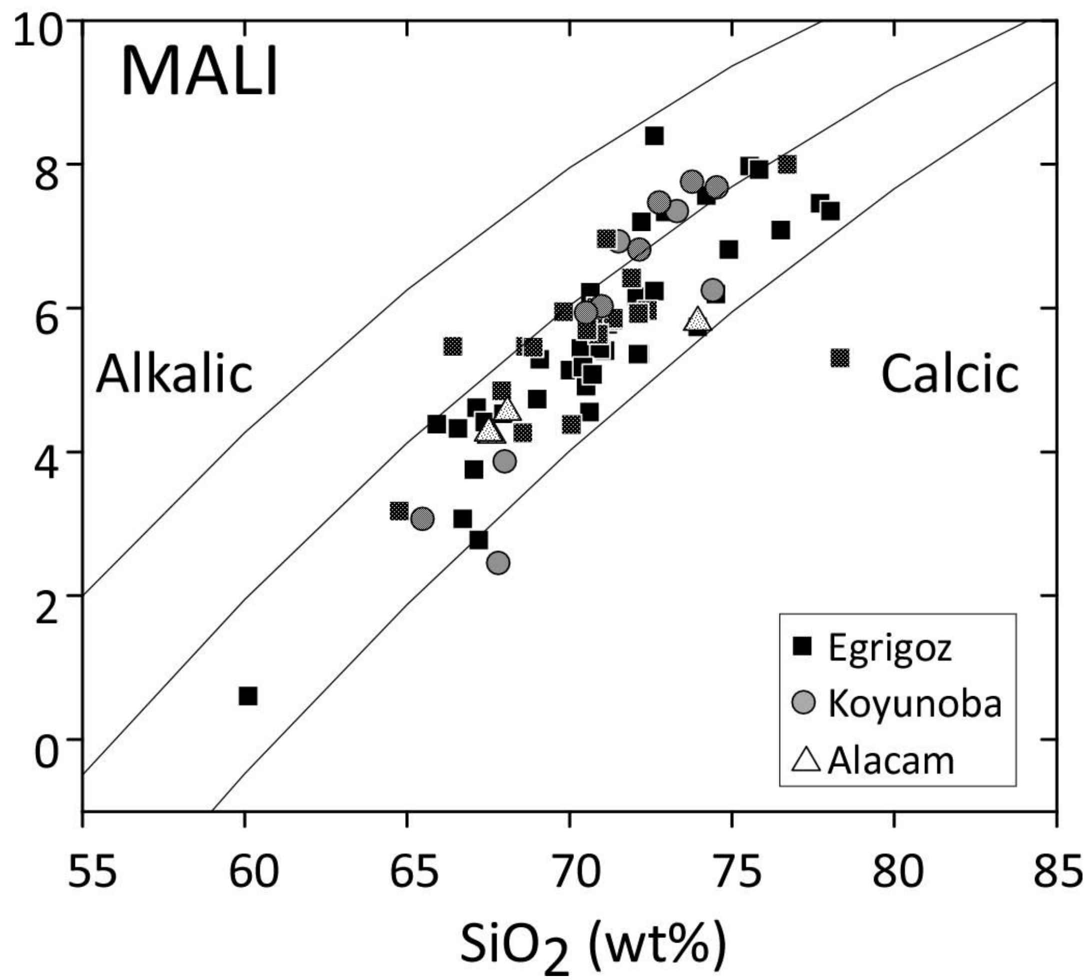

Figure 5-5: Modified Alkaline Lime Index (MALI; Na_2O+K_2O-CaO) vs. SiO_2 wt. % after Le Maitre et al (1989). Data points are the same as in Figure 5-1.

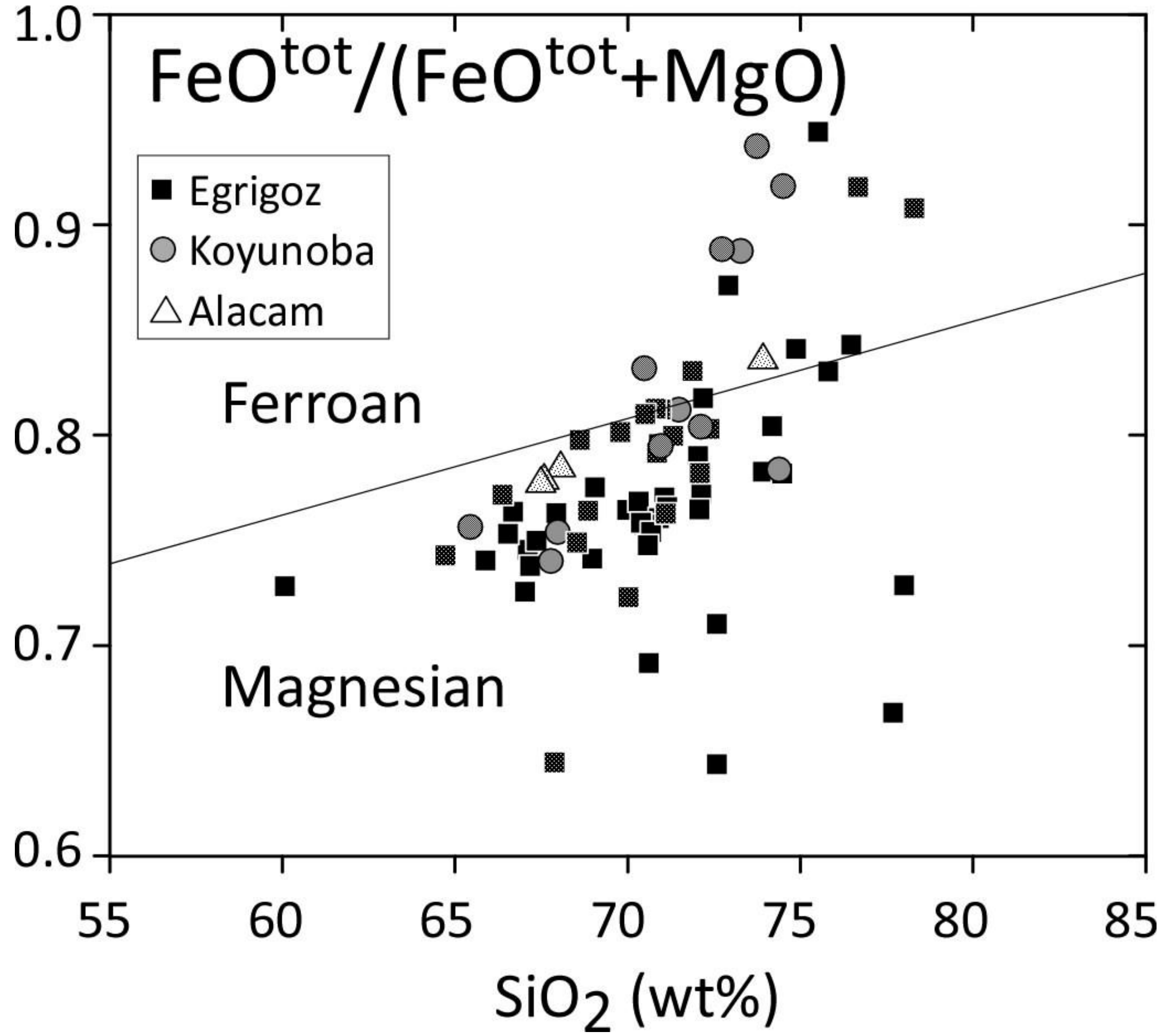

Figure 5-6: $FeO^{tot}/(FeO^{tot}+MgO)$ vs. SiO_2 wt. % diagram (after Frost et al., 2001). Data points are the same as in Figure 5-1. Koyunoba and Alacam samples become more ferroan with increasing SiO_2.

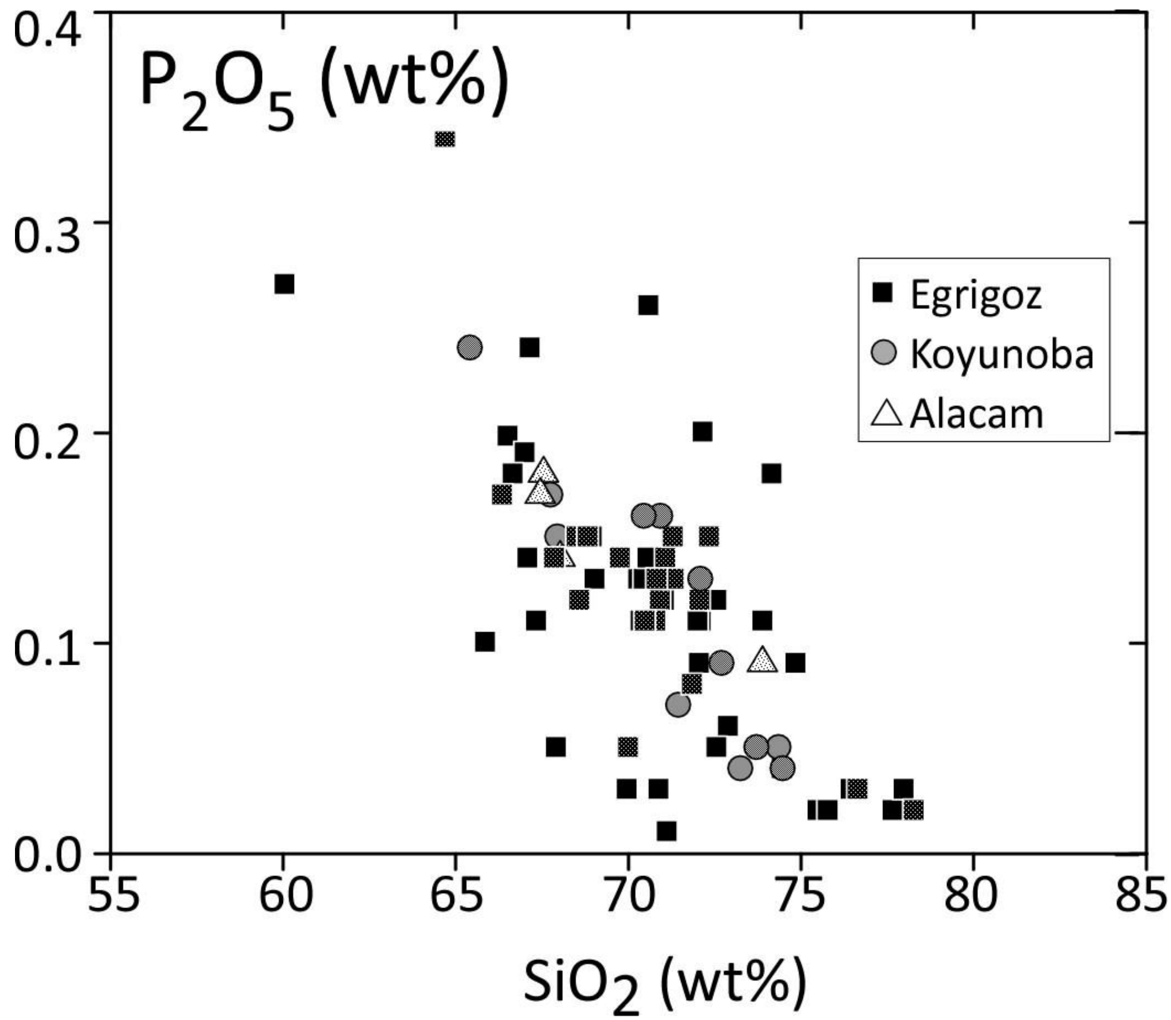

Figure 5-7: P_2O_5 vs. SiO_2 wt. % diagram for the plutons analyzed in this study showing fractional crystallization. Data points are the same as in Figure 5-1.

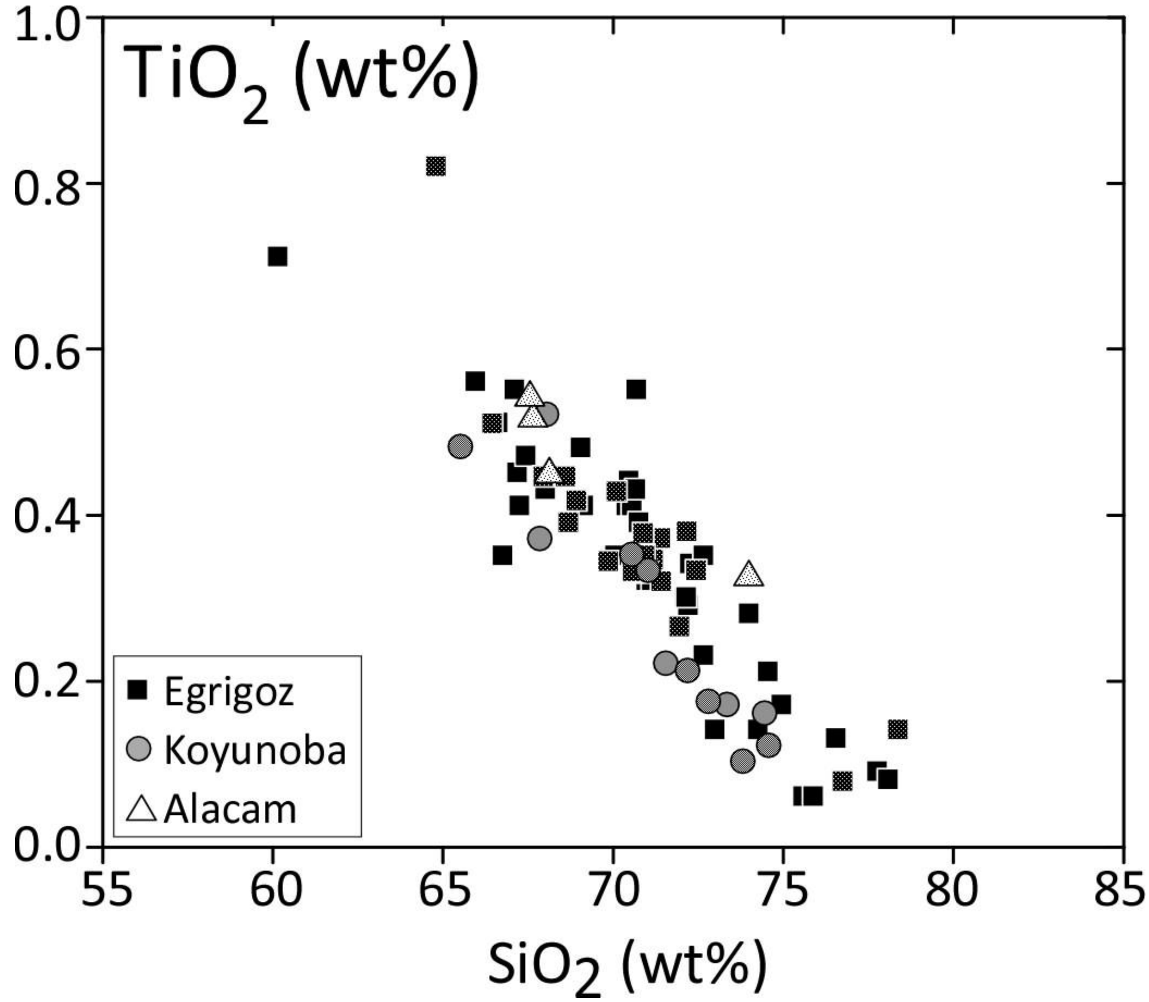

Figure 5-8: Major element Harker diagram (TiO_2vs. SiO_2 wt. %) showing fractional crystallization. Data points are the same as in Figure 5-1.

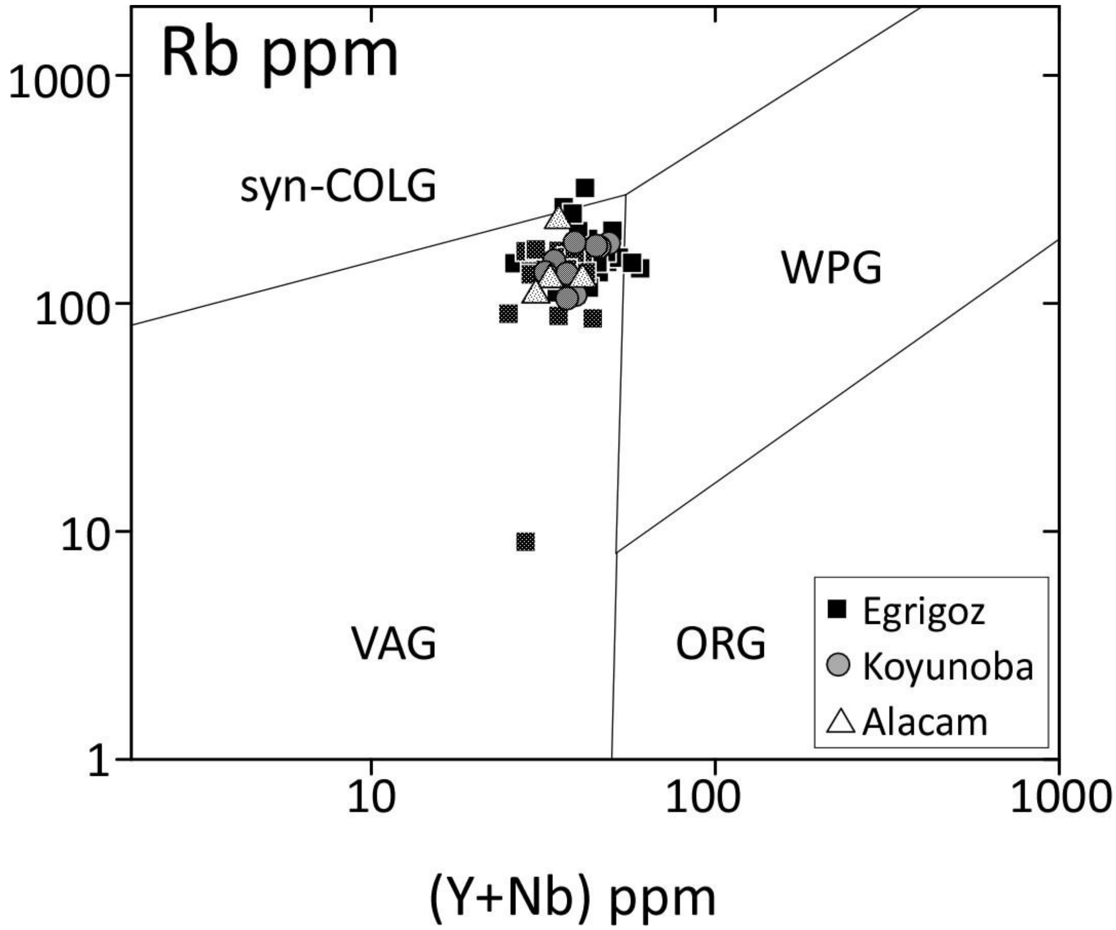

Figure 5-9: Rb vs. (Y+Nb) discrimination diagram for granitics showing the syn-collisional granites (syn-COLG), within-plate granites (WPG), volcanic-arc granites (VAG), and ocean ridge granites (ORG) (Pearce et al., 1984). Data points are the same as in Figure 5-1.

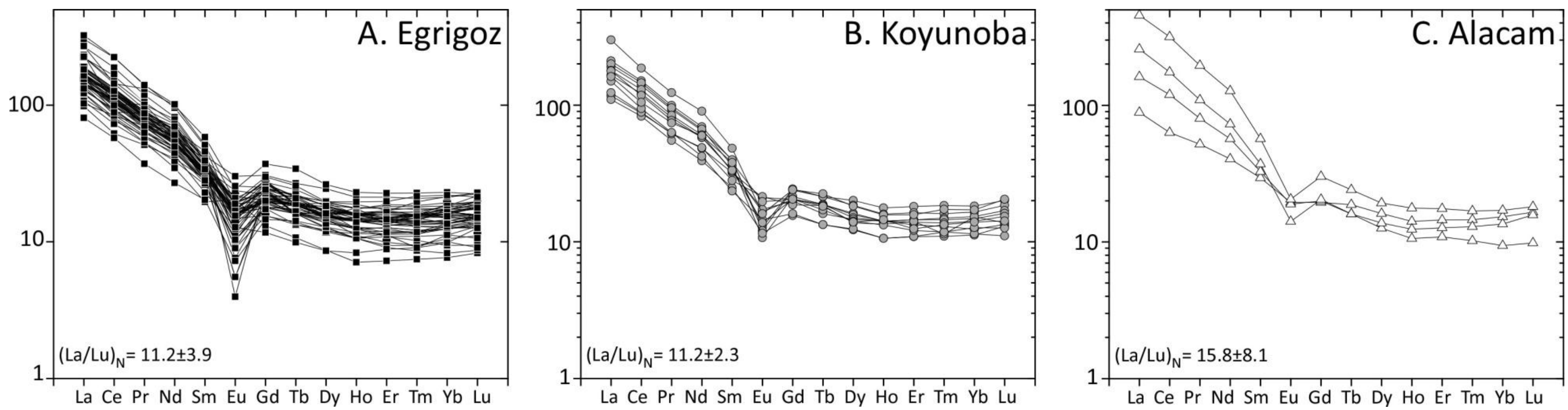

Figure 5-10: Chondrite-normalized (Sun and McDonough, 1989) rare earth element (REE) patterns for the Egrigoz (A), Koyunoba (B), and Alacam (C) granitoids. Data is the same as in Figure 5-1.

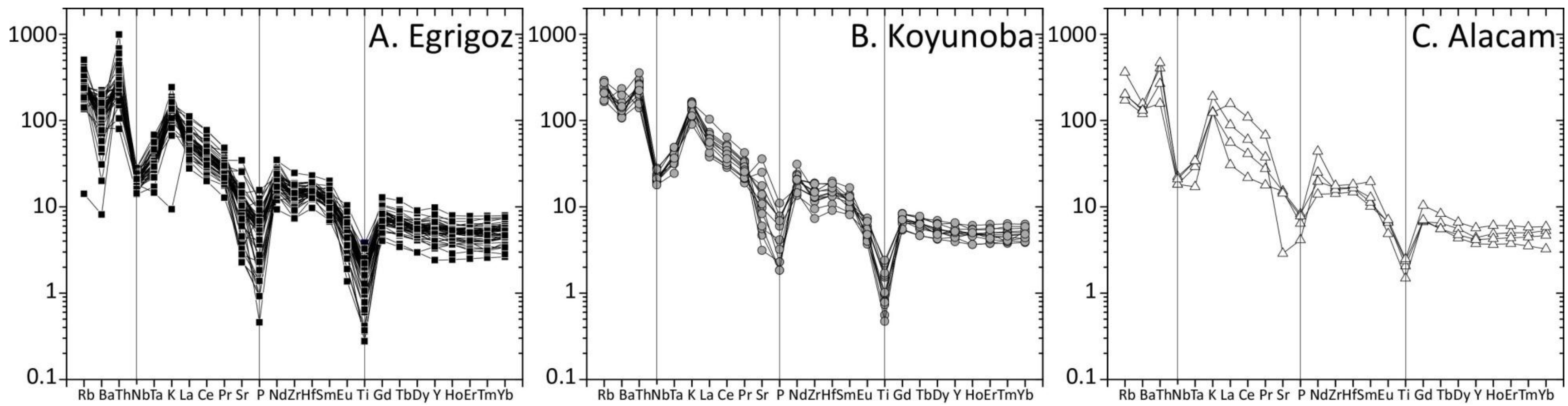

Figure 5-11: Spider diagrams normalized to primitive mantle (Sun and McDonough, 1989) for the Egrigoz (A), Koyunoba (B), and Alacam (C) granitoids. Data is the same as in Figure 5-1.

Table 5.1. Major element concentrations from the Egrigoz pluton.

	AT02A	AT02B	AT03	AT04A	AT04B	AT05A	AT05B	AT06	AT07A	AT08	AT15A	AT15B	AT15C	AT16
SiO_2	57.1	71.1	67.9	68.6	66.4	68.6	68.9	71.0	69.8	71.4	72.4	71.3	70.9	70.8
Al_2O_3	14.3	14.8	15.5	14.7	15.2	14.9	14.8	14.9	14.8	14.7	14.4	14.4	14.8	14.1
Fe_2O_3	6.07	2.17	1.82	3.48	3.89	3.05	3.02	2.87	2.64	2.62	2.79	3.09	2.75	3.48
MnO	0.11	0.05	0.03	0.04	0.03	0.03	0.02	0.04	0.03	0.03	0.05	0.05	0.05	0.05
MgO	4.58	0.68	1.01	0.89	1.16	1.03	0.94	0.67	0.66	0.66	0.69	0.78	0.73	0.81
CaO	5.04	1.06	3.19	2.44	2.56	2.94	2.54	2.05	2.15	1.89	1.77	1.93	2.02	1.95
Na_2O	2.78	3.72	4.53	3.44	3.40	3.78	3.34	3.75	3.71	3.82	3.53	3.52	3.70	3.03
K_2O	4.01	4.25	3.45	4.41	4.57	3.37	4.60	4.09	4.33	3.84	4.15	4.21	3.90	4.87
TiO_2	0.79	0.35	0.45	0.39	0.51	0.45	0.42	0.33	0.34	0.32	0.33	0.37	0.35	0.38
P_2O_5	0.39	0.14	0.14	0.12	0.17	0.15	0.15	0.12	0.14	0.13	0.15	0.15	0.13	0.11
LOI	4.27	1.90	1.12	1.00	0.80	0.92	0.93	0.72	1.07	0.94	0.71	0.82	0.78	0.74
Total	99.4	100	99.1	99.5	98.7	99.1	99.7	100	99.7	100	101	101	100	100

Elements reported as weight percent oxide. Detection limit for all elements is 0.001 wt% with the exception of MnO (0.01%) and TiO_2 (0.01%), Fe_2O_3 is measured total. All elements were obtained using Fusion Inductively Coupled Plasma Spectrometry. LOI = Loss of Ignition. See Figure 2-4 and Table 3-1 for sample locations.

Table 5.2. Major element concentrations from the Koyunoba pluton.

	AT09	AT10	AT11	AT12	AT13	AT14	AT17
SiO_2	74.5	72.8	73.76	65.5	71.0	70.5	72.1
Al_2O_3	13.6	13.8	13.52	16.6	15.1	15.1	14.0
Fe_2O_3	2.21	2.67	2.34	4.84	2.73	3.38	1.71
MnO	0.07	0.05	0.05	0.06	0.05	0.05	0.02
MgO	0.20	0.34	0.16	1.57	0.71	0.69	0.42
CaO	0.90	1.06	0.68	3.82	1.97	2.08	1.46
Na_2O	3.95	3.91	3.46	3.55	3.71	3.99	3.45
K_2O	4.57	4.56	4.92	3.28	4.23	3.97	4.77
TiO_2	0.12	0.17	0.10	0.48	0.33	0.35	0.21
P_2O_5	0.04	0.09	0.05	0.24	0.16	0.16	0.13
LOI	0.51	0.71	0.99	0.77	0.58	0.68	0.54
Total	101	100	100	101	101	101	98.9

Detection limits and methods same as for Table 5.1.

Table 5.3. Major element concentrations from the Alacam pluton.

	AT19	AT20A	AT20B	AT21
SiO_2	68.1	67.6	73.9	67.5
Al_2O_3	15.4	15.4	12.7	14.7
Fe_2O_3	3.61	4.22	2.47	4.46
MnO	0.07	0.08	0.07	0.07
MgO	1.00	1.21	0.49	1.29
CaO	2.78	3.07	0.25	3.02
Na_2O	3.53	3.56	0.36	3.54
K_2O	3.75	3.69	5.64	3.69
TiO_2	0.45	0.52	0.32	0.54
P_2O_5	0.14	0.18	0.09	0.17
LOI	0.67	0.69	2.86	0.55
Total	99.5	100	99.2	99.5

Detection limits and methods same as for Table 5.1.

Table 5.4. Trace element concentrations from the Egrigoz pluton.

	AT02A	AT02B	AT03	AT04A	AT04B	AT05A	AT05B	AT06	AT07A	AT08	AT15A	AT15B	AT15C	AT16
Sc	18	6	8	5	7	7	7	6	6	5	6	6	5	6
Be	3	4	3	3	3	3	3	4	4	6	3	4	3	3
V	133	27	51	39	53	44	43	23	25	24	25	26	25	40
Ba	1568	794	1249	1566	1318	658	1195	758	948	733	971	935	899	781
Sr	463	176	304	269	271	276	264	210	229	210	210	219	236	210
Y	28	26	22	23	21	22	18	25	27	26	22	22	18	16
Zr	169	165	169	170	193	172	141	157	163	160	159	167	166	148
Cr	230	nd	nd	nd	nd	nd	nd	nd	nd	nd	nd	nd	nd	nd
Co	19	2	1	3	3	3	2	2	2	2	2	3	2	3
Ni	70	nd	nd	nd	nd	nd	nd	nd	nd	nd	nd	nd	nd	nd
Cu	20	nd	nd	nd	nd	nd	nd	nd	nd	10	nd	nd	10	nd
Zn	60	nd	nd	nd	nd	nd	nd	nd	30	30	40	50	60	50
Ga	16	17	17	16	17	17	16	17	17	17	17	16	17	15
Ge	2	2	2	2	2	2	2	2	2	2	2	2	2	2
Rb	147	142	88	152	150	128	138	163	156	137	170	159	143	169
Nb	14	14	13	14	14	13	12	14	14	16	13	15	11	12
Mo	nd	nd	nd	nd	nd	nd	4	3	nd	nd	3	nd	nd	nd
Ag	0.5	0.5	0.6	0.5	0.6	0.6	nd	0.5	0.5	nd	0.5	nd	0.5	nd
Sn	3	6	9	4	5	5	6	5	6	5	5	5	5	3
Sb	3.8	nd	nd	nd	nd	nd	nd	nd	nd	nd	nd	nd	nd	nd
Cs	1.4	2.1	1.5	4.9	4.8	4.8	3.7	10.3	5.3	4.7	6.5	11.5	7.9	5.9
La	45.1	72.1	63.6	34.3	53	33.9	33.4	38.8	38.1	30.3	33.9	34.6	36.4	44.6
Ce	91.7	136	115	66.2	100	65.2	63.2	75.5	73.1	56.9	64.7	66.6	69.1	81
Pr	10.2	13.4	11.3	6.94	10	6.84	6.57	7.84	7.59	6.18	6.77	7.06	7.14	7.86
Nd	38.6	44.7	38	24.4	34.6	24.4	22.7	27.7	26.6	22.5	24	24.9	24.8	26
Sm	7.2	7.6	6.2	4.7	6	4.6	4.4	5.4	5.2	4.8	4.8	4.9	4.7	4.3
Eu	1.65	0.87	1.14	1	1.12	0.99	1.04	0.85	0.9	0.86	0.9	0.9	0.95	0.86

Gd	6.1	5.6	4.6	4	4.9	4	3.7	4.4	4.5	4.3	4.1	4.2	4	3.2
Tb	0.9	0.9	0.7	0.7	0.7	0.6	0.6	0.7	0.8	0.7	0.7	0.7	0.6	0.5
Dy	5	4.9	4	3.9	3.9	3.7	3.5	4.3	4.7	4.3	3.8	4	3.6	3
Ho	1	1	0.8	0.8	0.8	0.8	0.7	0.9	1	0.9	0.8	0.8	0.7	0.6
Er	2.8	2.9	2.4	2.4	2.2	2.3	2.1	2.6	3	2.6	2.2	2.3	2.1	1.8
Tm	0.42	0.44	0.36	0.38	0.33	0.35	0.31	0.4	0.46	0.4	0.34	0.36	0.31	0.28
Yb	2.7	2.9	2.4	2.7	2.2	2.3	2.1	2.7	3.1	2.8	2.3	2.4	2.1	1.9
Lu	0.43	0.48	0.39	0.46	0.35	0.37	0.34	0.45	0.5	0.46	0.39	0.4	0.34	0.33
Hf	4.6	4.7	4.8	4.9	5.4	5	4.1	4.5	4.9	4.8	4.5	4.7	4.6	4.2
Ta	0.9	1.5	1	1.5	0.9	1.1	1	1.6	1.5	2.2	1.2	1.3	1.1	1.2
W	2	nd	nd	nd	nd	nd	nd	nd	nd	nd	2	1	nd	nd
Tl	1.3	0.8	0.4	0.7	0.8	0.6	0.7	0.8	0.8	0.7	0.8	0.8	0.7	0.8
Pb	27	23	22	42	28	22	28	31	35	31	34	29	41	34
Th	20	26.7	29.6	18.9	22.1	19.5	18.1	23.3	20.1	25.5	18.8	18.5	18.2	84.3
U	5.3	6.4	6.2	7.4	4.4	6.7	5.1	8	10.1	8.3	7.6	6.3	6.2	13.8

All elements reported as parts per million (ppm). The elements Sc, Be, V, Ba, Sr, Y, Zr were obtained using Fusion Inductively Coupled Plasma Spectrometry. All other elements were detected using Fusion Inductively Coupled Plasma/ Mass Spectrometry. Detection limits: Lu = 0.04 ppm; Pr, Eu, Tm = 0.05 ppm; La, Ce, Nd, Gd, Tb, Dy, Ho, Er, Yb, Ta, Tl, Th, U = 0.1 ppm; In and Hf = 0.2 ppm: Bi = 0.4 ppm; Sc, Be, Co, Ga, Ge, Nb, Sn, W = 1ppm; Sr, Y, Rb, Mo = 2 ppm; Ba = 3 ppm; Zr = 4 ppm; V, As, Pb = 5 ppm; Cu = 10 ppm; Cr and Ni = 20 ppm. Zn = 30. Bi, As, and In were measured but not detected (nd).

Table 5.5. Trace element concentrations from the Koyunoba pluton.

	AT09	AT10	AT11	AT12	AT13	AT14	AT17
Sc	4	4	4	8	5	5	4
Be	5	5	4	4	3	4	3
V	nd	9	nd	65	23	22	15
Ba	748	796	788	1637	974	1130	795
Sr	99	118	66	758	279	294	205
Y	29	25	23	23	20	21	18
Zr	134	142	129	144	171	211	106
Co	nd	1	nd	5	3	2	1
Cu	10	nd	10	10	nd	nd	nd
Zn	40	40	50	50	nd	50	nd
Ga	17	17	16	18	17	17	15
Ge	2	2	2	2	2	2	2
Rb	177	179	185	105	154	135	137
Nb	17	20	16	14	14	16	14
Mo	nd	nd	nd	nd	nd	nd	3
Ag	nd	nd	nd	nd	0.5	0.6	nd
Sn	5	4	6	7	4	4	3
Cs	9	6.5	5.5	7.3	4.7	5.9	3.5
La	49.9	45.2	47.5	27.8	39.2	42.4	26
Ce	92.3	85.4	89.1	53.4	74.1	79.4	50.7
Pr	9.45	8.85	9.07	5.93	7.71	8.01	5.24
Nd	32.4	30.4	31.2	22.5	27	28.2	18.3
Sm	6	6.1	5.5	4.9	5.1	5	3.8
Eu	0.74	0.7	0.62	1.22	0.96	1	0.67
Gd	5	4.9	4.4	4.2	4.2	4.1	3.2
Tb	0.8	0.8	0.7	0.7	0.7	0.6	0.5
Dy	5.1	4.7	4.1	4	3.8	3.7	3.1
Ho	1	0.9	0.8	0.8	0.8	0.8	0.6
Er	3	2.7	2.4	2.4	2.2	2.3	1.8
Tm	0.47	0.41	0.38	0.37	0.33	0.35	0.28
Yb	3.1	2.8	2.6	2.5	2.1	2.4	1.9
Lu	0.51	0.47	0.43	0.41	0.34	0.39	0.33
Hf	4.2	4.5	4.2	4.1	4.8	5.6	3.3
Ta	2	1.9	1.5	1.4	1.3	1.3	1.7
W	2	nd	2	nd	nd	nd	nd
Tl	0.9	0.7	0.9	0.6	0.8	0.7	0.6
Pb	40	41	50	34	43	47	54
Th	24.3	25.4	22.7	11.9	20.1	21.2	16.2
U	7.3	4.9	3.6	6.1	5	2.5	7

Methods and detection limits are the same as Table 5.4. Bi, Cr, As, Sb, and In were measured but not detected (nd).

Table 5.6. Trace element concentrations from the Alacam pluton.

	AT19	AT20A	AT20B	AT21
Sc	7	9	5	9
Be	3	3	2	3
V	55	55	25	66
Ba	943	837	1095	919
Sr	320	320	61	303
Y	20	17	19	26
Zr	159	186	177	198
Co	4	5	2	6
Zn	60	90	80	50
Ga	17	17	14	18
Ge	2	2	2	2
As	nd	nd	15	nd
Rb	127	109	231	128
Nb	13	13	16	15
Mo	nd	nd	9	nd
Ag	nd	0.5	0.6	0.6
Sn	4	2	3	4
Sb	nd	nd	5.5	nd
Cs	8	5.3	20	10.2
La	21	38.3	61	108
Ce	38.6	73.3	107	194
Pr	4.93	7.62	10.4	18.6
Nd	18.9	26.6	34	59.5
Sm	4.5	5	5.7	8.7
Eu	1.13	1.1	0.82	1.19
Gd	4	4.1	4.2	6.2
Tb	0.7	0.6	0.6	0.9
Dy	4.1	3.2	3.5	4.9
Ho	0.8	0.6	0.7	1
Er	2.4	1.8	2.1	2.9
Tm	0.37	0.26	0.33	0.43
Yb	2.6	1.6	2.3	2.9
Lu	0.42	0.25	0.4	0.46
Hf	4.6	5.1	5.1	5.6
Ta	1.2	0.7	1.4	1.4
W	1	nd	3	nd
Tl	0.8	0.7	2.2	0.7
Pb	28	26	23	24
Th	13.4	22.8	34.3	39.7
U	6.1	4.1	9.8	6

Methods and detection limits are the same as Table 5.4. Bi, Cr, Ni, Cu, and In were measured but not detected (nd).

Chapter 6: Cathodoluminescence Imagery and Discussion

6.1 Introduction

In this study, cathodoluminescence (CL) is used to understand the structural history of the Egrigoz, Koyunoba, and Alacam plutons by identifying mineral distribution and compositions, cracks and vein textures, mineral zoning, and potential fluid alteration (e.g., Ramseyer et al., 1992; Cox et al., 1996; Stirling et al., 1999; Goetze et al., 2000; Sorensen et al., 2006). CL is also used to better understand ion microprobe zircon ages (see Chapter 7) by identifying the textural relationships of the zircons within the samples. CL colors (wavelengths) and intensities depend upon imperfections in the host lattice and the presence of activators and quenchers (e.g., Kopp, 1981). Activators, such as manganese (Mn^{2+}) in calcite and titanium (Ti^{4+}) in alkali feldspar, are elements incorporated into the crystal structure that produce visible light when struck by an electron beam. Quenchers, such as ferrous iron (Fe^{2+}), modify the energy level arrangement so little or no visible light is produced (Marshall, 1988). Because CL is affected by subtle differences in the amounts of impurities and crystal defects, it is possible for two samples of the same mineral to behave differently (Marshall, 1977; Kopp, 1981; Sorensen et al., 2006). For example, zoned plagioclase records magmatic and subsolidus evolution (Cox et al., 1996; Stirling et al., 1999; Goetze et al., 2000; Janousek et al., 2001; Leichmann et al., 2003).

Each mineral imaged in the Egrigoz, Koyunoba, and Alacam plutons shows a characteristic color. Qualitative terms are used to describe the colors seen with CL (e.g. Sorensen et al., 2006; Parsons et al., 2008). Plagioclase grains are shades of green and yellow due to the presence of Ca^{2+} and Mn^{2+} (e.g., Greake et al., 1972). Alkali feldspars are seen in shades of blue due to activators Eu^{2+}, Ti^{4+}, and Ga^{3+} (Geake et al., 1973; Mariano and Ring, 1975; De St. Jorre and Smith, 1990; Finch and Klein, 1999). When oxidized, alkali feldspar can turn a shade of red (from blue) due to trace amounts of Fe changing oxidation state. In igneous rocks, quartz only weakly luminesces (activators unknown) and is seen as brown or dull black. Subtle variations of colors in feldspars and quartz are typically attributed to different amounts of activators and quenchers and may distinguish different generations of crystallization (Marshall, 1988). Bright yellow apatite and bright white zircon grains are also visible in CL. Calcite, a secondary mineral acquired during fluid alteration, can be seen as bright orange and is typically located along cracks, grain boundaries, and within cracked plagioclase cores. Biotite, muscovite, hornblende, rutile, and monazite are not visible in CL.

6.2. CL INTERPRETATIONS

6.2.1 Egrigoz pluton

Samples WA12B, AT05A, and AT16 were collected from the Egrigoz pluton and contain Qtz + Pl + Kfs + Bt + Ms + Chl + Ap + Cal + Rt + Zrn + FeO (Table 3-2) (mineral abbreviations after Kretz, 1983). Sample WA12B, collected from the southern portion of the Egrigoz pluton (see Figure 2-4), contains plagioclase of at least two distinct grain sizes (~1mm, ~3mm) suggesting magma mixing (e.g., Salisbury et al., 2008). Large (~3mm) retrogressed plagioclase grains are surrounded by alkali feldspar, quartz, and biotite. Plagioclase grains have brighter green cores and darker green rims. Higher amounts of calcium are responsible for bright yellow-green CL in plagioclase (Catlos et al., 2011). Corroded cores in all plagioclase may be relic crystals from previous magmas (Janousek et al., 2004). Red-rimmed feldspars and crack boundaries are indicative of post-crystallization oxidation from fluid alteration (Finch and Klein, 1999). Multiple generations of microcracks document episodes of deformation. Large intergranular cracks crosscut plagioclase, alkali feldspar, and quartz and are overprinted by plagioclase intragranular cleavage cracks. The cleavage cracks propagate towards the corroded cores. These cracks may have acted as conduits allowing fluids to infiltrate the cores and replace plagioclase with muscovite by metasomatism (Kretz et al., 1989). Microcracks propagate through quartz and feldspars and were likely formed during post-crystallization deformation. Grain-boundary migration and recrystallization can be seen along the plagioclase and alkali feldspar grains. Grains are texturally resorbed as alkali-feldspar intrudes brownish-green plagioclase. "Flame-type" structures within alkali feldspar grains may be due to different chemical compositions within each grain or edge effects due to microcracks (Catlos et al., 2011). Accessory minerals, specifically apatite and zircon, are found primarily clustered within biotite grains.

Sample AT16 (Figure 6-2) was collected approximately 15 kilometers from sample WA12B but shows largely similar textures. This rock was collected from the middle of the Egrigoz pluton (see Figure 2-4) and contains an abundance of accessory minerals, specifically apatite and zircon. Apatite and zircon are concentrated within biotite grains. Plagioclase grains of different sizes show a range of zoning types including normal zoning, with high-Ca cores and lower-Ca rims, patchy zoning, and weakly oscillatory zoning with darker cores, brighter mid-rims, and darker outer-rims. Corroded plagioclase cores are also present. Alkali feldspar, which is more abundant than plagioclase, exhibits "flame-type" structures and shows patchy reddish zoning. Unlike sample WA12B, sample AT16 shows calcite-filled cracks within quartz and feldspar grains. Calcite is seen within cleavage cracks of hornblende grains. Cross-cutting relationships of microcracks within quartz and feldspars document multiple episodes of deformation. Intergrowths of alkali-feldspar within plagioclase show that alkali feldspar, aided by hydrothermal fluids, is working to replace plagioclase (Drake et al., 2008; Morad et al., 2010).

Sample AT05A (Figure 6-3) was collected from the most northern part of the Egrigoz pluton (see Figure 2-4) and is significantly more altered than the other Egrigoz samples. This rock contains considerably more alkali feldspar than plagioclase. One large alkali feldspar grain envelopes quartz, biotite, and corroded plagioclase grains. Plagioclase grains appear corroded and contain swarms of microcracks. Alkali feldspar is altering and replacing plagioclase (Morad, 2010) as evidenced by brighter blue regions within the plagioclase grains. Veins within deteriorated plagioclase are filled with alkali feldspar which likely acted as conduits to facilitate a reaction between alkali feldspar and plagioclase (Morad et al., 2010). Calcite can be found in deteriorated plagioclase cores and can also be seen filling microcracks within quartz and alkali feldspar. "Flame-type" structures exist within the large alkali feldspar grain. Apatite and zircon are concentrated in small biotite grains as is typical for the Egrigoz granitic samples.

6.3.2 Koyunoba pluton CL interpretations

Samples AT10, AT12, and AT14 were collected from the Koyunoba pluton and contain Qtz+Pl+Kfs+Bt+Ap+Hbl+Ilm+Rt+Zrn+FeO+Mnz (Table 3-2). Sample AT10 (Figure 6-4) shows evidence of fluid-induced alteration. Zoning in large subhedral plagioclase grains has been overprinted by microcracks and grains appear chemically altered. Some plagioclase grains have low-Ca cores with high-Ca rims. Many have corroded cores replaced by muscovite and others have high-Ca cores with low-Ca rims. The edges of the plagioclase grains appear in reaction with matrix minerals including quartz and alkali feldspar. Two generations of quartz are seen as large (~1-3mm) fragmented grains with altered edges or small (~200μ) circular grains along grain boundaries of feldspars. The smaller quartz grains may be the result of dissolved silica within hydrothermal fluids that traveled through microcracks and precipitated along grain boundaries. Grain boundaries between quartz and alkali feldspar show evidence of fluid alteration as the alkali feldspar is being altered to a reddish hue. A reaction texture between plagioclase and alkali feldspar can be seen as brownish-green rims between the two feldspars. Apatite and zircon are concentrated near biotite grains as was seen in the Egrigoz samples.

Sample AT12 (Figure 6-5), collected 2.5 kilometers southeast of AT10, has a cumulate-like texture and shows evidence of fluid alteration and crystal settling. Similar to sample AT10, alkali feldspar is reacting with plagioclase as evidenced by myrmekite. Coarse-grained apatites, commonly associated with biotites, are evidence of crystal settling. Plagioclase grains of at least two different sizes contain multiple generations of microcracks and veins filled with alkali feldspar and quartz. Grain boundary migration between plagioclase and alkali feldspar is also documented. This rock shows ample evidence of fluid interactions as evidenced by the alteration of alkali feldspar to a reddish-brown hue along grain boundaries and microcracks.

Sample AT14 (Figure 6-6) was collected from the northern Koyunoba pluton (see Figure 2-4). The absence of red-rimmed feldspars suggests that the oxidation front did not reach the center of the pluton. CL images reveal coarse-grained granitics with subhedral plagioclase grains and large alkali feldspar and quartz grains. Myrmekite indicates alkali feldspar is replacing plagioclase. Plagioclase phenocrysts of at least two different sizes have deteriorated cores and multiple generations of microcracks. Some plagioclase grains contain cores of muscovite. Apatite and zircon are found near biotite grains as is typical of the imaged granitics.

6.3.3 Alacam pluton CL interpretations

Samples AT19, AT20A, and AT20B were collected from the Alacam pluton and contain Qtz+Pl+Kfs+Bt+Ap+Ms+Cal+Hbl+Ilm+Rt+Zrn+FeO (Table 3-2) (see Figure 2-4). Sample AT19 (Figure 6-7) shows calcite present in cores of plagioclase, veins of quartz, and cleavage cracks of hornblende. Red edges along cracks and grain boundaries within feldspars show evidence of fluid alteration. Plagioclase grains of multiple sizes have cracked and deteriorated cores filled with muscovite and calcite. Microcracks through plagioclase grains allow fluid to enter the cores. Quartz appears to be filling in grain boundaries and microcracks within alkali feldspar. Apatite and zircon grains are concentrated within biotite grains as is typical of these granitics.

Sample AT20A (Figure 6-8) shows large deteriorating plagioclase grains locally surrounded by alkali feldspar. Plagioclase grains contain larger microcracks cross-cutting smaller microcrack swarms. In some places, corrosion textures exist between the alkali feldspar and plagioclase grains. These textures are evidenced by alteration of the plagioclase to a darker olive green. Alkali feldspar grains exhibit "flame-type" structures, indicating two different compositions present. Orange calcite is seen within biotite grains. Quartz microfractures are filled with both alkali feldspar and plagioclase. Sample AT20A also contains abundant apatite and zircon.

Sample AT20B (Figure 6-9) was collected from a hydrothermally altered dacite dyke within the Alacam pluton and contains biotite and subhedral plagioclase phenocrysts in a groundmass of alkali feldspar and quartz. Plagioclase grains have a mottled texture and appear in shades of yellow to tan. The red groundmass gives evidence of oxidation. Calcite and recrystallized alkali feldspar are concentrated in vesicles within the groundmass. Accessory minerals are scarce but some zircons can be found concentrated in biotite grains and the groundmass.

6.4 SUMMARY

CL images of the Egrigoz, Koyunoba, and Alacam plutons show evidence of a complicated tectonic history that includes magma mixing, multiple stages of brittle deformation and mineral growth, and fluid alteration. Fluid interaction is evidenced in most samples by the alteration of CL colors along grain boundaries and microcracks, patchy zoning within feldspars, chemical alteration of plagioclase grains, and the presence of myrmekite, calcite, and muscovite. Different grain sizes and zoning patterns of plagioclase (Salisbury et al., 2008), corroded relic cores (Janousek et al., 2004), and "flame-type" structures within alkali feldspar (Catlos et al., 2011) are evidence of magma mixing. Multiple episodes of brittle deformation are documented by cross-cutting relationships of microcracks including large intergranular microcracks, intragranular swarms of microcracks, and cleavage microcracks. Accessory minerals, specifically zircon and apatite, are typically located within biotite grains. Geochemistry analyses indicate plutons were emplaced in a post-collisional volcanic arc setting and experienced typical fractional crystallization, but geochemistry alone cannot be used to document the complicated tectonic history of the plutons. These CL images were also used to interpret the geochronologic data described in Chapter 7 of this thesis.

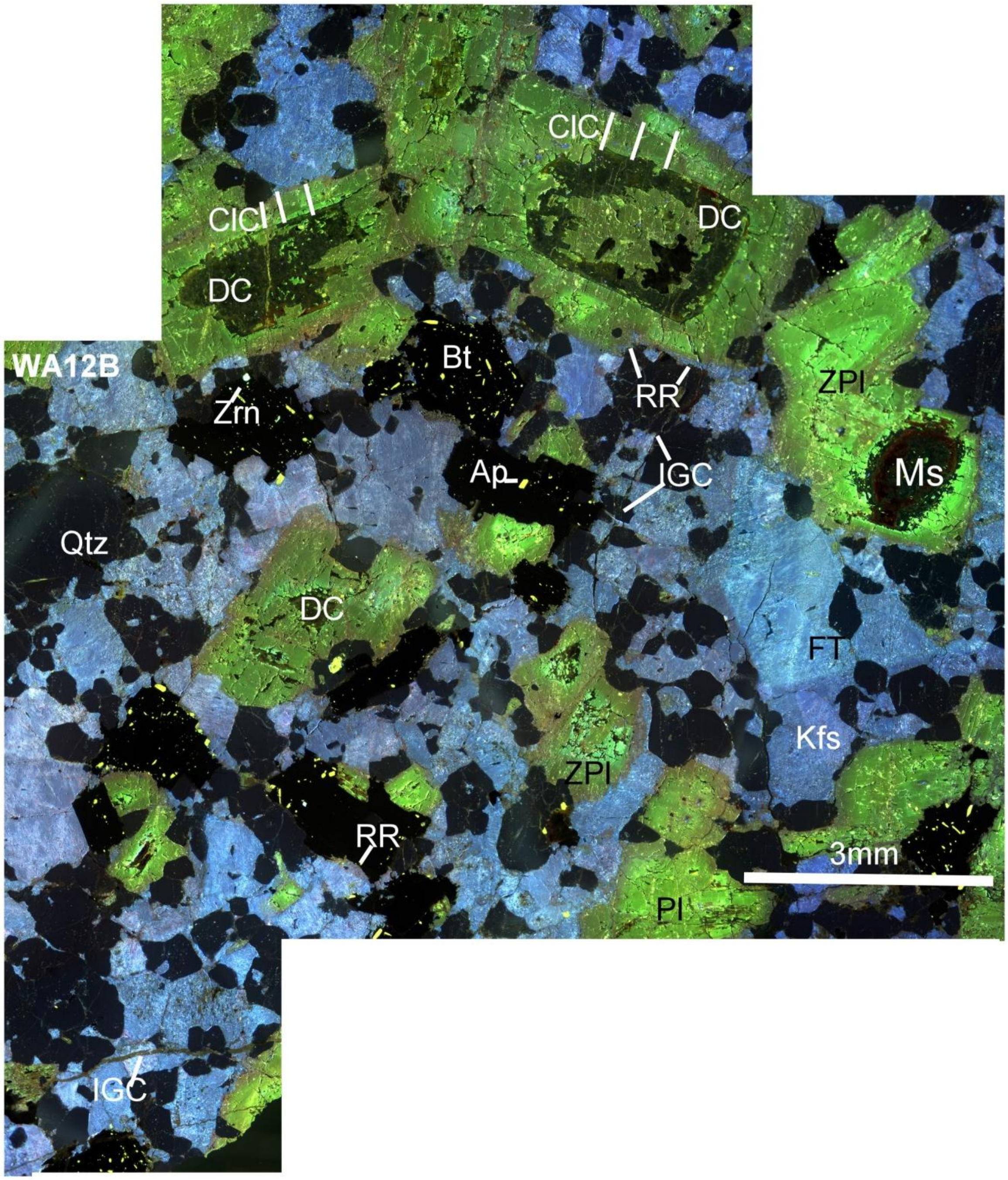

Figure 6-1: CL image of Egrigoz granitic sample WA12B. Pl=plagioclase, Qtz= quartz, Kfs=alkali feldspar, Bt= biotite, Ms=muscovite, Ap=apatite, Zrn=zircon, ZPl=zoned plagioclase, DC= deteriorated cores, RR= red rims, IGC= intergranular cracks, ClC=cleavage cracks, FT=flame textures. Abbreviations after Kretz (1983).

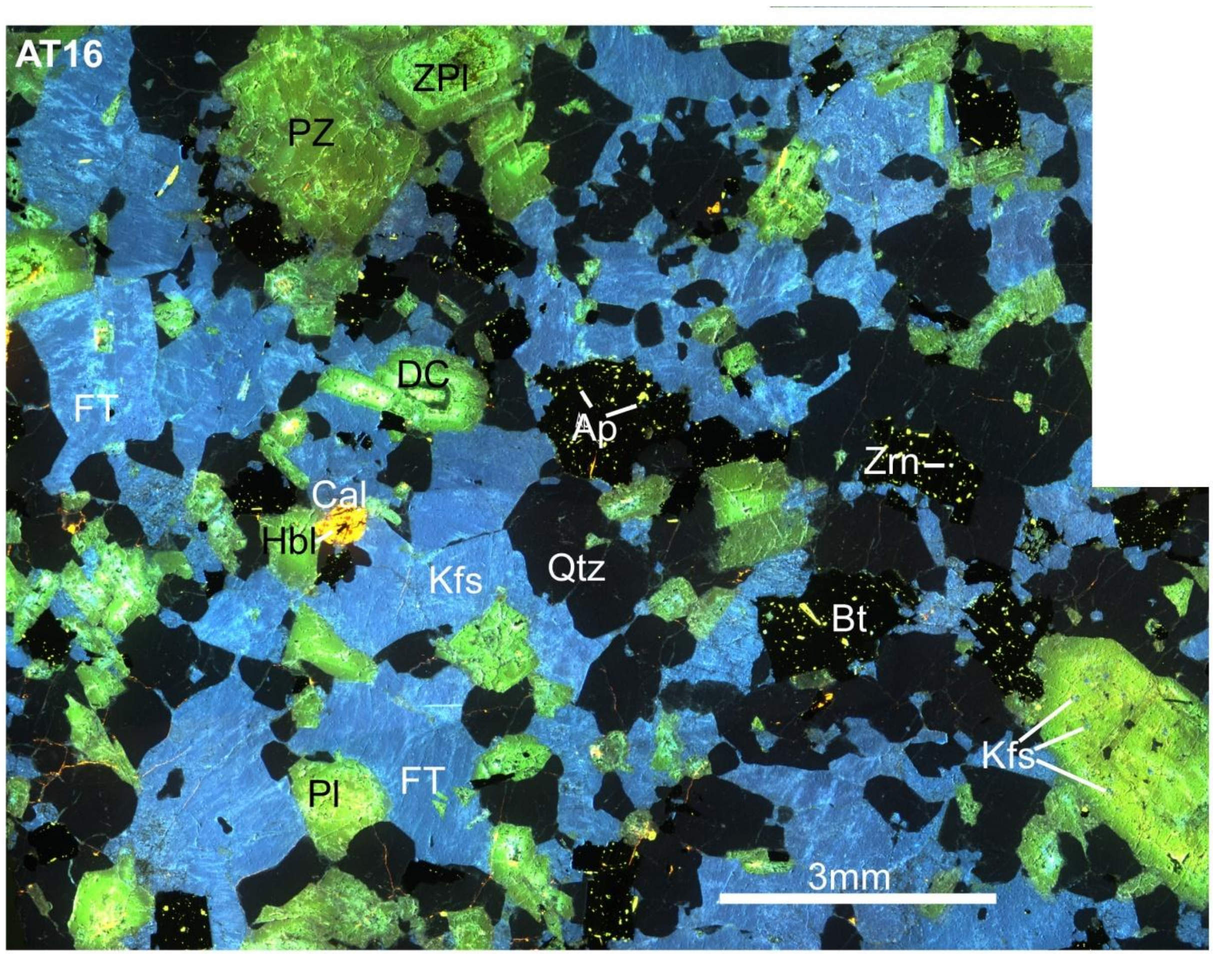

Figure 6-2: CL image of Egrigoz granitic sample AT16. Pl=plagioclase, Qtz= quartz, Kfs=alkali feldspar, Bt= biotite, Cal=calcite, Hbl=hornblende, Ap=apatite, Zrn=zircon, ZPl=zoned plagioclase, PZ=patchy zoning, DC= deteriorated cores, FT=flame textures. Abbreviations after Kretz (1983).

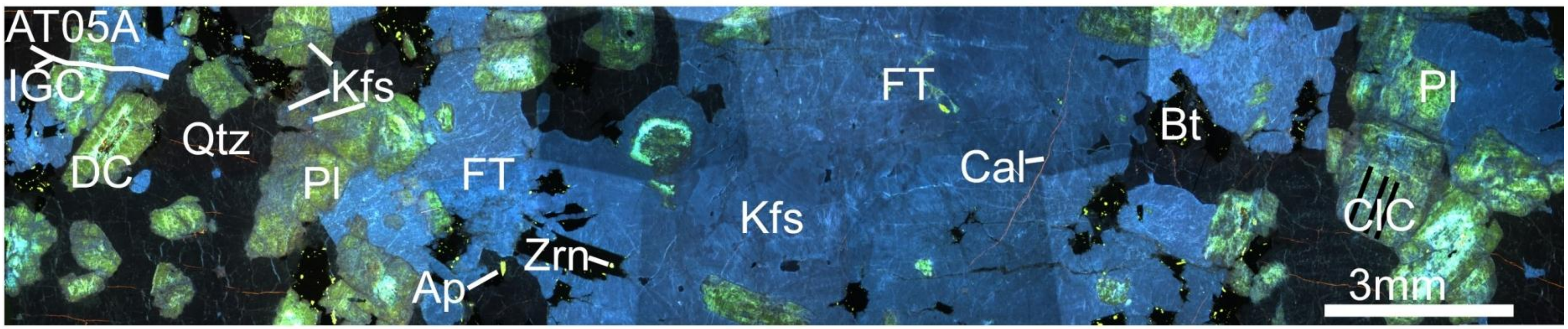

Figure 6-3: CL image of Egrigoz granitic sample AT05A. Pl=plagioclase, Qtz= quartz, Kfs=alkali feldspar, Pl=plagioclase, Bt= biotite, Cal=calcite, Ap=apatite, Zrn=zircon, DC= deteriorated cores, FT=flame textures, IGC=intergranular cracks, ClC=cleavage cracks. Abbreviations after Kretz (1983).

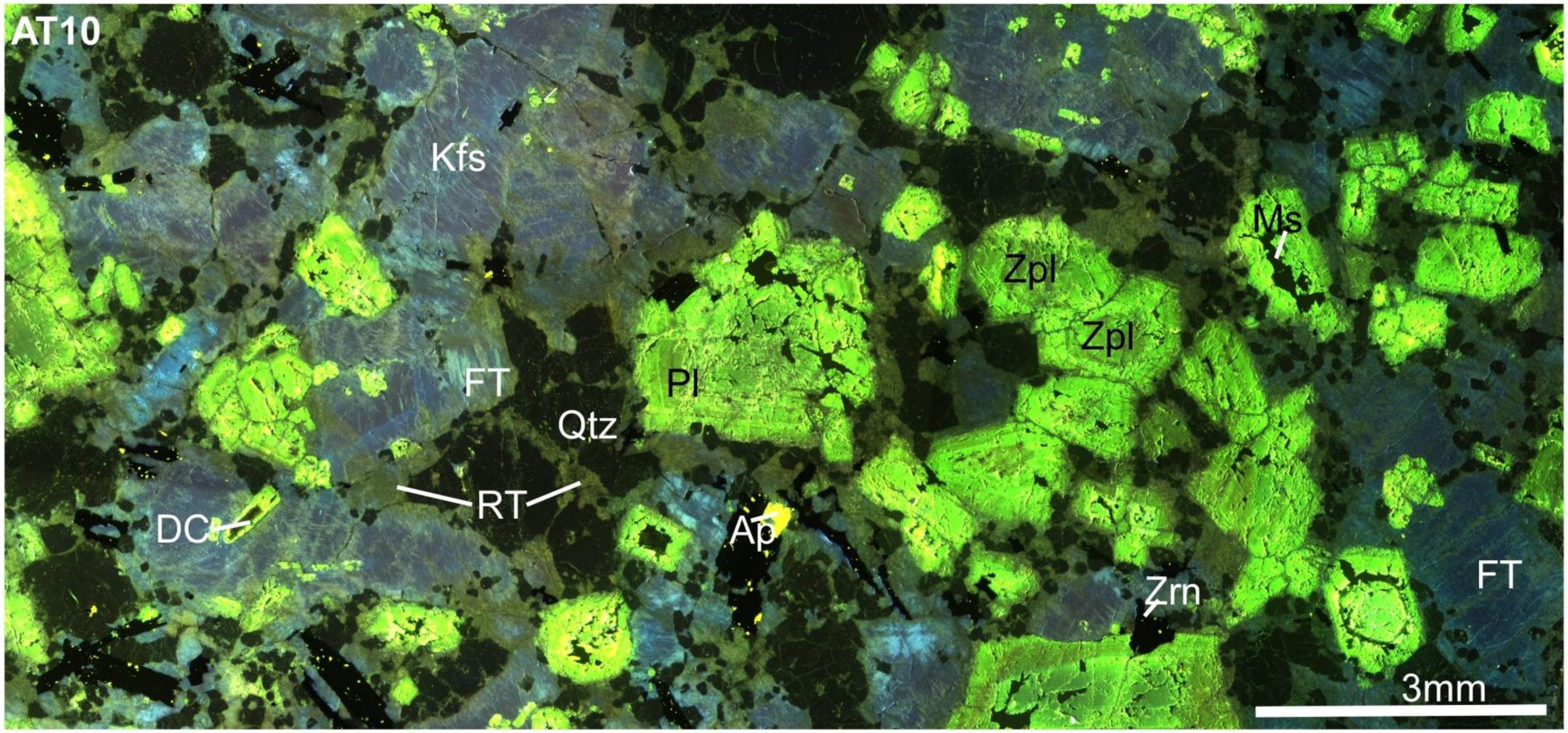

Figure 6-4: CL image of Koyunoba granitic sample AT10. Pl=plagioclase, Qtz= quartz, Kfs=alkali feldspar, Bt= biotite, Ms=muscovite, Cal=calcite, Ap=apatite, Zrn=zircon, ZPl=zoned plagioclase, DC= deteriorated cores, FT=flame textures, RT=reaction textures. Abbreviations after Kretz (1983).

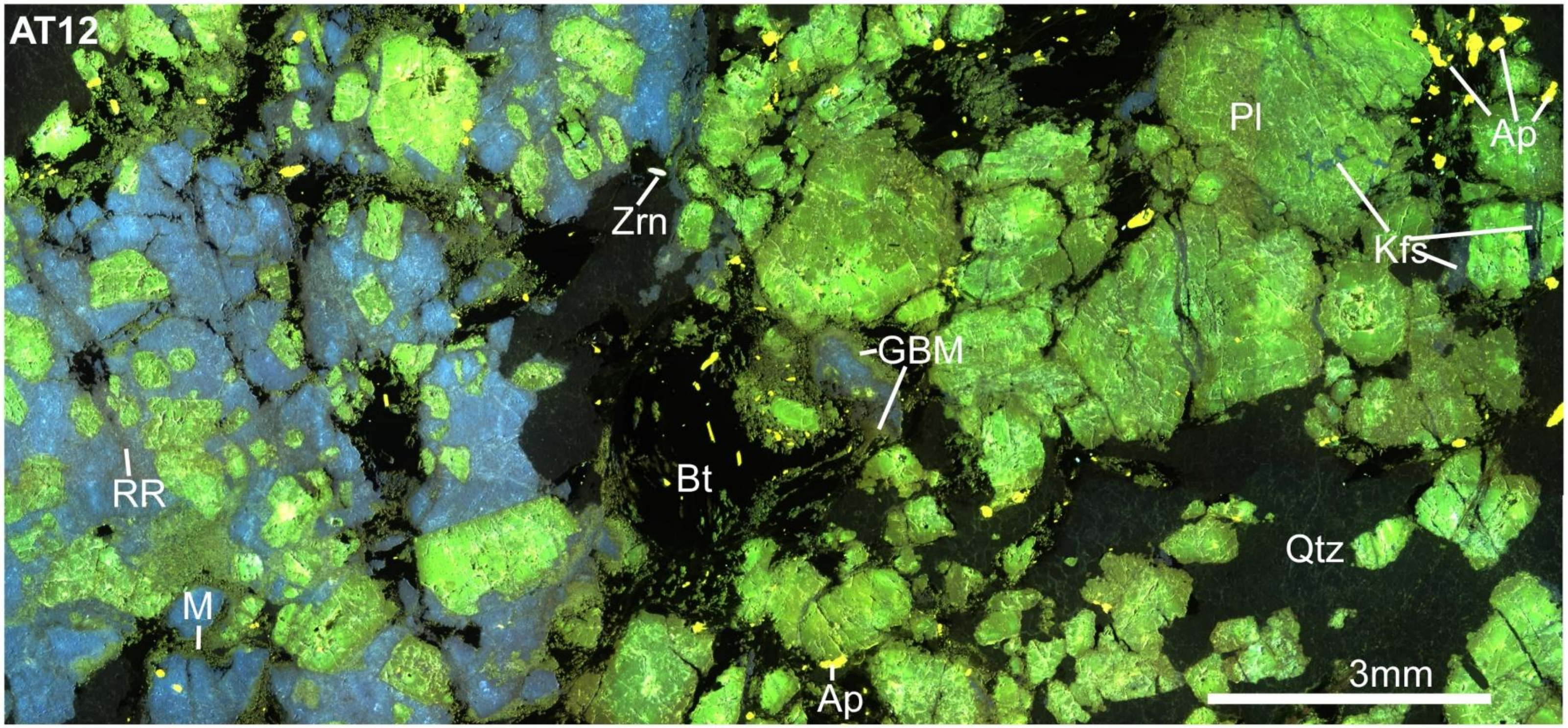

Figure 6-5: CL image of Koyunoba granitic sample AT12. Pl=plagioclase, Qtz= quartz, Kfs=alkali feldspar, Bt= biotite, Ap=apatite, Zrn=zircon, GBM=grain boundary migration, M=myrmekite, RR=red rims. Abbreviations after Kretz (1983).

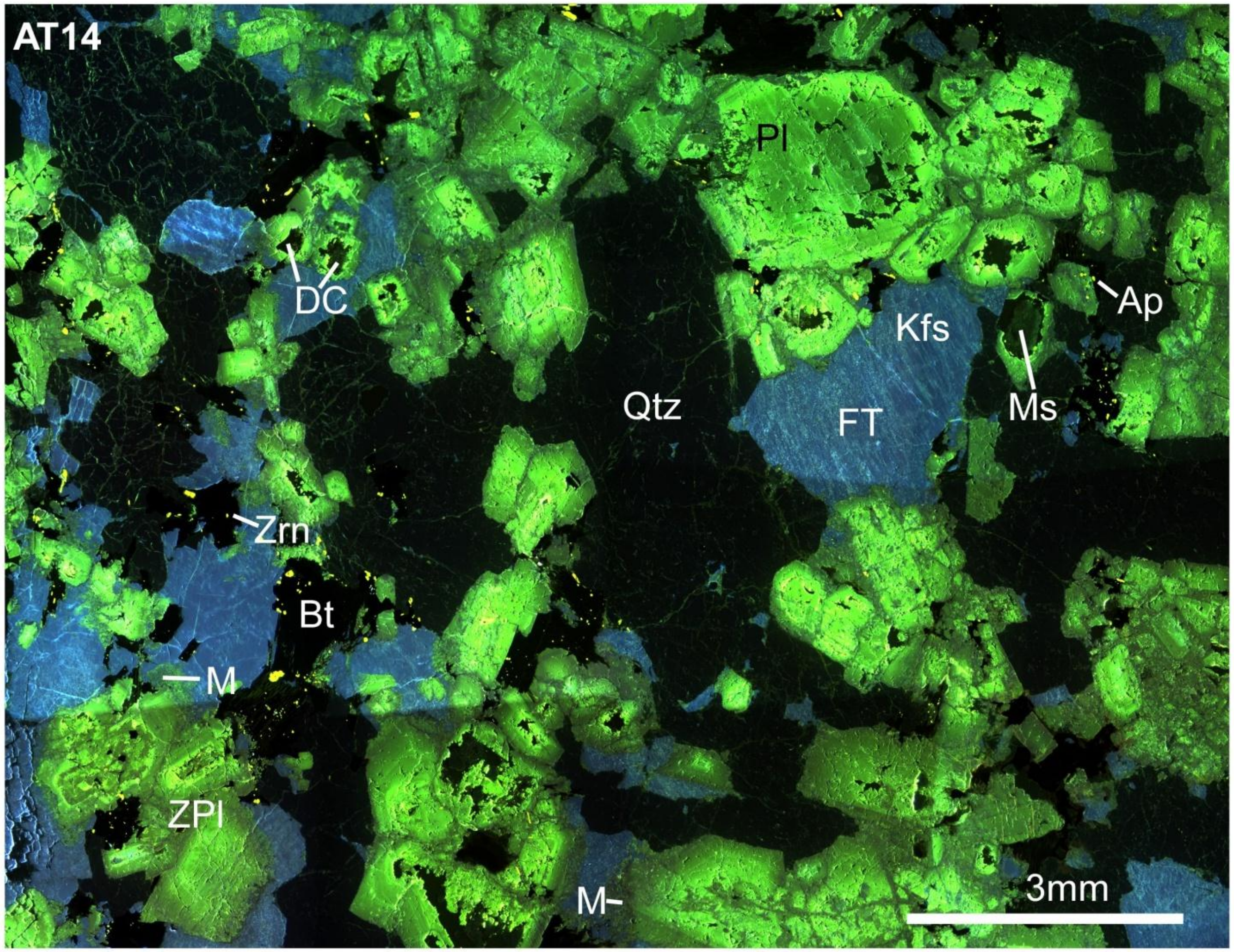

Figure 6-6: CL image of Koyunoba granitic sample AT14. Pl=plagioclase, Qtz= quartz, Kfs=alkali feldspar, Bt= biotite, Ms=muscovite, Ap=apatite, Zrn=zircon, ZPl=zoned plagioclase, DC=deteriorated cores, FT=flame texture, M=myrmekite. Abbreviations after Kretz (1983).

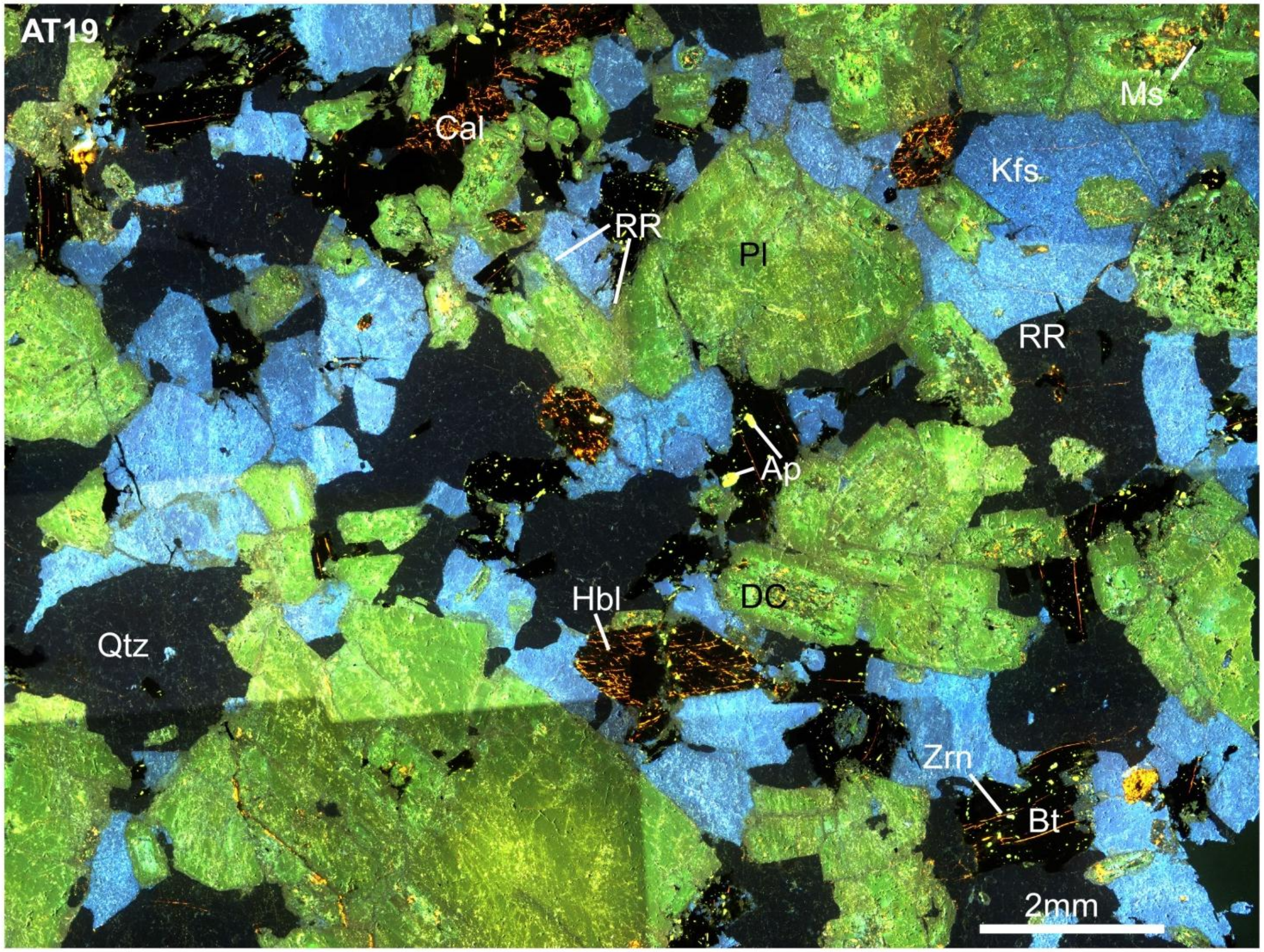

Figure 6-7: CL image of Alacam granitic sample AT19. Pl=plagioclase, Qtz= quartz, Kfs=alkali feldspar, Bt= biotite, Ms=muscovite, Cal=calcite, Hbl=hornblende, Ap=apatite, Zrn=zircon, DC=deteriorated cores, M=myrmekite, RR=red rims. Abbreviations after Kretz (1983).

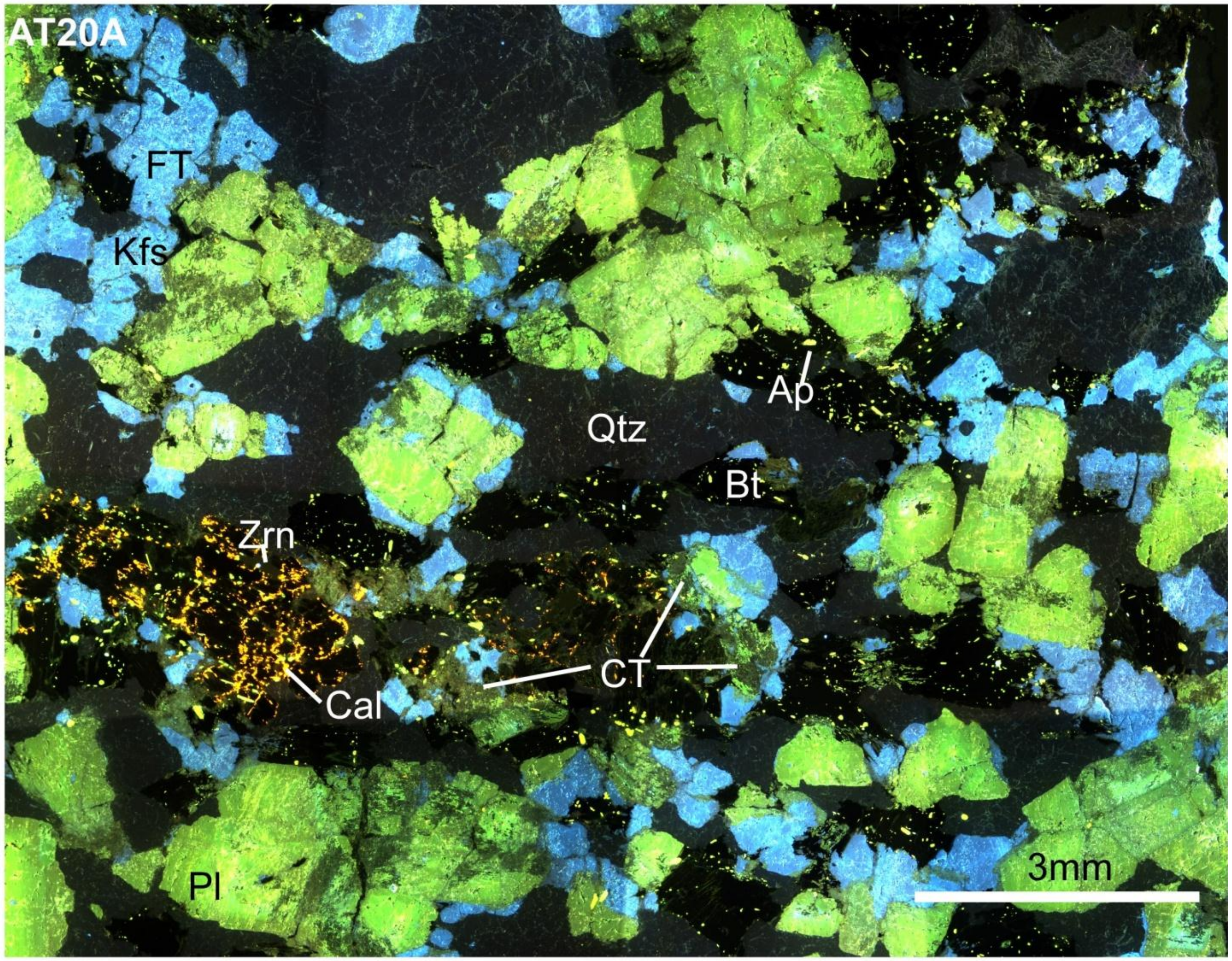

Figure 6-8: CL image of Alacam granitic sample AT20A. Pl=plagioclase, Qtz= quartz, Kfs=alkali feldspar, Bt= biotite, Cal=calcite, Ap=apatite, Zrn=zircon, FT=flame texture, CT=corroded textures. Abbreviations after Kretz (1983).

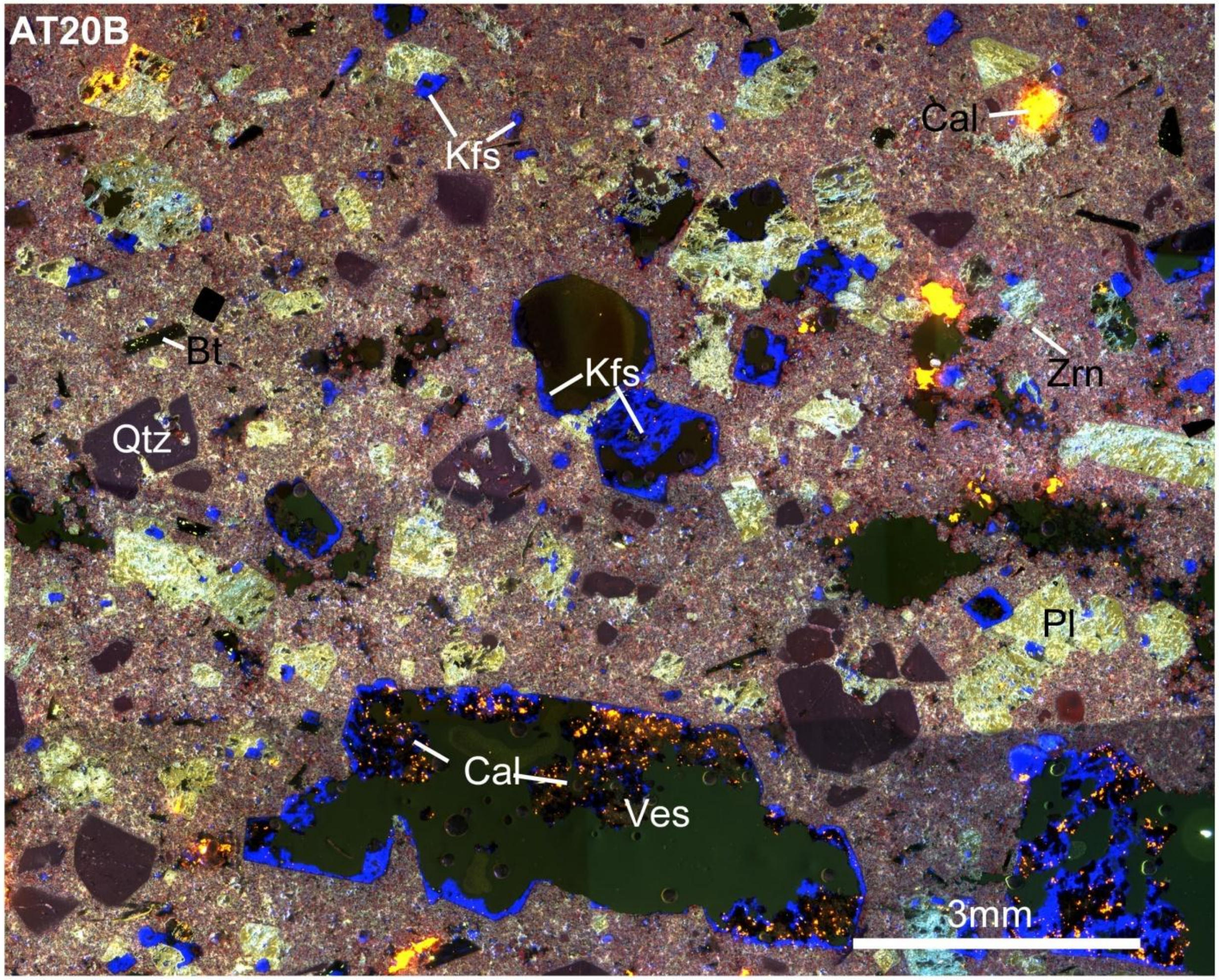

Figure 6-9: CL image of Alacam dacite dyke sample AT20B. Pl=plagioclase, Qtz= quartz, Kfs=alkali feldspar, Bt= biotite, Cal=calcite, Zrn=zircon, Ves=vesicle. Abbreviations after Kretz (1983).

Chapter 7: Geochronological Analyses and Discussion

7.1 INTRODUCTION

Zircon ($ZrSiO_4$) is one of the most commonly used minerals for isotopic age determinations due to its common occurrence in a wide variety of rocks, relative high abundance in uranium, high closure temperature (T_c > 800ºC, Cherniak and Watson, 2001), and resistance to age resetting (Schneider et al., 1999; Mouri et al., 2008). The internal structure of zircon grains visible by cathodoluminescence (CL) can exhibit complex zoning. Inherited cores from previous crystallization events may be present (Vavra, 1990; Pidgeon, 1992) and outer rims of zircons commonly time the latest crystallization event (e.g., Mouri et al., 2008).

In this study, *in situ* (in thin section) ages were obtained using the ion microprobe for eight samples (Egrigoz: WA12B, AT05A, AT15; Koyunoba: AT12, AT14; Alacam: AT19, AT20A, AT20B). The preservation of the zircon grain and rock fabric allows for a clear interpretation of the age. A detailed description of methods can be found in Chapter 3 of this thesis and is briefly reviewed here. Intensities of sputtered $^{94}Zr_2O$, ^{204}Pb, ^{206}Pb, ^{207}Pb, ^{208}Pb, Th, U, and UO ions were measured in 15 magnet cycles to calculate the ion microprobe age. A calibration curve was developed by calibrating the U-Pb sensitivity as a function of UO^+/U^+ of a standard zircon AS3 (Figure 7-1). Ideally the UO^+/U^+ ratio of the unknown zircon lies within the range defined by the standard's calibration curve, which ranges from 7.028±0.014 to 8.634±0.045. The calibration line used to calculate the ages in this thesis is UO^+/U^+=0.428($^{206}Pb^+/U^+$ RSF)+5.798±0.116. Reported ages are corrected for common lead either using the ^{204}Pb correction or the $^{206}Pb/^{208}Pb$ correction assuming common $^{206}Pb/^{204}Pb$=18.86, $^{207}Pb/^{204}Pb$=15.62, and $^{208}Pb/^{204}Pb$=38.34.

7.2 AGE OF THE EGRIGOZ PLUTON

Previously reported ages of the Egrigoz pluton range from 2972±13 Ma (inherited $^{207}Pb/^{206}Pb$ zircon; Ring and Collins, 2005) to 19.3±4.4 Ma (U-Pb zircon; Hasozbek et al., 2010) (see Table 2-1). The Archean age was reported from the core of a single zircon and is interpreted as an inherited age from previous crystallization events. Late Oligocene to early Miocene ages are often cited as timing pluton crystallization (e.g. Ring and Collins, 2005).

In this study, five zircons were dated from sample WA12B (Figure 7-2 and 7-3), four zircons were dated from sample AT05A (Figure 7-2 and 7-4), and five zircons were dated from sample AT16 (Figure 7-2 and 7-5, see Table 7-1). Sample WA12 was collected from the southern section of the pluton, AT16 from the core of the pluton, and AT05 from the northern section of the pluton (Figure 2-4).

Overall, zircon ages from the Egrigoz pluton yield late Oligocene to early Miocene ages ranging from 24.1±1.3 Ma to 15.9±0.9 Ma with an average of 20.0±1.1 Ma (±1σ) and a Mean Square Weighted Deviation (MSWD) of 4.7. MSWD measures the scatter of individual ages and has an expected value of one when the observed deviations from the regression line are within analytical error (Wendt and Carl, 1991). In our case, the dated samples are inconsistent with a single population.

Five zircon grains from southern section of the Egrigoz pluton (sample WA12B, Figure 2-4) yield Miocene ages. $^{206}Pb/^{238}U$ ages range from 22.2±1.1 Ma to 18.9±1.4 Ma (Figures 7-2 and 7-3, Table 7-1). The oldest zircon also yields a $^{207}Pb/^{235}U$ age of 22.8±2.3 Ma (zircon 5, Table 7-1). Four of the dated zircon grains are located within biotite grains and one zircon (zircon 4, 20.2±0.7 Ma) is located along a grain boundary between biotite, quartz, and altered alkali feldspar (Figure 7-3D). Three zircons are concordant while two zircons show reverse discordance on the concordia diagram (Figure

7-2A). When the two geochronometers, $^{206}Pb/^{238}U$ and $^{207}Pb/^{235}U$, give equivalent ages, the dated mineral is concordant and will plot on the line (Figure 7-2) (Faure, 1986). Note that in some cases, the $^{207}Pb/^{235}U$ ages yield large errors; we attribute this to ion microprobe detection limits in measuring small amounts of radiogenic ^{207}Pb. Reverse discordance may be due to radiogenic Pb gain brought in by hydrothermal fluids or analytical artifacts (Aleinikoff et al., 1993). The reverse discordance in Figure 7-2A is likely due to an overcorrection of the amount of common Pb in the dated grain.

Four zircon grains from the northern Egrigoz pluton (sample AT05A, Figure 2-4) yield late Oligocene to early Miocene ages from 24.1±1.3 Ma to 19.0±0.7 Ma (Figures 7-2 and 7-4, Table 7-1). One zircon (zircon 6, 19.5±0.9 Ma), located with iron oxide in a small biotite surrounded by alkali feldspar, also gave a $^{207}Pb/^{235}U$ age of 17.5±1.9 Ma. The youngest dated zircon (zircon 3, 19.0±0.7 Ma) is located between biotite and plagioclase. The oldest dated grain (zircon 4, 24.1±1.3 Ma) is located within plagioclase surrounding alkali feldspar. The other dated zircons (zircon 6, 19.5±0.9; zircon 2, 21.1±0.8 Ma) are located within grain boundaries between biotite and feldspar. All zircons are concordant (Figure 7-2B)

Five zircon grains from the core of the Egrigoz pluton (sample AT16, Figure 2-4) yield Miocene ages ranging from 22.6±2.0 Ma to 15.9±0.9 Ma (Figures 7-2 and 7-5, Table 7-1). Three zircons, including the youngest (zircon 5; 15.9±0.9 Ma) and the oldest (zircon 2, 22.6±2.0 Ma), are located within biotite grains. Two zircons (zircon 1, 17.1±0.8 Ma; zircon 4, 19.5±0.9 Ma) are both located within grain boundaries between biotite, quartz, and feldspar. Three zircons are concordant (Figure 7-2C), where as the youngest zircon 5 is reversely discordant. One zircon is discordant on the concordia diagram (zircon 4, 19.5±0.9 Ma). Discordance is common in zircons due to Pb loss (Faure, 1986).

7.3 AGE OF THE KOYUNOBA PLUTON

Previously reported ages of the Koyunoba pluton range from 540±96 Ma (inherited U-Pb zircon; Ring and Collins, 2005) to 19.9±3.1 Ma (U-Pb zircon; Ring and Collins, 2005) (see Table 2-1). The Cambrian aged-zircon likely formed during the Pan-African orogeny, whereas the Miocene ages have been attributed again to pluton crystallization (e.g., Ring and Collins, 2005).

In this study, six zircons were dated from sample AT12 (Figures 7-6 and 7-7) and four zircons were dated from sample AT14 (Figures 7-6 and 7-8, Table 7-2). AT12 was collected from the eastern section and AT14 was collected from the northern section of the pluton (Figure 2-4). Overall, zircon ages from the Koyunoba pluton yield late Oligocene to early Miocene ages ranging from 29.9±3.9 Ma to 14.6±2.6 Ma, with an average of 22.6±2.2 Ma (±1σ) and MSWD of 2.8.

Six zircon grains from the eastern section of the Koyunoba pluton (sample AT12, Figure 2-4) were dated and range from 29.9±3.9 Ma to 19.7±2.7 Ma (Figures 7-6 and 7-7, Table 7-2). Two spots on the largest zircon, located within a biotite grain with quartz inclusions, yield ages of 24.3±1.5 Ma and 20.3±1.2 Ma. The oldest dated zircon in this sample (zircon 3, 29.9±3.9 Ma) is surrounded by iron oxide within a biotite grain. The youngest dated zircon (zircon 2, 19.7±2.7 Ma) and the largest (zircon 5, 20.3±1.2 Ma and 24.3±1.5 Ma) lie within biotite grains. One zircon is located within plagioclase (zircon 4, 23.8±1.5 Ma) and one is located within a crack (zircon 6, 20.7±2.3 Ma). Five zircons are concordant and one zircon (zircon 5, two spots) shows reverse discordance on the concordia diagram (Figure 7-6A).

Four zircon grains were dated from the northern section of the Koyunoba pluton (sample AT14, Figure 2-4) and yield late Oligocene to Miocene ages ranging from 26.5±2.5 Ma to 14.6±2.6 Ma (Figures 7-6 and 7-8). The oldest zircon (zircon 1, 26.5±2.5

Ma) is located within a quartz inclusion in biotite. The youngest zircon (zircon 2, 14.6±2.6) is located at the edge of a biotite grain. The core of the biotite contains a zircon that yields 21.8±1.4 Ma (zircon 3). One zircon is located within quartz (zircon 4, 21.3±1.1). Four zircons are concordant and one zircon (zircon 3) is discordant (Figure 7-6B).

7.4 Age of the Alacam pluton

Previously reported ages of the Alacam pluton range from 38.5±1.8 Ma (K-Ar orthoclase; Bingol et al., 1982) to 20.2±1.4 Ma (U-Pb zircon; Hasozbek et al., 2010) (see Table 2-1). The late Eocene age may document the closing of the Neotethys Ocean. Similar to the Egrigoz and Koyunoba plutons, crystallization of the Alacam pluton is thought to be early Miocene (e.g., Hasozbek et al., 2010).

In this study, three zircons were dated from sample AT19 (Figures 7-9 and 7-10), four were dated from sample AT20A (Figures 7-9 and 7-11), and one was dated from sample AT20B (Figures 7-9 and 7-12) (see Table 7-3). All samples were collected from roughly the same location (Figure 2-4). Overall, zircon ages from the Alacam pluton yield late Oligocene to Miocene ages ranging from 25.2±1.5 Ma to 17.2±0.9 Ma with an average age of 20.8±1.4 Ma (±1σ) and MSWD of 4.9.

Three zircons grains from sample AT19 were dated and range from 25.2±1.5 Ma to 19.7±1.9 Ma (Figures 7-9 and 7-10, Table 7-3). The youngest zircon (zircon 3, 19.7±1.9 Ma) is located within a deteriorating plagioclase grain surrounded by biotite. Two zircons (zircon 1, 20.6±2.1 Ma and zircon 2, 25.2±1.5 Ma) are located within biotite grains. All zircons are concordant (Figure 7-9A)

Four zircon grains from sample AT20A (Figures 7-9 and 7-11, Table 7-3) were dated and range from 22.6±1.4 Ma to 18.8±0.8 Ma. The oldest zircon grain (zircon 2, 22.6±1.4 Ma) is located within quartz. Two zircons, including the youngest (zircon 3, 18.8±0.8 Ma) are located within biotite grains with apatite inclusions. One zircon (zircon 1, 20.8±1.1 Ma) is located within grain boundaries between deteriorating plagioclase and biotite. Two zircons (zircon 1, 20.8±1.1 Ma and zircon 2, 22.6±1.4 Ma) are concordant and two (zircon 3, 18.8±0.8 Ma and zircon 4, 21.8 ± 1.1 Ma) show reverse discordance on the concordia diagram (Figure 7-9B).

One zircon grain from sample AT20B yielded 17.2±0.9 Ma (Figures 7-9 and 7-12, Table 7-3). Sample AT20B was collected from a dacite dyke within the Alacam pluton and the zircon, which is located within the quartz/alkali feldspar groundmass, is the youngest found in the pluton. The zircon shows reverse discordance on the concordia diagram (Figure 7-9B, zircon 5).

7.5 Discussion

Ages from the Egrigoz, Koyunoba, and Alacam plutons range from 29.9±3.9 Ma to 14.6±2.6 Ma, with an average of 21.0±1.2 Ma (Figure 7-13). All dated zircons plot near concordia. Due to uncertainty in measurements, it is difficult to evaluate if the grains were initially Oligocene but experienced mid Miocene Pb loss. Reverse discordance is likely due to an overcorrection of the amount of common Pb in the dated grain. Large uncertainties in some of the $^{207}Pb/^{235}U$ ages are due to small amounts of these isotopes in the measured samples.

The majority of zircons are within or adjacent to biotite grains and range in size from 10-120µm. Due to their small size, we cannot see chemical differences or zoning patterns in the zircons that would assist in identifying clear core/rim relationships. However, no pattern between textural relationships within the thin sections and ion microprobe ages was found. For example, in the Egrigoz pluton, sample WA12 has an

18.9±1.4 Ma age in the core of a biotite grain (Figure 7-3A and B) and also shows a 22.2±1.1 Ma age in the rim of a grain (Figure 7-3E and F). Finding zircons cluster near biotite is a common igneous texture (Mackenzie and Guilford, 1980), and suggests that they are products of crystallization, rather than inheritance. If the zircon grains were assimilated from an external source, the expectation is that they would be texturally scattered throughout the sample. In addition, zircon grains in a magmatic pluton are expected to show similar size and morphological character unless complex magma intrusions have occurred and rounding of grains are due to resorption (Deer et al., 1992).

To further assist in interpreting the ages, we used the geochemistry of the rock to estimate the zircon saturation temperatures of the Egrigoz, Koyunoba, and Alacam plutons, which average 782±13°C (Watson and Harrison, 1983, Table 7-4). Zircon saturation temperatures are interpreted as estimating initial magma temperature at the source (e.g., Miller et al., 2003). In our samples, no relationship is found between ion microprobe age and zircon saturation temperature. A greater zircon saturation temperature is commonly observed in I-type granites (800-900°C) than for S-type granites (≤700°C) (Watson and Harrison, 1983). The calculated zircon saturation temperature of our dated samples lies between S-type and I-type. These relatively high temperatures would result in the dissolution of most inherited zircons before attainment of saturation thus explaining the lack of inherited grains found in our samples (Watson and Harrison, 1983).

The Rhodope Massif, approximately 200km to the north, was intruded by granitoids of similar Oligocene age (29±1 Ma to 33±2 Ma; Dinter, 1998). Oligocene ages are also found in the Evciler pluton of the Kazdag metamorphic core complex to the west (25.0±0.3 Ma; Birkle and Satir, 1995). The Kazdag Massif, located south of the Rhodope, is largely thought to have been created during the Late Oligocene (Papanikolaou and

Demirtasli, 1987; Okay and Satir, 2000; Okay et al., 2008). Late Miocene ages are documented for granitoids within the central Menderes Massif (Salihi and Turgutlu plutons: 15.0±2.8 Ma; Catlos et al., 2010; 15.0±0.3 Ma and 16.1±0.2 Ma; Glodny and Hetzel, 2007). The ages of the dacite dyke are consistent with ages of acid volcanic domes in the northern Menderes Massif (17.3±0.4 Ma; Seyitoglu et al., 1992). Ages are consistent with the hypothesis that magmatism in the Aegean occurred in pulses beginning in the Eocene and continuing into the Miocene, and largely propagating from north to south (Dilek and Altunkaynak, 2007).

The range of ages reported here suggest that the Egrigoz, Koyunoba, and Alacam plutons crystallized over a ~15 m.y. time frame, predominantly centered around 21 Ma. These plutons may have started to crystallize as early as the Oligocene and were crystallized by middle Miocene. The CL textures suggest the plutons are products of magma mixing and have experienced some fluid-rock interactions during either crystallization or exhumation.

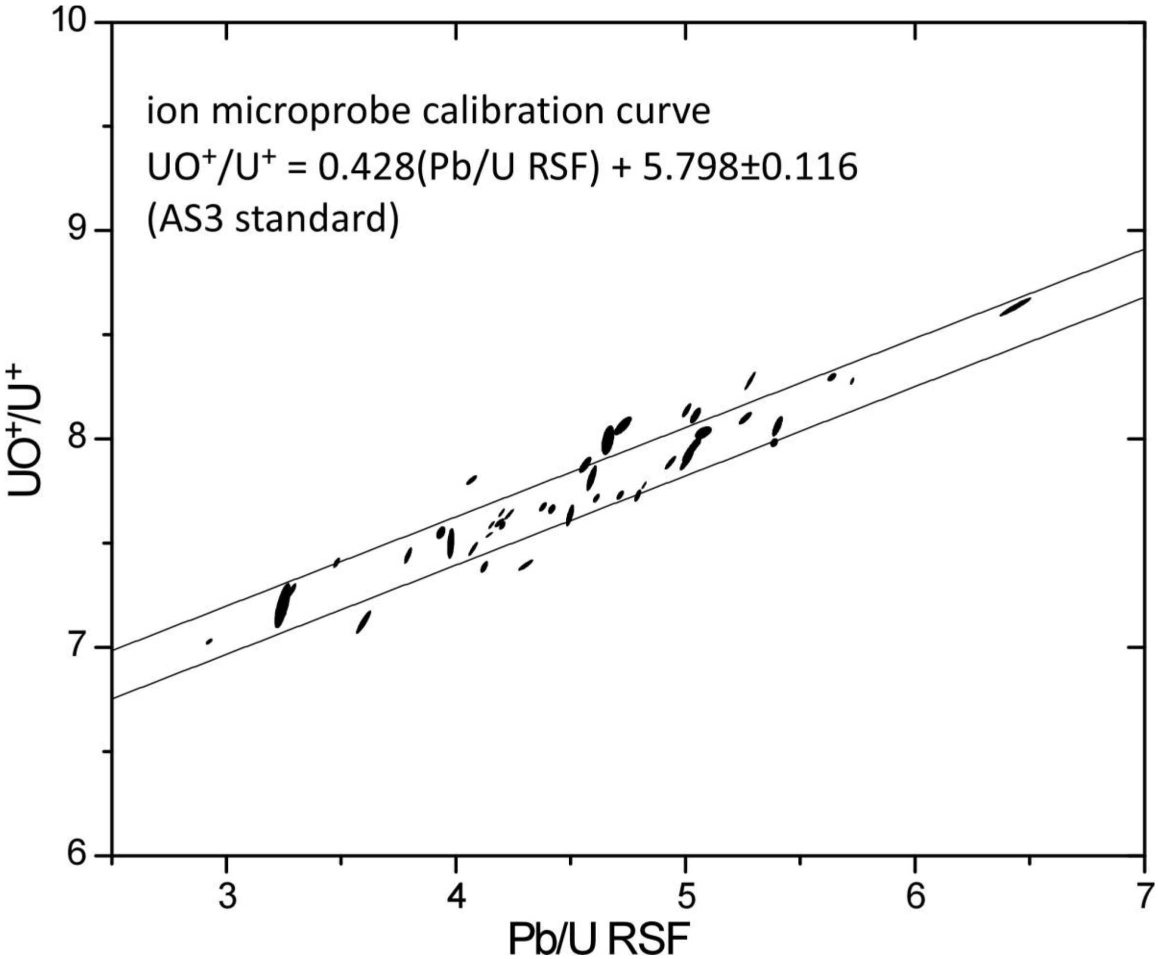

Figure 7-1: Ion microprobe calibration of UO+/U+ vs. Pb/U Relative sensitivity factor (RSF). This curve was developed using zircon standard AS3 that has an age of 1099 Ma±1σ (Schneider et al., 1999)

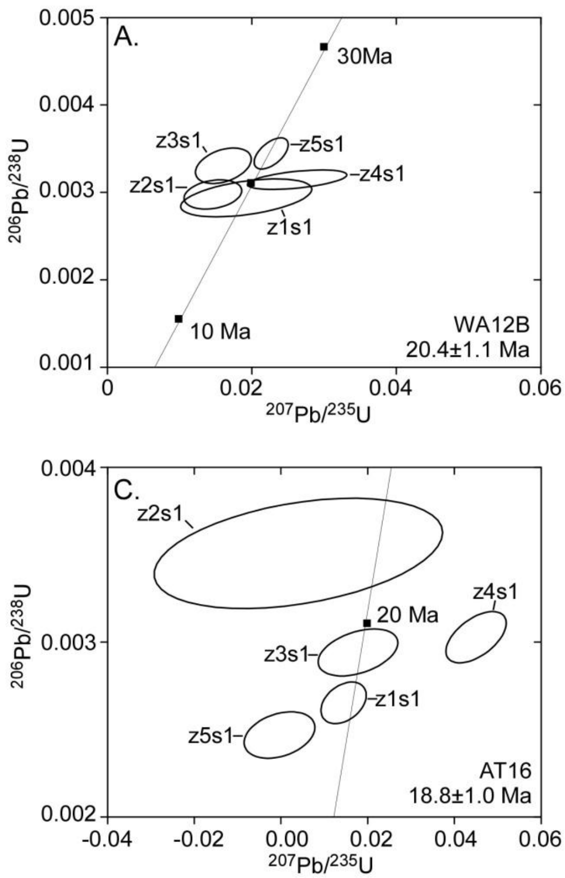

Figure 7-2: Concordia diagrams from the Egrigoz pluton samples (A) WA12B, (B) AT05A, and (C) AT16. Ages on concordia are provided for reference. Nomenclature (z#s#) refers to the zircon number and spot number. Average $^{206}Pb/^{238}U$ age is provided for each sample

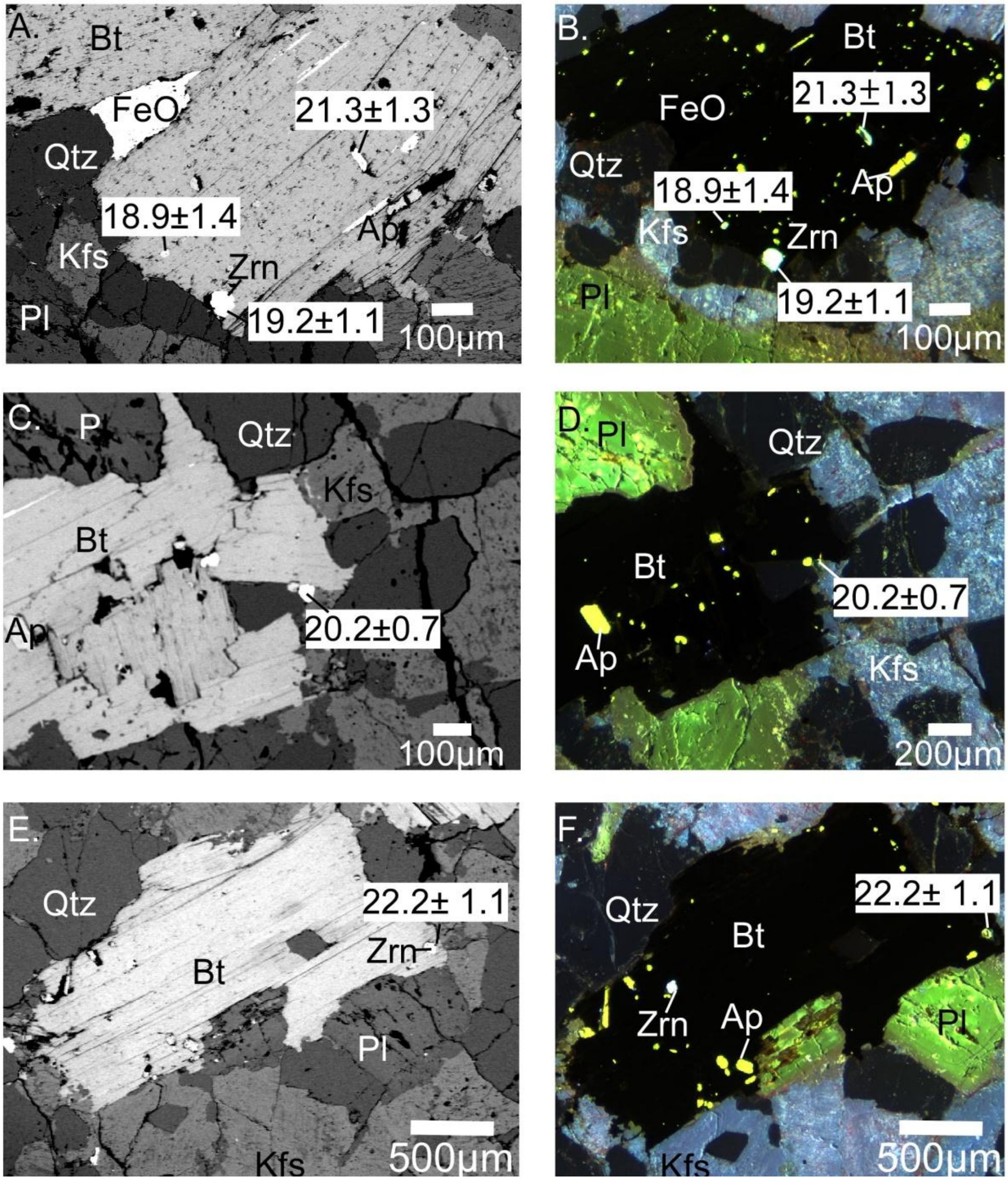

Figure 7-3: Backscatter electron (BSE) and corresponding cathodoluminescence (CL) images of *in situ* dated zircons from sample WA12 of the Egrigoz pluton. Mineral abbreviations after Kretz (1983). Ages are reported in millions of years.

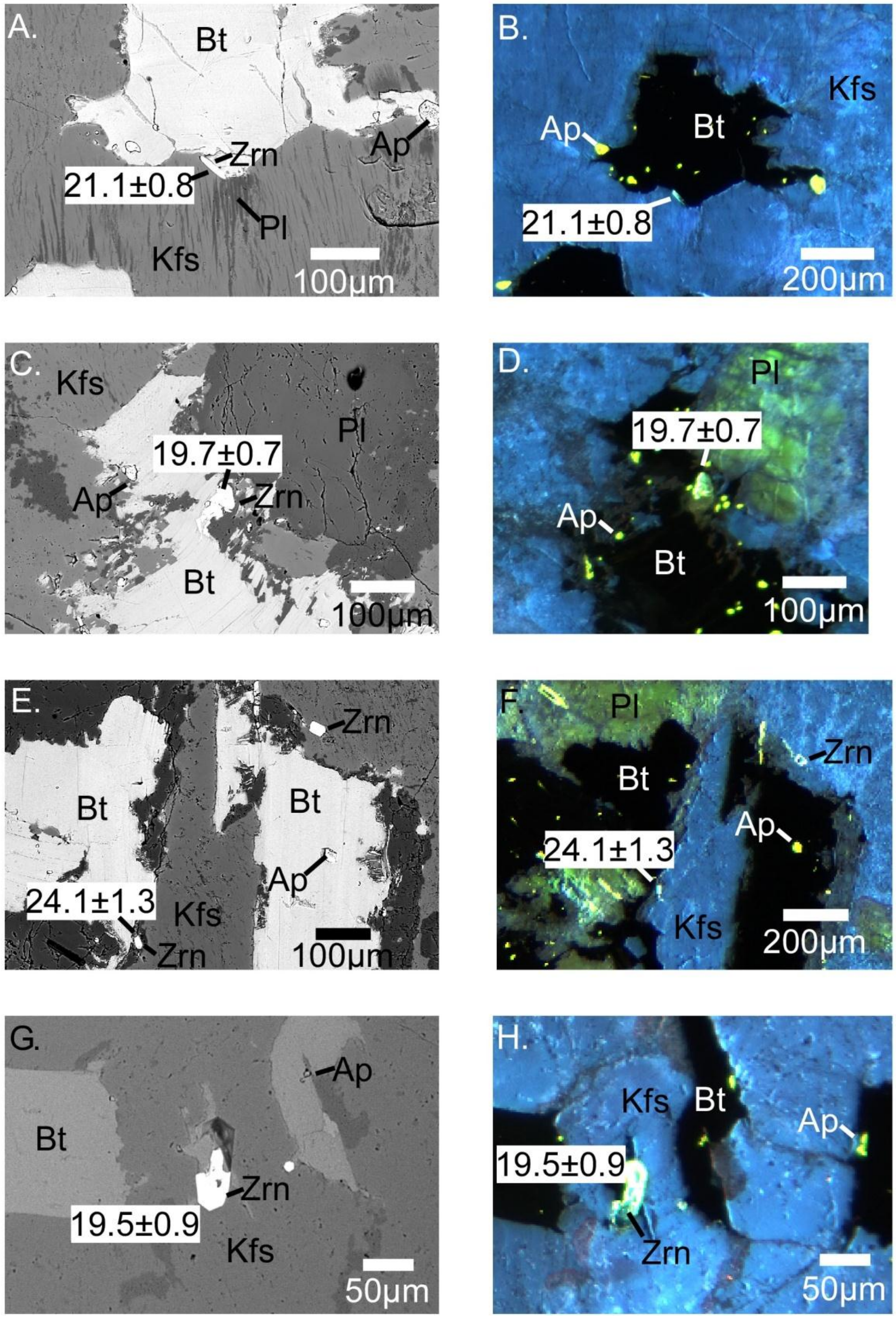

Figure 7-4: Backscatter electron (BSE) and corresponding cathodoluminescence (CL) images of *in situ* dated zircons from sample AT05A of the Egrigoz pluton. Mineral abbreviations after Kretz (1983). Ages are reported in millions of years.

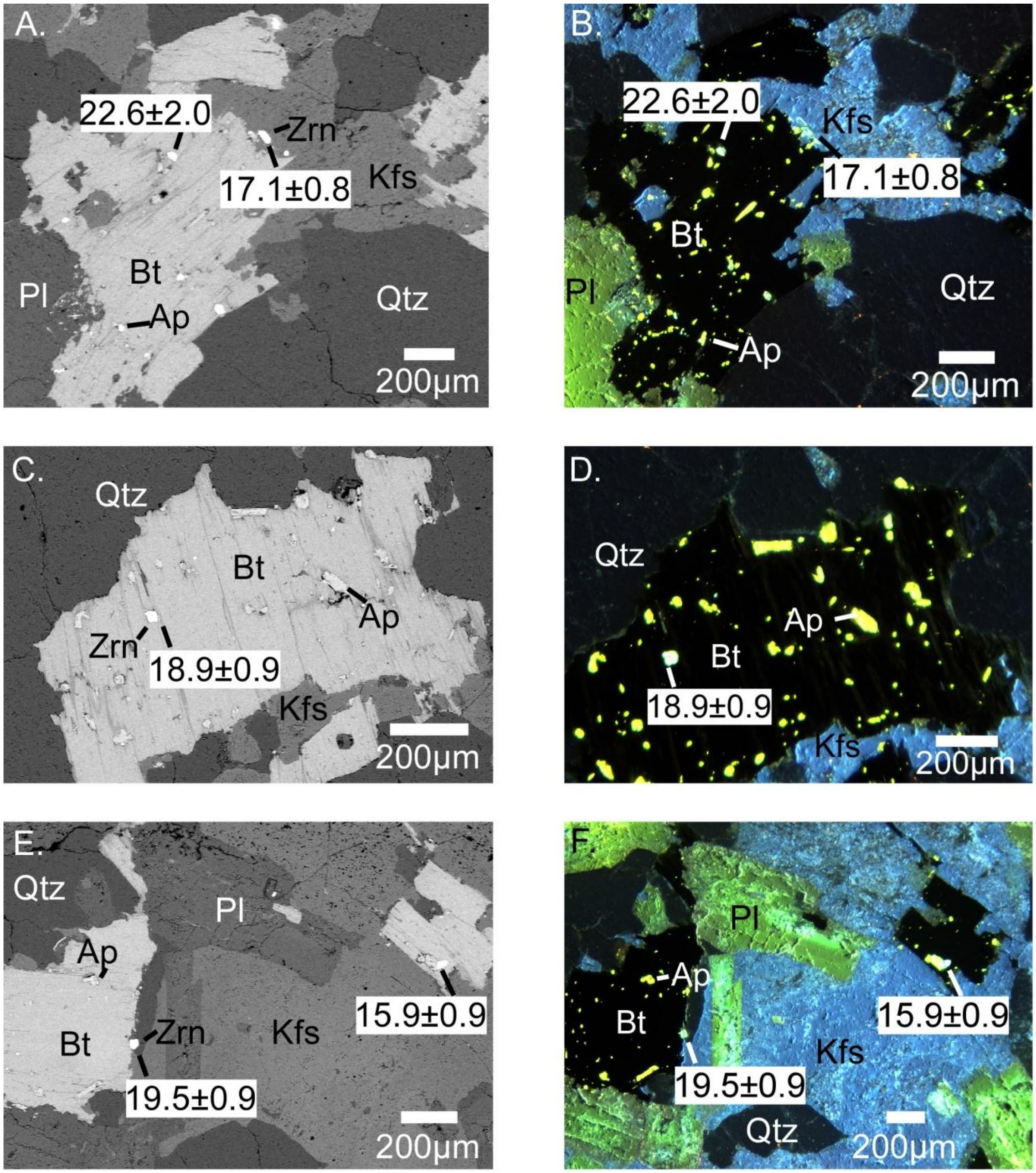

Figure 7-5: Backscatter electron (BSE) and corresponding cathodoluminescence (CL) images of *in situ* dated zircons from sample AT16 of the Egrigoz pluton. Mineral abbreviations after Kretz (1983). Ages are reported in millions of years.

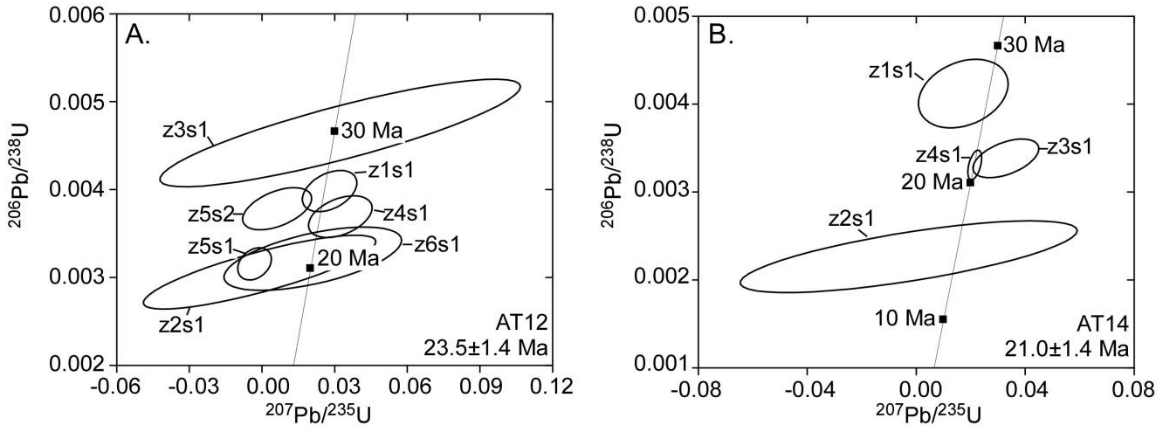

Figure 7-6: Concordia diagrams from the Koyunoba pluton samples (A) AT12 and (B) AT14. Ages on concordia are provided for reference. Nomenclature (z#s#) refers to the zircon number and spot number. Average $^{206}Pb/^{238}U$ age is provided for each sample.

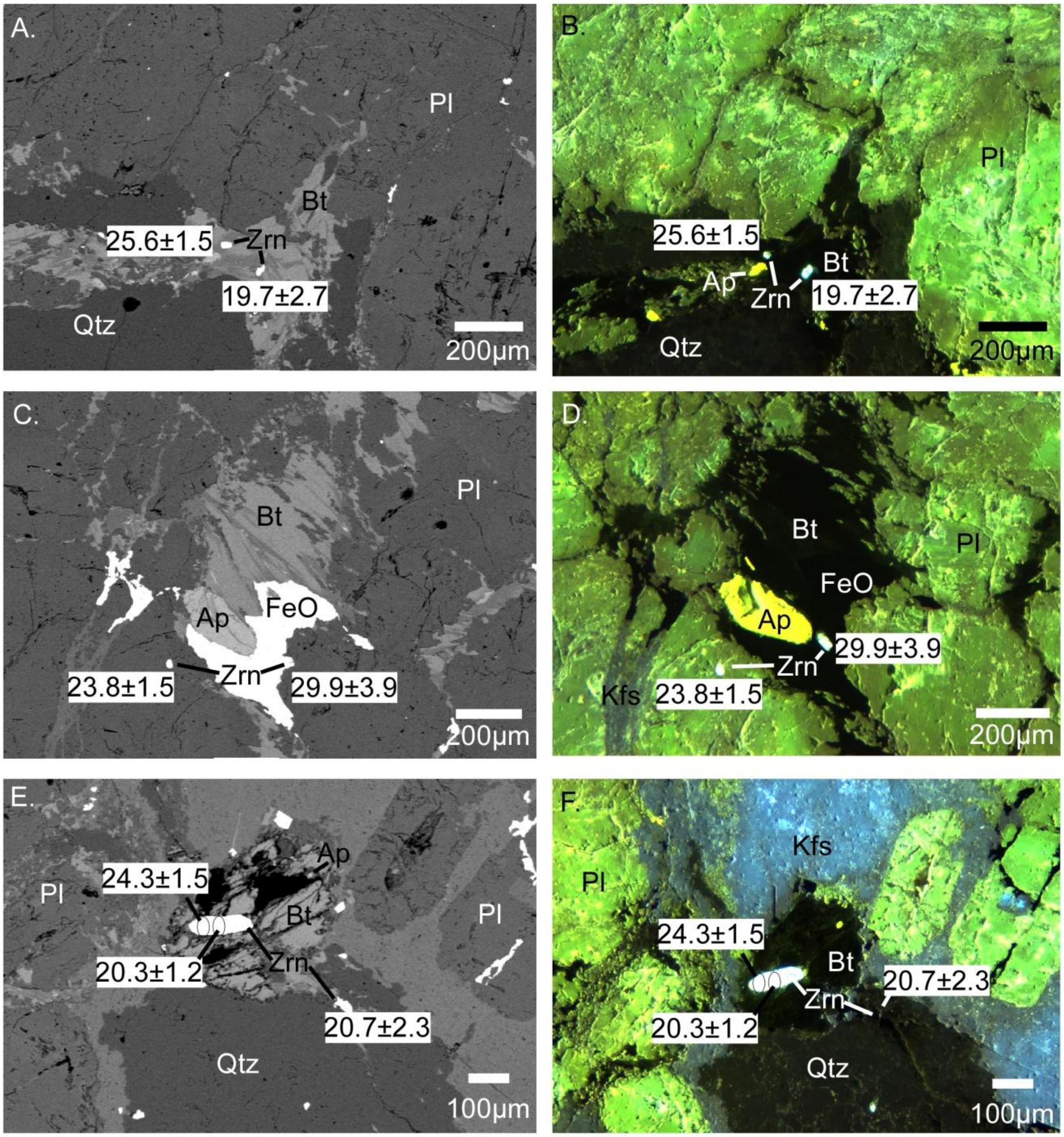

Figure 7-7: Backscatter electron (BSE) and corresponding cathodoluminescence (CL) images of *in situ* dated zircons from sample AT12 of the Koyunoba pluton. Mineral abbreviations after Kretz (1983). Ages are reported in millions of years.

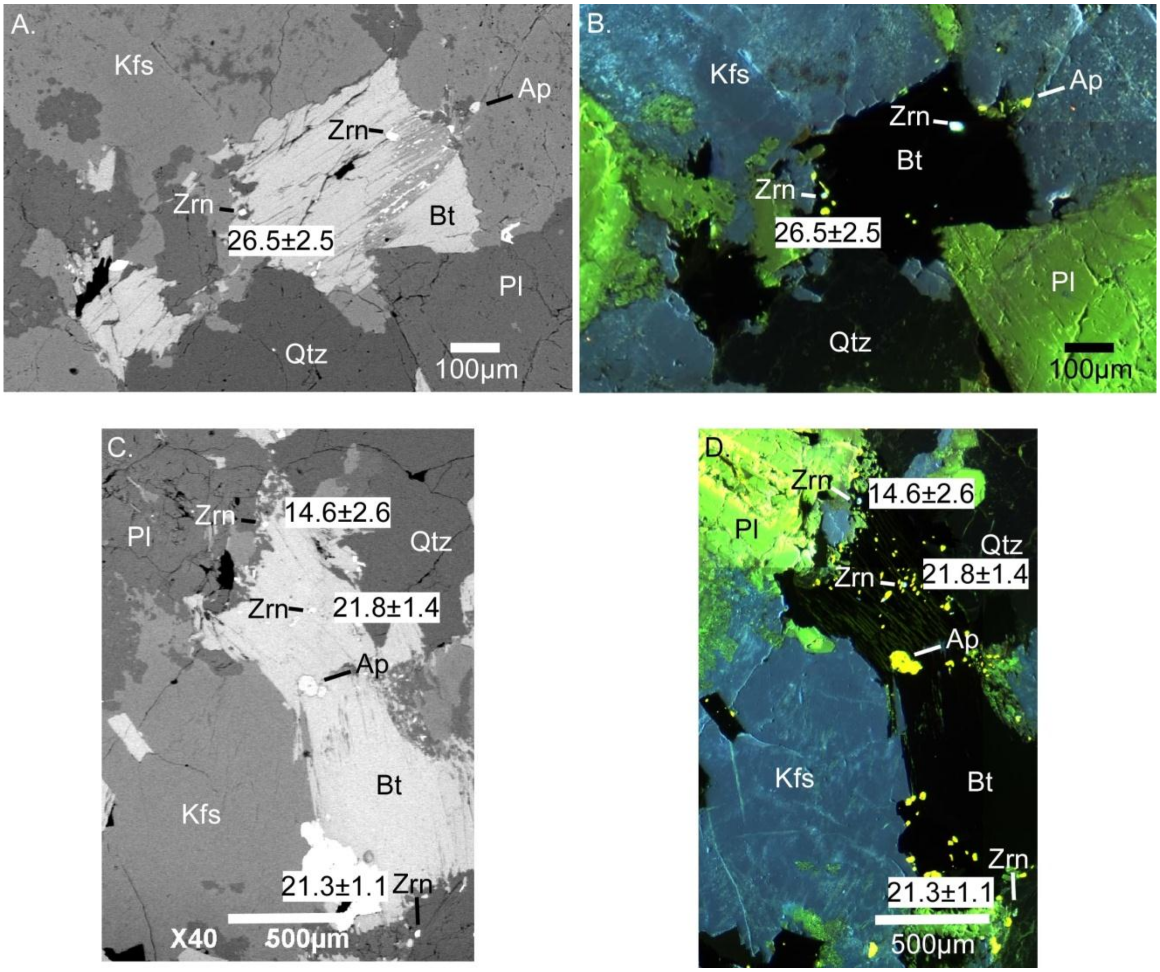

Figure 7-8: Backscatter electron (BSE) and corresponding cathodoluminescence (CL) images of *in situ* dated zircons from sample AT14 of the Koyunoba pluton. Mineral abbreviations after Kretz (1983). Ages are reported in millions of years.

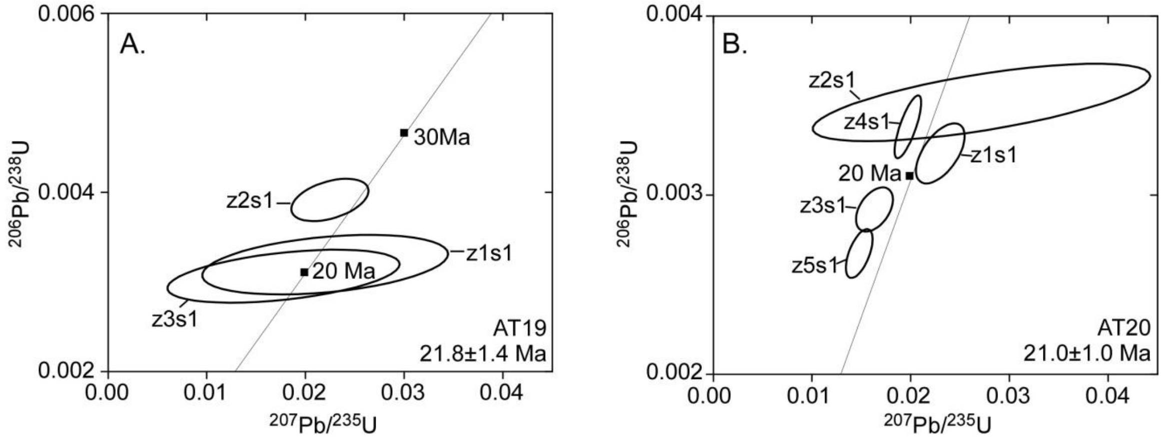

Figure 7-9: Concordia diagrams from the Alacam pluton samples (A) AT19 and (B) AT20. Ages on concordia are provided for reference. Nomenclature (z#s#) refers to the zircon number and spot number. Average $^{206}Pb/^{238}U$ age is provided for each sample.

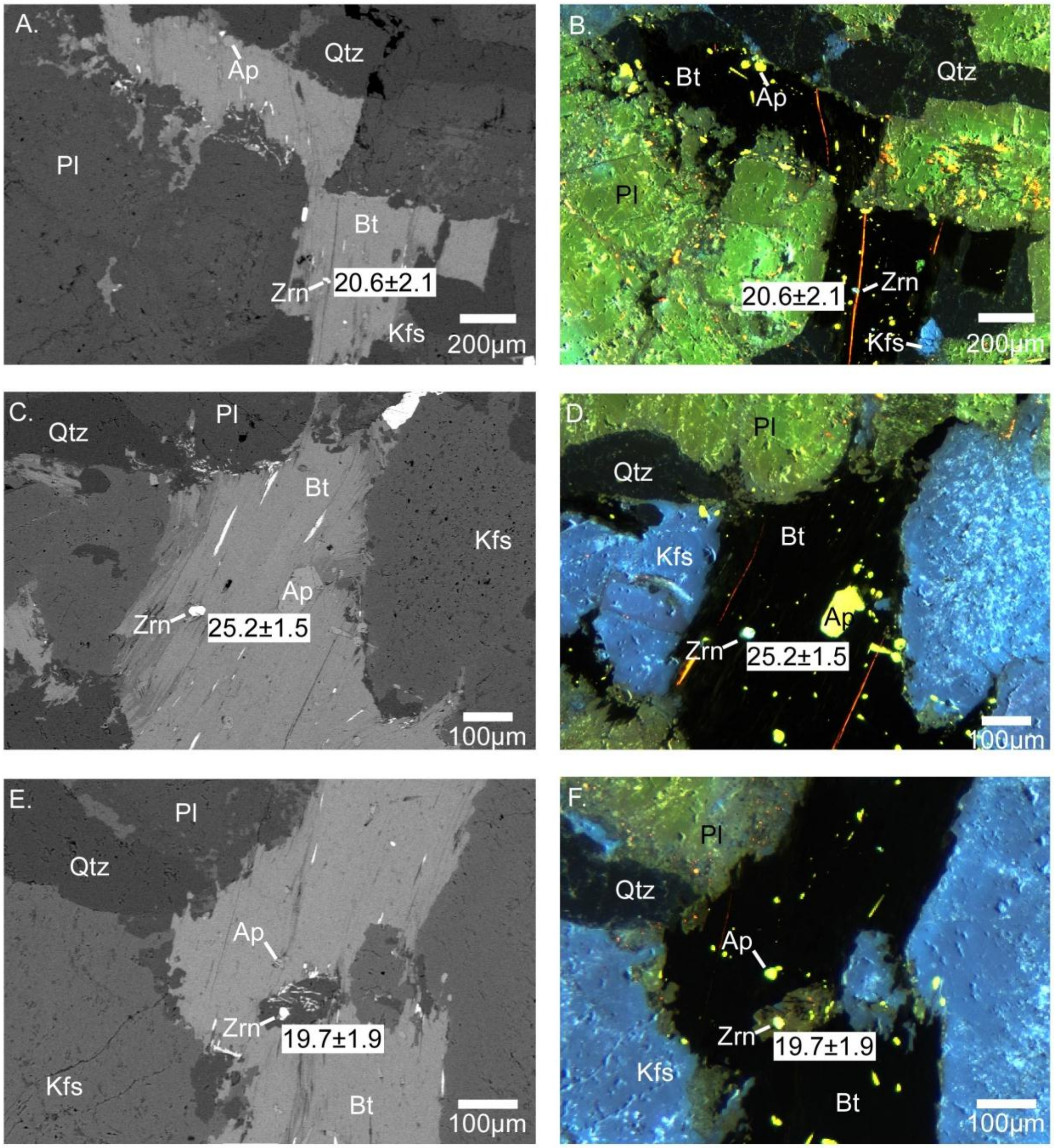

Figure 7-10: Backscatter electron (BSE) and corresponding cathodoluminescence (CL) images of *in situ* dated zircons from sample AT19 of the Alacam pluton. Mineral abbreviations after Kretz (1983). Ages are reported in millions of years.

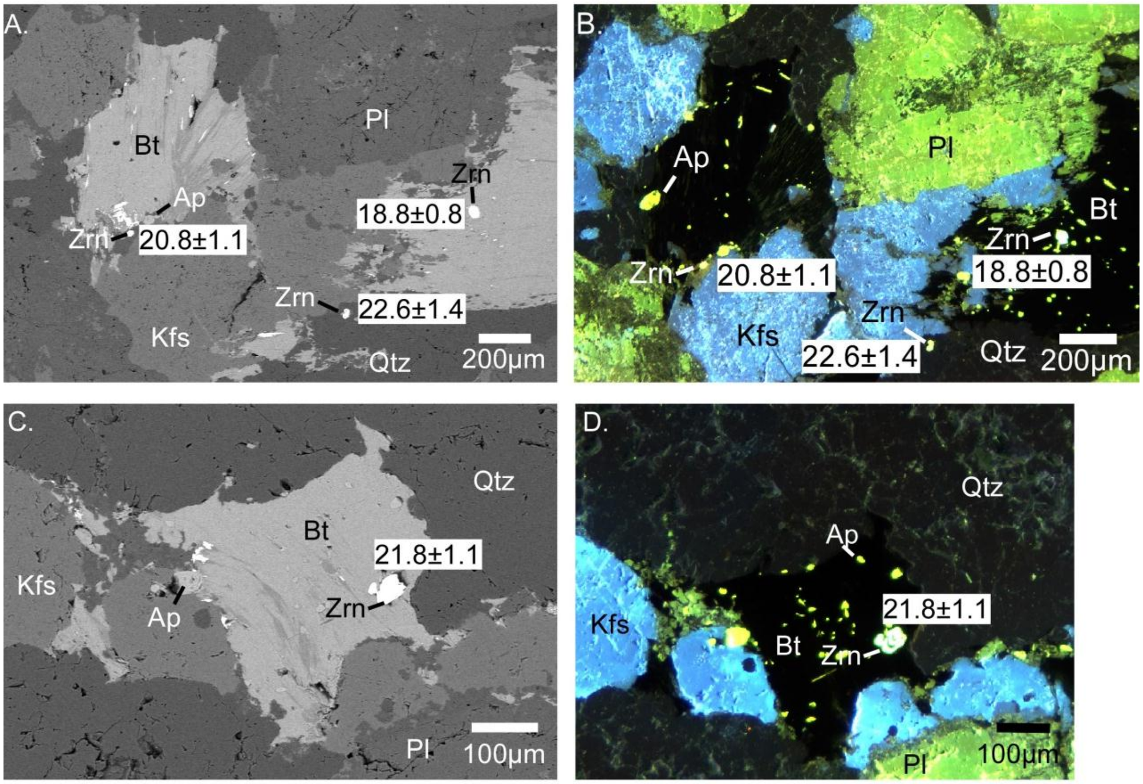

Figure 7-11: Backscatter electron (BSE) and corresponding cathodoluminescence (CL) images of *in situ* dated zircons from sample AT20A of the Alacam pluton. Mineral abbreviations after Kretz (1983). Ages are reported in millions of years.

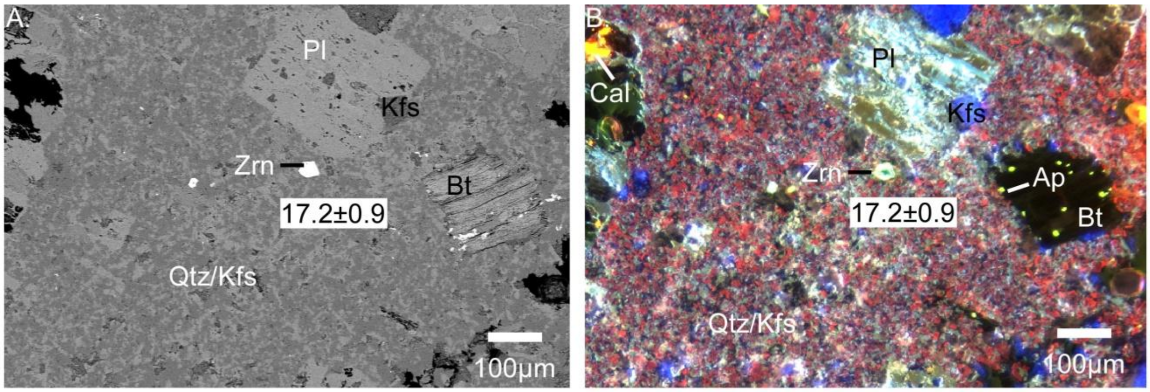

Figure 7-12: Backscatter electron (BSE) and corresponding cathodoluminescence (CL) images of the *in situ* dated zircon from sample AT20B, a dacite dyke within the Alacam pluton. Ages are reported in millions of years.

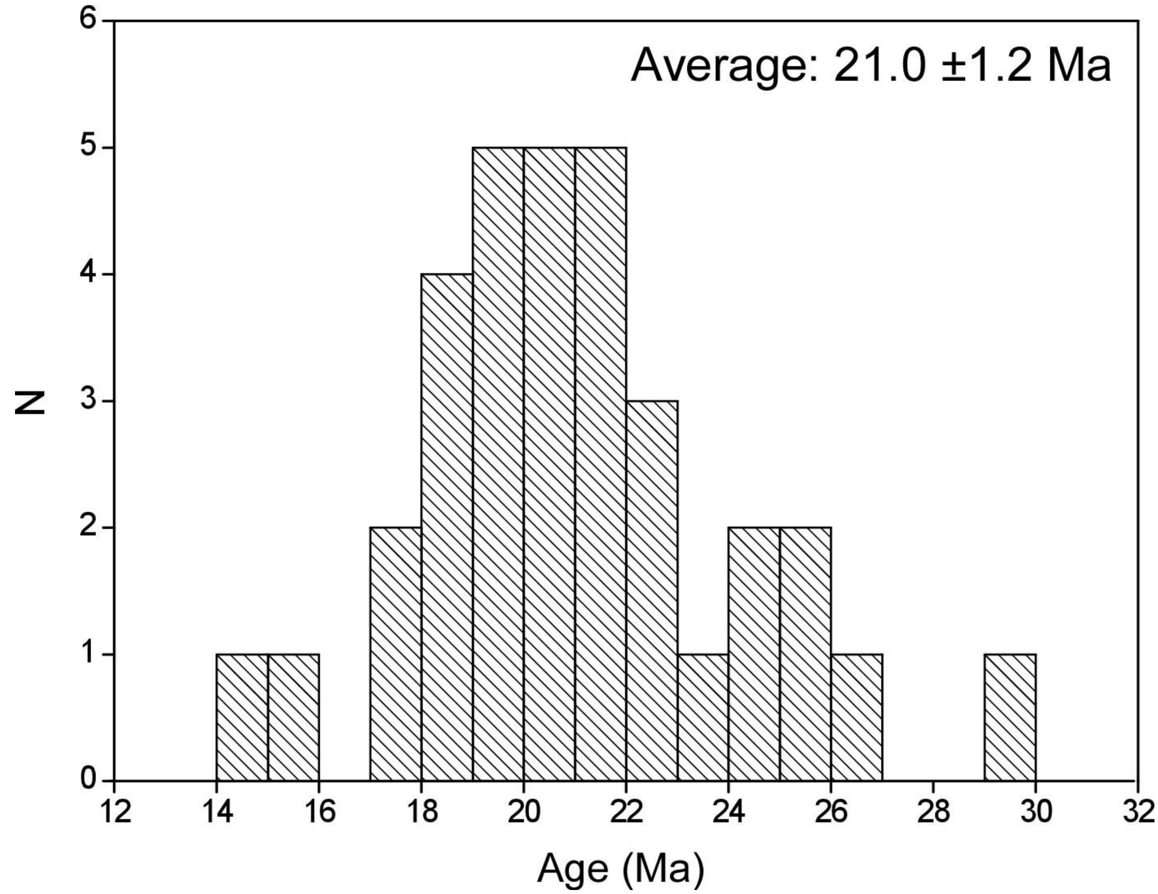

Figure 7-13: Histogram of ion microprobe ages from the Egrigoz, Koyunoba, and Alacam plutons. Ages range from 29.9±3.9 Ma—14.6±2.6 Ma with an average age of 21.0±1.2 Ma.

Table 7-1: ^{206}Pb/^{238}U ion microprobe zircon ages from the Egrigoz pluton.

zircon#_spot#	^{206}Pb/^{238}U Age ±1σ	^{206}Pb*% ±1σ	^{206}Pb*/^{238}U ±1σ	^{207}Pb*/^{235}U ±1σ	UO+/U+ ±1σ
AT16 (39° 16' 30.10" N 29° 03' 25.50" E)					
z2_s1	22.6±2.0	14.6±5.3	3.507E-03 ±3.157E-04	3.992E-03 ±3.328E-02	7.485±0.038
z4_s1	19.5±0.9	92.1±1.6	3.028E-03 ±1.469E-04	4.501E-02 ±6.954E-03	8.416±0.029
z3_s1	18.9±0.9	79.8±1.9	2.941E-03 ±1.346E-04	1.777E-02 ±9.206E-03	8.854±0.046
z1_s1	17.1±0.8	81.7±1.4	2.652E-03 ±1.188E-04	1.444E-02 ±5.222E-03	8.773±0.053
z5_s1	15.9±0.9	67.9±2.3	2.468E-03 ±1.329E-04	-3.400E-04 ±8.176E-03	8.426±0.038
WA12B (39° 08' 34.90" N 29° 03' 24.70" E)					
z5_s1	22.2±1.1	96.6±0.4	3.445E-03 ±1.784E-04	2.268E-02 ±2.358E-03	8.078±0.022
z3_s1	21.3±1.3	87.7±0.9	3.305E-03 ±2.033E-04	1.606E-02 ±3.864E-03	7.829±0.041
z4_s1	20.2±0.7	66.3±1.6	3.145E-03 ±1.109E-04	2.627E-02 ±6.873E-03	10.20±0.036
z2_s1	19.2±1.1	97.7±1.0	2.976E-03 ±1.674E-04	1.461E-02 ±4.000E-03	8.128±0.051
z1_s1	18.9±1.4	68.4±2.5	2.937E-03 ±2.167E-04	1.922E-02 ±9.092E-03	8.279±0.140
AT05A (39° 25' 43.40" N 29° 07’ 18.20" E)					
z4_s1	24.1±1.3	84.7±0.6	3.752E-03 ±2.022E-04	2.169E-02 ±3.413E-03	7.993±0.020
z2_s1	21.1±0.8	60.6±2.2	3.273E-03 ±1.196E-04	2.214E-02 ±1.028E-02	10.32±0.056
z6_s1	19.5±0.9	97.1±0.5	3.028E-03 ±1.401E-04	1.735E-02 ±1.945E-03	8.342±0.020
z3_s1^{C}	19.0±0.7	95.4±1.2	2.946E-03 ±1.115E-04	1.753E-02 ±5.188E-03	9.188±0.060

Notes: ^{C}= denotes using the ^{204}Pb correction, all others use the ^{206}Pb/^{208}Pb correction assuming common ^{206}Pb/^{204}Pb=18.86, ^{207}Pb/2^{04}Pb=15.62, ^{208}Pb/^{204}Pb=38.34. Ideally the UO+/U+ lies within the range defined by the calibration curve from 7.028±0.014 to 8.634±0.045. Note that WA12Bz5_s1 also gave a ^{207}Pb/^{235}U age of 22.8±2.3 Ma, AT05Az4_s1 gave a ^{207}Pb/^{235}U age of 21.8±3.4 Ma, and AT05Az6_s1 gave a ^{207}Pb/^{235}U age of 17.5±1.9 Ma. The average age of the dated zircons is 20.0±1.1 Ma with a MSWD of 4.7.

Table 7-2: $^{206}Pb/^{238}U$ ion microprobe zircon ages from the Koyunoba pluton.

zircon#_spot#	$^{206}Pb/^{238}U$ Age ±1σ	$^{206}Pb^{*}$% ±1σ	$^{206}Pb^{*}/^{238}U$ ±1σ	$^{207}Pb^{*}/^{235}U$ ±1σ	UO+/U+ ±1σ
AT12 (39° 13' 07.10" N 28° 53' 43.60" E)					
z3_s1	29.9±3.9	6.4±12.6	4.643E-03 ±6.128E-04	3.226E-02 ±7.449E-02	8.815±0.042
z1_s1	25.6±1.5	59.8±2.0	3.983E-03 ±2.344E-04	2.793E-02 ±1.124E-02	7.933±0.029
z5_s2	24.3±1.5	88.7±3.1	3.782E-03 ±2.394E-04	6.246E-03 ±1.425E-02	7.976±0.020
z4_s1	23.8±1.5	59.6±2.4	3.692E-03 ±2.373E-04	3.234E-02 ±1.312E-02	7.814±0.024
z6_s1	20.7±2.3	42.0±7.6	3.213E-03 ±3.600E-04	2.097E-02 ±3.668E-02	8.087±0.034
z5_s1	20.3±1.2	89.1±1.9	3.155E-03 ±1.832E-04	-3.044E-03 ±6.945E-03	7.978±0.051
z2_s1^{C}	19.7±2.7	23.5±12.5	3.060E-03 ±4.202E-04	-9.694E-04 ±4.800E-02	7.969±0.033
AT14 (39° 16’ 59.06” N 28° 54’ 30.70” E)					
z1_s1	26.5±2.5	61.2±2.5	4.120E-03 ±3.905E-04	1.727E-02 ±1.647E-02	7.127±0.042
z3_s1	21.8±1.4	73.7±2.6	3.383E-03 ±2.201E-04	3.292E-02 ±1.208E-02	7.896±0.048
z4_s1	21.3±1.1	95.6±0.4	3.307E-03 ±1.683E-04	2.149E-02 ±2.543E-03	8.100±0.022
z2_s1	14.6±2.6	8.0±17.7	2.264E-03 ±4.083E-04	-2.738E-03 ±6.188E-02	11.34±0.146

Notes: ^{C}= denotes using the ^{204}Pb correction, all others use the $^{206}Pb/^{208}Pb$ correction assuming common $^{206}Pb/^{204}Pb$=18.86, $^{207}Pb/2^{04}Pb$=15.62, $^{208}Pb/^{204}Pb$=38.34. Ideally the UO+/U+ lies within the range defined by the calibration curve from 7.028±0.014 to 8.634±0.045. Note that AT14z4_s1 gave a $^{207}Pb/^{235}U$ age of 21.6±3.5 Ma. The average age of the dated zircons is 22.6±2.2 Ma with a MSWD of 2.8.

Table 7-3: ^{206}Pb/^{238}U ion microprobe zircon ages from the Alacam pluton.

zircon#_spot#	^{206}Pb/^{238}U Age ±1σ	^{206}Pb*% ±1σ	^{206}Pb*/^{238}U ±1σ	^{207}Pb*/^{235}U ±1σ	UO+/U+ ±1σ
AT20A (39° 20' 34.60" N 28° 68' 31.80" E)					
z2_s1^{C}	22.6±1.4	47.9±4.0	3.517E-03 ±2.163E-04	2.717E-02 ±1.710E-02	8.335±0.039
z4_s1^{C}	21.8±1.1	99.0±0.2	3.381E-03 ±1.753E-04	1.971E-02 ±1.346E-03	8.049±0.011
z1_s1^{C}	20.8±1.1	97.4±0.5	3.233E-03 ±1.678E-04	2.300E-02 ±2.466E-03	8.079±0.014
z3_s1^{C}	18.8±0.8	97.6±0.5	2.920E-03 ±1.231E-04	1.632E-02 ±1.870E-03	8.614±0.013
AT20B (39° 20' 34.60" N 28° 68' 31.80" E)					
z5_s1^{C}	17.2±0.9	98.7±0.3	2.674E-03 ±1.364E-04	1.478E-02 ±1.355E-03	8.177±0.035
AT19 (39° 20' 22.30" N 28° 49' 01.20" E)					
z2_s1	25.2±1.5	81.2±0.6	3.916E-03 ±2.363E-04	2.247E-02 ±3.917E-03	7.821±0.052
z1_s1	20.6±2.1	56.3±2.6	3.193E-03 ±3.330E-04	2.199E-02 ±1.246E-02	7.000±0.029
z3_s1^{C}	19.7±1.9	62.0±3.3	3.064E-03 ±2.960E-04	1.777E-02 ±1.177E-02	7.630±0.070

Notes: ^{C}= denotes using the ^{204}Pb correction, all others use the ^{206}Pb/^{208}Pb correction assuming common ^{206}Pb/^{204}Pb=18.86, ^{207}Pb/2^{04}Pb=15.62, ^{208}Pb/^{204}Pb=38.34. Ideally the UO+/U+ lies within the range defined by the calibration curve from 7.028±0.014 to 8.634±0.045. Note that AT20Az1_s1 also gave a ^{207}Pb/^{235}U age of 23.1±2.4 Ma, AT20Az3_s1 gave a ^{207}Pb/^{235}U age of 16.4±1.9, AT20Az4_s1 gave a ^{207}Pb/^{235}U age of 19.8±1.3 Ma, AT20Bz1_s1 gave a ^{207}Pb/^{235}U age of 14.9±1.4 Ma, and AT19z2_s1 gave a ^{207}Pb/^{235}U age of 22.6±3.9 Ma. The average age of the dated zircons is 20.8±1.4 Ma with a MSWD of 4.9.

Table 7-4: Average zircon saturation temperatures of dated samples. Calculations after Watson and Harrison (1983).

Sample	Zr Saturation Temperature (°C)
WA12B	788
AT16	774
AT05A	780
AT12	762
AT14	805
AT19	778
AT20A	786
AT20B	845

Chapter 8: Conclusions

8.1 Outcomes of the Research Questions

Several analytical techniques have been used to understand the crystallization and exhumation of the Egrigoz, Koyunoba, and Alacam plutons in western Turkey including remote sensing, major and trace element geochemical analyses, cathodoluminescence (CL) imaging, and *in situ* ion microprobe zircon dating. Understanding the tectonic history of these three plutons aids in further constraining the complicated geodynamic evolution of the Menderes Massif. Research questions are:

1. *When did the Egrigoz, Koyunoba, and Alacam plutons crystallize and what are their probable source rocks and source regions?* The Egrigoz, Koyunoba, and Alacam plutons crystallized over a period of at least 15 million years between the Oligocene and early Miocene. The plutons are S-type, peraluminous, granite to granodiorites. The granitcs are similar geochemically and likely had a similar source. The heterogeneity in the plutons themselves caused by magma mixing, partial melting, crustal contamination, and post-emplacement fluid interactions makes it difficult to identify a specific source, but we speculate the plutons source from partial melting of the subducting Mediterranean sea floor and overlying lower-middle crust of the Eurasian plate in a post-collisional volcanic arc setting (e.g., Dilek et al., 2009).
2. *How are the Egrigoz, Koyunoba, and Alacam plutons related to one another structurally, geochemically, and tectonically?* Similar major and trace element geochemistry, coeval zircon crystallization ages, and lack of evidence of a detachment fault separating the Alacam pluton from the Egrigoz and Koyunoba pluton support the hypothesis that the plutons are related and share a similar source and tectonic history. CL images show that all plutons experienced fluid-

rock interactions, as evidenced by the variation of CL colors along grain boundaries and microcracks, patchy feldspar zoning, chemical alteration of plagioclase grains, and the presence of calcite precipitated in microcracks and muscovite in deteriorated plagioclase cores.

3. *How and when did the Egrigoz, Koyunoba, and Alacam plutons exhume?* The Egrigoz, Koyunoba, and Alacam plutons began crystallizing as early as 29 Ma and finished by 15 Ma. Pulsed exhumation is evidenced by multiple episodes of brittle deformation shown as cross-cutting microcracks. It is unclear if a single detachment worked to exhume these plutons. Lineations are evidence that the exhumation of the plutons is tectonically controlled. Model A of Corti (Figure 1-1) suggests that there would be clearly identifiable detachments working to exhume these rocks. Our data more closely resembles model B (Figure 1-1B) where granites are working their way to the surface due to large-scale extension.

8.2 Conclusions and Summary of Contributions

Geochemical and geochronological data suggest that the Egrigoz, Koyunoba, and Alacam plutons formed in a post-collisional regime caused by the north-dipping subduction of the African plate under the Eurasian plate along the Hellenic trench. Exhumation of the plutons due to large-scale extension in the Menderes Massif was complete by ~15 Ma. Geochemical analyses show the plutons have similar sources, crystallized over the same time period, and show similar degrees of alteration and interaction with fluids. CL data indicates that the plutons experienced similar deformation histories, noted by the generations of mineral growth, multiple episodes of brittle deformation, and fluid alteration. Data collected from the Egrigoz, Koyunoba and Alacam plutons reported here is consistent with extension initiating in the Menderes

Massif due to subduction roll-back in the late Oligocene and continuing into the Miocene. Complex textures, generations of mineral growth, multiple episodes of deformation, and fluid alteration make it difficult to link ages to a specific tectonic events. The following is an attempt to outline the summary of contributions and future research related to the research questions.

1. *The Northern Menderes Massif plutons are peraluminous S-type granite to granodiorites.* Peraluminous magmas are formed from the melting of mafic rocks (Ellis and Thompson, 1986) or melting pelitic or semi-pelitic rocks (Holtz and Johannes, 1991). S-type granites are thought to form from melted metasedimentary rocks and are strongly peraluminous with high silica contents (Chappell and White, 1974; Frost et al., 2001). These plutons have been reported to be I-type and metaluminous **(**Ozgenc and Ilbeyli, 2008; Dilek et al., 2009; Ilbeyli and Kibici, 2009; Akay, 2009**)** but the difference likely reflects a heterogeneity in the plutons themselves caused by magma mixing, partial melting, crustal contamination, and post-emplacement fluid interactions (Hibbard, 1981; Rollinson, 1993; Andersson and Eklund, 1994; Janousek et al., 2004; Purvis and Robertson, 2005; Pietranik and Waight, 2008; Catlos et al., 2010).
2. *The Northern Menderes Massif plutons were emplaced in a post-collisional volcanic-arc setting and range from magnesian to ferroan with increasing Si contents.* The trace element geochemistry is consistent with the rocks analyzed here being emplaced in a volcanic-arc, forming in the overriding plate of a subduction zone. Magnesian granites are typical of subduction zones whereas ferroan granites are typical of extensional environments (Frost and Lindsley, 1991; Frost et al., 2001) and the presence of both may reflect a change in tectonic settings between compression and extension in the Aegean region.

3. *Geochemical analyses show little difference between the three plutons also consistent with the rocks arising from a similar source.* Major and trace element analyses (Figures 5-10 and 5-11) and in situ ion microprobe zircon ages (Figure 7-13) show little difference between the three plutons suggesting the plutons share a similar source and are not separated by a major structure.
4. *A detachment does not exist between the western edge of the Egrigoz and Koyunoba and eastern edge of the Alacam pluton*. A difference in geochemical analyses would be expected if a detachment separated the plutons. No digital elevation evidence supports the existence of the low angle Simav detachment along the western border of the Egrigoz and Koyunoba plutons. Fieldwork in the Simav area also found no evidence of a detachment fault. CL data indicates that the plutons experienced similar deformation histories and ion microprobe ages indicate that the plutons crystallized during the same time period (Figure 7-13).
5. *Extension lineations are present in the hanging wall of the Simav normal fault.* The hillshade raster shows ~E-W lineations (Figure 4-5) likely due to large-scale ~N-S extension (ten Veen et al., 2009) that are more defined in the hanging wall of the main Simav normal fault. There is no offset of extension lineations between the footwall and hanging wall of the inferred Simav detachment and no grooves paralleling extension were found on the footwall. Extension lineations continue across plutons inferring that extension continued after the exhumation of these rocks.
6. *CL images document a complicated tectonic history including magma mixing, multiple episodes of brittle deformation, and fluid alteration.* Fluid interaction is evidenced in all samples by the variation of CL colors along grain boundaries and microcracks, patchy zoning within feldspars, chemical alteration of plagioclase

grains, and the presence of calcite precipitated in microcracks and muscovite in deteriorated plagioclase cores. Different grain sizes and zoning patterns of plagioclase (Salisbury et al., 2008), corroded relic cores (Janousek et al., 2004), and "flame-type" structures within alkali feldspar (Catlos et al., 2011) are evidence of magma mixing. Multiple episodes of brittle deformation are documented by cross-cutting relationships of microcracks including large intergranular microcracks, intragranular swarms of microcracks, and cleavage microcracks.

7. *The Egrigoz, Koyunoba, and Alacam plutons crystallized over a ~15 m.y. time frame, predominantly centered around 21 Ma.* Ages from the Egrigoz, Koyunoba, and Alacam plutons range from 29.9±3.9 Ma to 14.6±2.6 Ma, with an average of 21.0±1.2 Ma (Figure 7-13). A 15 m.y. time period for the crystallization of these granitics is not unusual; continual generation of magmas in a mantle wedge is possible, even after after the cessation of subduction (Harris et al., 1994). The plutons may have started to crystallize as early as the Oligocene and were exhumed by the Middle Miocene. Zircon ages are consistent with the magmatism largely propagating from the north to the south in the Aegean region (Dilek and Altunkaynak, 2007; Jolivet and Brun, 2010).

8.3 Future Research

The data reported here directly impacts our understanding of the Northern Menderes Massif metamorphic core complex. Suggested areas for future research are:

1. *Explore how the extension lineations seen in the digital topography are evidenced in the field and their relationship to the exhumation of the plutons.* Mylonite zones have been reported to exist in some areas along the boundaries

of the Koyunoba and Egrigoz plutons (e.g. Isik and Tekeli, 2001; Isik et al., 2004; Ring et al., 2005). Mylonites are formed in ductile shear zones (Sibson, 1977) and may indicate the presence of a low angle detachment fault. The relationship of these mylonites to the Alacam pluton is unclear and should be investigated in future work.

2. *Identification and characterization of skarn zones, created by the reaction between host rocks and intruding magma.* These zones contain information that can assist in our understanding different paragenetic, spatial, and temporal characteristics related to the emplacement of the plutons (e.g., Oyman, 2011).
3. *Similar studies could be done on other plutons in the Aegean region.* Several plutons exist in western Turkey, notably the Cataldag, Goynukbelen, Ilica, Kozak, Orhaneli, Salihli, Turgutlu, and Topuk plutons. These methods (i.e. remote sensing, CL imaging, and *in situ* datings) have only been applied to the Salihi and Turgultu plutons in central Turkey. Applying these same techniques to plutons in the Rhodope and Kazdag massifs could lend insight to the timing and nature of extension in the Aegean region.

References

Akay, E., 2009, Geology and petrology of the Simav magmatic complex (NW Anatolia) and its comparison with the Oligo-Miocene granitoids in NW Anatolia; implications on Tertiary tectonic evolution of the region: International Journal of Earth Sciences, v. 98, p. 1655-1675.

Akdeniz, N., and Konak, N., 1979, Menderes Masifinin simav dolayindaki kayabirimleri ve metabazik, metaultramafik kayalarin konomu: Bulletin of the Geological Society of Turkey, v. 22, p. 175-183. [in Turkish]

Aleinikoff, J.N., Reed, J.C., and Wooden, J.L., 1993, Lead isotopic evidence for the origin of Paleo- and Mesoproterozoic rocks of the Colorado Province, U.S.A.: Precambrian Research, v. 63, p. 97-122.

Altunkaynak, S. S., and Yilmaz, Y., 1998, The Mount Kozak magmatic complex, western Anatolia: Journal of Volcanology and Geothermal Research, v. 85, p. 211-231.

Andersson, U. B., and Eklund, O., 1994, Cellular plagioclase intergrowths as a result of crystal-magma mixing in the Proterozoic Aland rapakivi batholith, SW Finland: Contributions to Mineralogy and Petrology, v. 117, p. 124-136.

Bea, F., and Montero, P., 1999, Behavior of accessory phases and redistribution of Zr, REE, Y, Th, and U during metamorphism and partial melting of metapelites in the lower crust; an example from the Kinzigite Formation of Ivrea-Verbano, NW Italy: Geochimica et Cosmochimica Acta, v. 63, p. 1133-1153.

Bingol, E., Delaloye, M., and Ataman, G., 1982, Granitic intrusions in western Anatolia; a contribution to the geodynamic study of this area: Eclogae Geologicae Helvetiae, v. 75, p. 437-446.

Birkle, P., and Satir, M., 1995, Dating, geochemistry and geodynamic significance of the Tertiary magmatism of the Biga Peninsula, NW Turkey: Mineral Research and Exploration Institute of Turkey, p. 171-180.

Bonev, N.G., and Stampfli, G., 2008, Petrology, geochemistry and geodynamic implications of Jurassic island arc magmatism as revealed by mafic volcanic rocks in the Mesozoic low-grade sequence, eastern Rhodope, Bulgaria: Lithos, v. 100, p. 210-233.

Bozkurt, E., and Park, R.G., 1994, Southern Menderes Massif; an incipient metamorphic core complex in western Anatolia, Turkey: Journal of the Geological Society of London, v. 151, p. 213-216.

Bozkurt, E., and Sozbilir, H., 2004, Tectonic evolution of the Gediz Graben; field evidence for an episodic, two-stage extension in western Turkey: Geological Magazine, v. 141, p. 63-79.

Brun, J., and Sokoutis, D., 2010, 45 m.y. of Aegean crust and mantle flow driven by trench retreat: Geology, v. 38, p. 815-818.

Buick, I.S., 1991, The late-Alpine evolution of an extensional shear zone, Naxos, Greece: Journal of the Geological Society, London, v. 148, p. 93-103.

Burkut, Y., 1966, Kuzeybati Anadolu'da Yer Alan Plutonlarin Mukayesli Jenetik Etudu: ITU, Yayin., Istanbul, p. 272. [in Turkish]

Catlos, E.J., and Cemen, I., 2005, Monazite ages and the evolution of the Menderes Massif: International Journal of Earth Sciences, v. 94, p. 204-217.

Catlos, E.J., Baker, C., Cemen, I., and Ozerdem, C., 2008, Whole rock major element influences on monazite growth: examples from igneous and metamorphic rocks in the Menderes Massif, western Turkey: Mineralogia, v. 38, p. 5-18.

Catlos, E. J., Baker, C., Sorensen, S.S., Cemen, I., and Hancer, M., 2010, Geochemistry, geochronology, and cathodoluminescence imagery of the Salihli and Turgutlu granites (central Menderes Massif, western Turkey); implications for Aegean tectonics: Tectonophysics, v. 488, p. 110-130.

Catlos, E.J., Baker, C.B., Sorensen, S.S., Jacob, L.R., Cemen, I, 2011, Linking microcracks and mineral zoning of detachment-exhumed granites to their tectonomagmatic history: Evidence from the Salihi and Turgutlu plutons in western Turkey (Menderes Massif): Journal of Structural Geology, submitted.

Cemen, I., Catlos, E.J., Gogus, O., and Ozerdem, C., 2006, Postcollisional extensional tectonics and exhumation of the Menderes Massif in the western Anatolia extended terrane, Turkey: Special Paper - Geological Society of America, v. 409, p. 353-379.

Chappell, B. W., and White, A.J.R., 1974, Two contrasting granite types: Pacific Geology, v. 8, p. 173-174.

Cherniak, D. J., and Watson, E., 2001, Pb diffusion in zircon: Chemical Geology, v. 172, p. 5-24.

Corti, G., Bonini, M., Conticelli, S., Innocenti, F., Manetti, P., and Sokoutis, D., 2003, Analogue modelling of continental extension; a review focused on the relations between the patterns of deformation and the presence of magma: Earth-Science Reviews, v. 63, p. 169-247.

Cox, K.G., Bell, J.D., and Pankhurst, R.J., 1979, The interpretation of igneous rocks: London, George Allen and Unwin, 445 p.

Cox, R.A., Dempster, T.J., Bell, B.R., and Rogers, G., 1996, Crystallization of the Shap Granite: evidence from zoned K-feldspar megacrysts: Geological Society of London, v. 153, p. 625-635.

De St. Jorre, L., and Smith, D.G.W., 1988, Cathodoluminescence Ga-enriched feldspars from the Thor Lake rare-metal deposits, NW Territories, Canada: Canadian Mineralogy, v. 26, p. 301-308.

Deer, W.A., Howie, R.A., and Zussman, J., 1992, An introduction to the rock-forming minerals: New York, NY, Wiley, 1992, 696 p.

Delaloye, M., and Bingol, E., 2000, Granitoids from western and northwestern Anatolia; geochemistry and modeling of geodynamic evolution: International Geology Review, v. 42, p. 241-268.

Dewey J.F., 1988, Extensional collapse of orogens: Tectonics, v. 7, p. 1123-1139.

Dilek, Y., and Altunkaynak, S., 2007, Cenozoic crustal evolution and mantle dynamics of post-collisional magmatism in western Anatolia: International Geology Review, v. 49, p. 431-453.

Dilek, Y., Altunkaynak, S., and Oner, Z., 2009, Syn-extensional granitoids in the Menderes core complex and the late Cenozoic extensional tectonics of the Aegean province: Geological Society Special Publications, v. 321, p. 197-223.

Dinter, D.A., and Royden, L., 1993, Late Cenozoic extension in northeastern Greece; Strymon Valley detachment system and Rhodope metamorphic core complex: Geology, v. 21, p. 45-48.

Dinter, D.A., 1998, Late Cenozoic extension of the Alpine collisional orogen, northeastern Greece; origin of the North Aegean Basin: Geological Society of America Bulletin, v. 110, p. 1208-1226

Drake, H., Tullborg, E.L., and Annersten, H., 2008, Red-staining of the wall rock and its influence on the reducing capacity around water conducting fractures: Applied Geochemistry, v. 23, p. 1898-1920.

Edwards, M. A., and Grasemann, B., 2009, Mediterranean snapshots of accelerated slab retreat; subduction instability in stalled continental collision: Geological Society Special Publications, v. 311, p. 155-192.

Einaudi, M.T., and Burt, D.M., 1982, Introduction; terminology, classification, and composition of skarn deposits: Economic Geology and the Bulletin of the Society of Economic Geologists, v. 77, p. 745-754.

Ellis, D., and Thompson, A, 1986, Subsolidus and partial melting reactions in the quartz-excess $CaO+MgO+Al_2O_3+SiO_2+H_2O$ system under water-excess and water-deficient conditions to 10 kb; some implications for the origin of peraluminous melts: Journal of Petrology, v. 27, p. 91-121.

Emre, O., 1988, Urgup yoresi peribacalarinin morfojenezi: Geomorphology Bulletin, v. 16, p. 23-30. [in Turkish]

Erkul, F., 2010, Tectonic significance of synextensional ductile shear zones within the early Miocene Alacamdag granites, northwestern Turkey: Geological Magazine, v. 147, p. 611-637.

Ersoy, Y., Helvaci, C., and Sozbilir, H., 2010, Tectonostratigraphic evolution of the NE/SW-trending superimposed Selindi Basin; implications for late Cenozoic crustal extension in western Anatolia, Turkey: Tectonophysics, v. 488, p. 210-232.

Faure, G., 1986, Principles of Isotope Geology: New York, John Wiley & Sons, 589 p.

Finch, A.A., and Klein, J., 1999, The causes and petrological significance of cathodoluminescence emissions from alkali feldspar: Contributions to Mineralogy and Petrology, v. 135, p. 234-243.

Frost, B. R., and Lindsley, D.H., 1991, Occurrence of iron-titanium oxides in igneous rocks: Reviews in Mineralogy, v. 25, p. 433-468.

Frost, B., Barnes, R., Calvin, G., Collins, William J., Arculus, Richard J., Ellis, David J., and Frost, Carol D., 2001, A geochemical classification for granitic rocks: Journal of Petrology, v. 42, p. 2033-2048.

Gautier, P., and Brun, J.P., 1994, Crustal-scale geometry and kinematics of late-orogenic extension in the central Aegean (Cyclades and Evvia Island): Tectonophysics, v. 238, p. 399-424.

Gautier, P., Bozkurt, E., Bosse, V., Hallot, E., and Dirik, K., 2008, Coeval extensional shearing and lateral underflow during Late Cretaceous core complex development in the Nigde Massif, central Anatolia, Turkey: Tectonics, v. 27, doi: 10.1029/2006TC002089.

Geake, J.E., Walker, G., Telfer, D.J., Mills, A.A., and Garlick, G.F.J., 1973, Luminescence of lunar, terrestrial, and synthesized plagioclase, caused by Mn^{2+} and Fe^{3+}: Geochimica et Cosmochimica Acta, v. 3, p. 181-189.

Genc, S., 1998, Evolution of the Bayramic magmatic complex, northwestern Anatolia: Journal of Volcanology and Geothermal Research, v. 85, p. 233-249.

Gessner, K., Piazolo, S., Gungor, T., Ring, U., Kroener, A., and Passchier, C., 2001, Tectonic significance of deformation patterns in granitoid rocks of the Menderes nappes, Anatolide Belt, Southwest Turkey: International Journal of Earth Sciences, v. 89, p. 766-780.

Gessner, K., Ring, U., Passchier, C.W., Johnson, C., Hetzel, R., and Gungor, T., 2001, An active bivergent rolling-hinge detachment system: Central Menderes metamorphic core complex in western Turkey: Geology, v. 29, p. 611-614.

Glodny, J., and Hetzel, G., 2007, Precise U-Pb ages of syn-extensional Miocene intrusions in the central Menderes Massif, western Turkey: Geological Magazine, v. 144, p. 235-246.

Goetze, J., Krbetschek, M.R., Habermann, D., and Wolf, D., 2000, High-resolution cathodoluminescence studies of feldspar minerals: Cathodoluminescence in geosciences, v. 26, p. 245-270.

Gorur, N., Oktay, F.Y., Seymen, I., and Sengor, A.M.C., 1984, Paleotectonic evolution of Tuzgolu basin complex, Central Turkey. The geologic evolution of the Eastern Mediterranean: Geological Society Special Publications, v. 17, p. 81-96.

Green, T.H., and Pearson, N.J., 1986, Ti-rich accessory phase saturation in hydrous mafic-felsic compositions at high P,T: Chemical Geology, v. 54, p. 185-201.

Gurer, O., Bozcu, M., and Yilmaz, Y., 1999, Geology and development of the Gediz-Alasehir Graben region; western Anatolia: European Union of Geosciences conference abstracts, v. 4, p. 35.

Harris, C.C. and Vogeli, J., 2010, Oxygen isotope composition of garnet in the Peninsula Granite, Cape granite suite, South Africa; constraints on melting and emplacement mechanisms: South African Journal of Geology, v. 113, p. 401-412.

Harris, N.W., Kelley, S., and Okay, A., 1994, Post-collision magmatism and tectonics in Northwest Anatolia: Contributions to Mineralogy and Petrology, v. 117, p. 241-252.

Harrison, T., and Watson, B.E., 1984, The behavior of apatite during crustal anatexis; equilibrium and kinetic considerations: Geochimica et Cosmochimica Acta, v. 48, p. 1467-1477.

Harrison, T., McKeegan, K.D., and LeFort, P., 1995, Detection of inherited monazite in the Manaslu leucogranite by $^{208}Pb/^{232}Th$ ion microprobe dating; crystallization age and tectonic implications: Earth and Planetary Science Letters, v. 133, p. 271-282.

Hasozbek, A., Satir, M., Erdogan, B., Akay, E., and Siebel, W., 2010, Early Miocene post-collisional magmatism in NW Turkey: geochemical and geochronological constraints: International Geology Review, doi: 10.1080/00206810903579302.

Hetzel, R.R., and Dora, O., 1994, Miocene extensional tectonics in the Menderes Massif, southwestern Turkey: Bulletin of the Geological Society of Greece, v. 30, p. 507-512.

Hetzel, R.R., Ring, U., Akal, C., and Troesch, M., 1995, Miocene NNE-directed extensional unroofing in the Menderes Massif, southwestern Turkey: Journal of the Geological Society of London, v. 152, p. 639-654.

Hetzel R.R., Romer, R.L., Candan, O., Passchier, C.W., 1998, Geology of the Bozdag area, central Menderes Massif, SW Turkey; Pan-African basement and Alpine deformation: Geologische Rundschau, v. 87, p. 639-654.

Hibbard, M. J., 1981, The magma mixing origin of mantled feldspars: Contributions to Mineralogy and Petrology, v. 76, p. 158-170.

Holtz, F., and Johannes, W., 1991, Genesis of peraluminous granites; I, Experimental investigation of melt compositions at 3 and 5 kb and various H (sub 2) O activities: Journal of Petrology, v. 32, p. 935-958.

Ilbeyli, N., and Kibici, Y., 2009, Collision-related granite magma genesis, potential sources and tectono-magmatic evolution; comparison between central, northwestern and western Anatolia (Turkey): International Geology Review, v. 51, p. 252-278.

Isik, V., and Tekeli, O., 2001, Late orogenic crustal extension in the northern Menderes massif (western Turkey): evidence for metamorphic core complex formation: International Journal of Earth Sciences, v. 89, p. 757-765.

Isik, V., Seyitoglu, G., and Cemen, I., 2003, Ductile-brittle transition along the Alasehir detachment fault and its structural relationship with the Simav detachment fault, Menderes massif, western Turkey: Tectonophysics, v. 374, p. 1-18.

Isik, V., Tekeli, O., and Seyitoglu, G., 2004, The (super 40) Ar/ (super 39) Ar age of extensional ductile deformation and granitoid intrusion in the northern Menderes core complex; implications for the initiation of extensional tectonics in western Turkey: Journal of Asian Earth Sciences, v. 23, p. 555-566.

Janousek, V., Bowes, D.R., Braithwaite, C.J.R., and Roger, G., 2001, Microstructural and mineralogical evidence for limited involvement of a Hercynian high-K calc-alkaline instrusion: the Kozarovice granodiorite, Central Bohemian Pluton, Czech Republic: Earth Science, v. 91, p. 15-26.

Janousek, V., Braithwaite, C., Bowes, D., and Gerdes, A., 2004, Magma-mixing in the genesis of Hercynian calc-alkaline granitoids; an integrated petrographic and geochemical study of the Sazava Intrusion, Central Bohemian Pluton, Czech Republic: Lithos, v. 78, p. 67-99.

Jolivet, L.L., Daniel, J.M., Truffert, C., and Goffe, B., 1994, Exhumation of deep crustal metamorphic rocks and crustal extension in arc and back-arc regions: Lithos, v. 33, p. 3-30.

Jolivet, L., and Brun, J.P., 2010, Cenozoic geodynamic evolution of the Aegean: International Journal of Earth Sciences, v. 99, p. 109-138.

Karacik, Z. Z., and Yilmaz, Y., 1998, Geology of the ignimbrites and the associated volcano-plutonic complex of the Ezine area, northwestern Anatolia: Journal of Volcanology and Geothermal Research, v. 85, p. 251-264.

Kilias, A.A., Fassoulas, C., and Mountrakis, D., 1994, Tertiary extension of continental crust and uplift of Psiloritis metamorphic core complex in the central part of the Hellenic Arc (Crete, Greece): Geologische Rundschau, v. 83, p. 417-430.

Kocyigit, A., Yusufoglu, H., and Bozkurt, E., 1999, Evidence from the Gediz Graben for episodic two-stage extension in western Turkey: Journal of the Geological Society of London, v. 156, p. 605-616.

Konak, N., 2002, Geological map of Turkey: Izmir Turkiye Jeoloji Haritasi, scale 1:500,000.

Kopp, O. C., 1981, Cathodoluminescence petrography; a valuable tool for teaching and research: Journal of Geological Education, v. 29, p. 108-113.

Kretz, R., 1983, Symbols for rock-forming minerals: American Mineralogist, v. 68, p. 277-279.

Kretz, R., Hartree, R., and Jones, P., 1989, Metasomatic crystallization of muscovite in granite and tourmaline in schist related to pegmatite emplacement near Yellowknife, Canada: Contributions to Mineralogy and Petrology, v. 102, p. 191-204

Le Maitre, R.W., Bateman, P., Dudek, A., Keller, J., Lameyre Le Bas, M.J., Sabine, P.A., Schmid, R., Sorensen, H., Streckeisen, A., Woolley, A.R., and Zanettin, B., 1989, A classification of igneous rocks and glossary of terms: Oxford, Blackwell science publisher, 193 p.

Le Pichon, X., and Angelier, J., 1979, The Hellenic arc and trench system; a key to the neotectonic evolution of the eastern Mediterranean area: Tectonophysics, v. 60, p. 1-42.

Le Pichon, X., and Angelier, J., 1981, The Aegean Sea: Philosophical Transactions of the Royal Society of London, Series A: Mathematical and Physical Sciences, v. 300, p. 357-372.

Leichmann, J., Broska, I., and Zachovalova, K., 2003, Low-grade metamorphic alteration of feldspar minerals: a CL study: Terra Nova, v. 15, p. 104-108.

Lindsley, D. H., 1991, Experimental studies of oxide minerals: Reviews in Mineralogy, v. 25, p. 69-106.

Lips, A., Cassard, D., and Sozbilir, H., 2001, Multistage exhumation of the Menderes Massif, western Anatolia (Turkey): International Journal of Earth Sciences, v. 89, p. 781-792.

Lister, G., Banga, G., and Feenstra, A., 1984, Metamorphic core complexes of cordilleran type in the Cyclades, Aegean sea, Greece: Geology, v. 12, p. 221-225.

MacKenzie, W.S., and Guilford, C., 1980, Atlas of rock-forming minerals in thin section: London, Longman Group, 97 p.

Maniar, P.D., and Piccoli, P.M., 1989, Tectonic discrimination of granitoids: Geological Society of America Bulletin, v. 101, p. 635-643.

Mariano, A.N., and Ring, P.J., 1975, Europium-activated cathodoluminescence in minerals: Geochimica et Cosmochimica Acta, v. 39, p. 649-660.

Marshak, S., 2001, Earth; portrait of a planet: United States, W.W. Norton & Company, 735 p.

Marshall, D.J., 1977, Suggested standards for the reporting of cathodoluminescence results: Journal of Sedimentary Research, v. 48, p. 651-653.

Marshall, D.J., 1988, Cathodoluminescence of geological materials: Boston, Unwin Hyman, 146 p.

Meulenkamp, J.E., Wortel, M., van Wamel, W.A., Spakman, W., and Hoogerduyn Strating, E., 1988, On the Hellenic subduction zone and the geodynamic evolution of Crete since the late middle Miocene: Tectonophysics, v. 146, p. 203-215.

Middlemost, E.A.K., 1994, Naming materials in the magma/igneous rock system: Earth-Science Reviews, v. 37, p. 91-104.

Miller, C.F., 1985, Are strongly peraluminous magmas derived from pelitic sedimentary sources?: Journal of Geology, v. 93, p. 673-689.

Miller, C.F., Meschter McDowell, S., and Mapes, R.W., 2003, Hot and cold granites? Implications of zircon saturation temperatures and preservation of inheritance: Geology, v. 31, p. 529-532.

Morad, S.S., El-Ghali, M.A..K., Caja, M.A., Sirat, M., Al-Ramadan, K., and Mansurbeg, H., 2010, Hydrothermal alteration of plagioclase in granitic rocks from Proterozoic basement of SE Sweden: Geological Journal, v. 45, p. 105-116.

Mouri, H.H., Brandl, G., Whitehouse, M., de Waal, S., and Guiraud, M., 2008, CL-imaging and ion microprobe dating of single zircons from a high-grade rock from the Central Zone, Limpopo Belt, South Africa; evidence for a single metamorphic event at nearly equal 2.0 Ga. Journal of African Earth Sciences, v. 50, p. 111-119.

Mukasa, S.B., and Henry, D.J., 1990, The San Nicolas Batholith of coastal Peru; early Palaeozoic continental arc or continental rift magmatism?: Journal of the Geological Society of London, v. 147, p. 27-39.

Oberhaensli, R., Partzsch, J., Candan, O., and Cetinkaplam, M., 2001, First occurrence of Fe-Mg-carpholite documenting a high-pressure metamorphism in metasediments of the Lycian nappes, SW Turkey: International Journal of Earth Sciences v. 89, p. 867-873.

Okay, I.A., and Satir, M., 2000, Coeval plutonism and metamorphism in a latest Oligocene metamorphic core complex in northwest Turkey: Geological Magazine, v. 137, p. 495-516.

Okay, A.I., Satir, M., Zattin, M., Cavazza, W., and Topuz, G., 2008, An Oligocene ductile strike-slip shear zone; the Uludag Massif, northwest Turkey; implications for the westward translation of Anatolia: Geological Society of America Bulletin, v. 120, p. 893-911.

Oyman, T., Ozgenc, I., Tokcaer, M., and Akbulut, M., 2011, Petrology, geochemistry and evolution of the iron skarns along the northern contact of the Egrigoz plutonic complex, western Anatolia, Turkey: In Press.

Oztunali, O., 1973, Petrology and geochronology of Uludag (NW Anatolia) and Egrigoz (W Anatolia) massifs: Istanbul Universitesi Fen Fakultesi Monografileri, v. 23, p. 1-115. [in Turkish]

Ozgenc, I., and Ilbeyli, N., 2008, Petrogenesis of the late Cenozoic Egrigoz Pluton in western Anatolia, Turkey; implications for magma genesis and crustal processes: International Geology Review, v. 50, p. 375-391.

Papanikolaou, D.J., and Demirtasli, E., 1987, Geological correlation between the Alpine segments of the Hellenides-Balkanies and Taurides-Pontides. In: Pre-Variscan and Variscan events in the Alpine-Mediterranean Mountain Belts, Flugel, H.W., et al., Bratislava, Alfa Publishers, p. 387-396.

Parsons, I., Steele, D.A., Lee, M.R., and Magee, C.W., 2008, Titanium as cathodoluminescence activator in alkali K-feldspar: American Mineralogist, v. 93, p. 875-879.

Paton, S., 1992, Active normal faulting, drainage patterns and sedimentation in southwestern Turkey: Journal of the Geological Society of London, v. 149, p. 1031-1044.

Pearce, J.A, and Cann, J.R., 1971, Ophiolite origin investigated by discriminant analysis using Ti, Zr, and Y: Earth Planet Science Letter, v. 12, p. 339-349.

Pearce, T.H., 1984, Optical dispersion and zoning in magmatic plagioclase; laser-interference observations: Canadian Mineralogist, v. 22, p. 383-390.

Pidgeon, R.T., 1992, Recrystallisation of oscillatory zoned zircon; some geochronological and petrological implications: Contributions to Mineralogy and Petrology, v. 110, p. 463-472.

Pietranik, A., and Waight, T., 2008, Processes and sources during late Variscan dioritic-tonalitic magmatism; insights from plagioclase chemistry (Gesiniec Intrusion, NE Bohemian Massif, Poland): Journal of Petrology, v. 49, p. 1619-1645.

Pinet, B., and Colletta, B., 1990, Probing into extensional sedimentary basins: Comparison of recent data and derivation of tentative models: Tectonophysics, v. 173, p. 185-197.

Purvis, M., and Robertson, A., 2005, Sedimentation of the Neogene-Recent Alasehir (Gediz) continental graben system used to test alternative tectonic models for western (Aegean) Turkey: Sedimentary Geology, v. 173, p. 373-408.

Ramseyer, K.K., Al Dahan, A.A., Collini, B., and Landstrom, O., 1992, Petrological modifications in granitic rocks from the Siljan impact structure; evidence from Cathodoluminescence: Tectonophysics, v. 216, p. 195-204.

Reischmann, T.T., Kroener, A., Todt, W., Duerr, S., and Sengor, A.M.C., 1991, Episodes of crustal growth in the Menderes Massif, W Turkey, inferred from zircon dating: European Union of Geosciences Terra Abstracts, v. 3, p. 34.

Rimmele, G., Oberhaensli, R., Goffe, B., Jolivet, L., Candan, O., and Cetinkaplam, M., 2003, First evidence of high-pressure metamorphism in the 'Cover Series' of the southern Menderes Massif; tectonic and metamorphic implications for the evolution of SW Turkey: Lithos, v. 71, p. 19-46.

Ring, U., Brandon, M., Willet, S., and Lister, G., 1999, Exhumation processes: Geological Society Special Publications, v. 154, p. 1-27.

Ring, U., Willner, A., and Lackmann, W., 2001, Stacking of nappes with different pressure-temperature paths; an example from the Menderes Nappes of western Turkey: American Journal of Science, v. 301, p. 912-944.

Ring, U., and Collins, A.S., 2005, U-Pb SIMS dating of synkinematic granites; timing of core-complex formation in the northern Anatolide Belt of western Turkey: Journal of the Geological Society of London, v. 162, p. 289-298.

Rollinson, H. R., 1993, Using Geochemical Data; Evaluation, Presentation, Interpretation: United Kingdom, Longman Scientific and Technical, 352 p.

Salisbury, M. J., Bohrson, W.A., Clynne, M.A., Ramos, F.C., Hoskin, P., 2008, Multiple plagioclase crystal populations identified by crystal size distribution and in situ chemical data; implications for timescales of magma chamber processes associated with the 1915 eruption of Lassen Peak, CA.: Journal of Petrology, v. 49, p. 1755-1780.

Schneider, D.A., Edwards, M.A., Kidd, W.S.F., Zeitler, P.K., and Coath, C.D., 1999, Early Miocene anatexis identified in the western syntaxis, Pakistan Himalaya: Earth and Planetary Science Letters, v. 167, p. 121-129.

Schuiling, R.D., 1962, On petrology, age and structure of the Menderes migmatite complex (SW-Turkey): Bulletin of the Mineral Research and Exploration Institute of Turkey, v. 58, p. 71-84.

Sengor, A., and Yilmaz, Y., 1981, Tethyan evolution of Turkey; a plate tectonic approach: Tectonophysics, v. 75, p. 181-241.

Seyitoglu, G., and Scott, B., 1992, Late Cenozoic volcanic evolution of the northeastern Aegean region: Journal of Volcanology and Geothermal Research, v. 54, p.157-176.

Seyitoglu, G., and Scott, B., 1996, The cause of N-S extensional tectonics in western Turkey; tectonic escape vs back-arc spreading vs orogenic collapse: Journal of Geodynamics, v. 22, p. 145-153.

Seyitoglu, G., 1997, The Simav Graben: An Example of Young E-W Trending Structures in the Late Cenozoic Extensional System of Western Turkey: Turkish Journal of earth sciences, v. 6, p. 135-141.

Seyitoglu, G., Tekeli, O; Cemen, I., Sen, S., and Isik, V., 2002, The role of the flexural rotation/rolling hinge model in the tectonic evolution of the Alasehir Graben, western Turkey: Geological Magazine, v. 139, p. 15-26.

Seyitoglu, G., Isik, V., and Cemen, I., 2004, Complete Tertiary exhumation history of the Menderes Massif, western Turkey; an alternative working hypothesis: Terra Nova, v. 16, p. 358-364.

Seyitoglu, G., and Isik, V., 2009, Meaning of the Kucuk Menderes graben in the tectonic framework of the central Menderes metamorphic core complex: Geologica Acta, v. 7, p. 323-331.

Sibson, R.H., 1977, Fault rocks and fault mechanisms: Journal of the Geological Society of London, v. 133, p. 191-213.

Sorensen, S., Harlow, George E., and Rumble III, D., 2006, The origin of jadeitite-forming subduction-zone fluids; CL-guided SIMS oxygen-isotope and trace-element evidence: American Mineralogist, v. 91, p. 979-996.

Sozbilir, H., 2001, Extension tectonics and the geometry of related macroscopic structures; field evidence from the Gediz detachment, western Turkey: Turkish Journal of Earth Sciences, v. 10, p. 51-67.

Stirling, D., Duncan, A.M., Guest, J.E., and Finch, A.A., 1999, Petrogenesis of plagioclase phenocryst of Mount Etna, Sicily, with particular reference to the 19833 eruption: contribution from cathodoluminescence petrography: Miner Magazine, v. 63, p. 189-199.

Sun, S.S., and McDonough, W.F., 1989, Chemical and isotopic systemics of oceanic basalts: implications for mantle composition and processes. Magmatism in ocean basins: Geological Society Special Publications, v. 42, p. 313-345.

Tankut, A., Dilek, Y., and Onen, P., 1988, Petrology and geochemistry of the neo-Tethyan volcanism as revealed in the Ankara mélange, Turkey: Journal of Volcanological and Geothermal Research, v. 85, p. 265-284.

Tekeli, O., Isik, V., Seyitoglu, G., and Cemen, I., 2001, The $^{40}Ar/^{39}Ar$ age of ductile extension and granitoid intrusions in the northern Menderes massif, western Turkey: 4th International Turkish Geology Sym. Abstract 226.

ten Veen, J.H., Boulton, S.J., Alcicek, M.C., 2009, From palaeotectonics to neotectonics in the Neotethys realm; the importance of kinematic decoupling and inherited structural grain in SW Anatolia (Turkey): Tectonophysics, v. 473, p. 261-281.

Thomson, S.N., and Ring, U., 2006, Thermochronologic evaluation of postcollision extension in the Anatolide Orogen, western Turkey: Tectonics, v. 25, doi:10.1029/2005TC001833.

Vandenberg, L.S., and Lister, G.S., 1996, Structural analysis of basement tectonites from the Aegean metamorphic core complex of Ios Cyclades, Greece: Journal of Structural Geology, v. 18, p. 1437-154.

Vavra, G., 1990, On the kinematics of zircon growth and its petrogenetic significance; a cathodoluminescence study: Contributions to Mineralogy and Petrology, v. 106, p. 90-99.

Watson, E., and Harrison, M.T., 1983, Zircon saturation revisited; temperature and composition effects in a variety of crustal magma types: Earth and Planetary Science Letters, v. 64, p. 295-304.

Wendt, I.I., and Carl, C., 1991, The statistical distribution of the mean squared weighted deviation: Chemical Geology; Isotope Geoscience Section, v.86, p. 275-285.

Westaway, R., 2006, Cenozoic cooling histories in the Menderes Massif, western Turkey, may be caused by erosion and flat subduction, not low-angle normal faulting: Tectonophysics, v. 412, p. 1-25.

Whitehouse, M. J., Claesson, S., Sunde, T., and Vestin, J., 1997, Ion microprobe U-Pb zircon geochronology and correlation of Archaean gneisses from the Lewisian Complex of Gruinard Bay, northwestern Scotland: Geochimica et Cosmochimica Acta, v. 61, p. 4429-4438.

Wilson, M., 1989, Igneous Petrogenesis; a global tectonic approach: London, Unwin Hyman, 466 p.

Yilmaz, Y., Genc, S.C., Gurer, F., Bozcu, M., Yilmaz, K., Karacik, Z., Altunkaynak, S., and Elmas, A., 2000, When did the western Anatolian grabens begin to develop?: Geological Society Special Publications, v. 173, p. 353-384.

Vita

Lauren Jacob was born in Mandeville, LA in 1984. She grew up in Mandeville with four siblings. Lauren first realized her interest in geology after a family vacation to the mountains in 1990.

Lauren graduated from Mandeville High School in 2003. She and her twin brother were co-valedictorians. After graduation, she enrolled at LSU as an elementary education major. In 2007, she received her B.S. in education and was hired to teach third grade at Woodlake Elementary School. After a few weeks in the classroom, she realized that teaching did not offer the academic challenges she had hoped and quickly decided to pursue a M.S. in geology.

After finishing the school year at Woodlake, Lauren re-enrolled at LSU to take pre-requisites for a geology masters program. During this year, she applied and was accepted to UT Austin for the fall of 2009.

Lauren moved to Austin, TX to begin work on her masters degree in August, 2009. Under her advisor, Elizabeth Catlos, she studied the tectonic environment of the Egrigoz, Koyunoba, and Alacam plutons in western Turkey. Her research focused on petrology and geochemistry as they relate to large-scale tectonic deformation. Upon graduation in May 2011, she will be employed with Apache Corporation, an oil and gas company located in Houston, TX.

Permanent email: laurenrjacob@gmail.com

This thesis was typed by Lauren Jacob.